AD-A250 089

Optimized Photorefractive Barium Titanate

Final Report, Contract No. F19628-87-C-0173

March 11, 1992

Cardinal Warde and Hans Jenssen, Principal Investigators

Department of Electrical Engineering and Computer Science
Massachusetts Institute of Technology
Cambridge, Massachusetts, 02139, USA

Hanscom Air Force Base
Bedford, MA 01731

DTIC
ELECTE
MAY 07 1992
S B D

Approved for public release
Distributed unlimited

92-12233

92 5 06 001

SECURITY CLASSIFICATION OF THIS PAGE

REPORT DOCUMENTATION PAGE

Form Approved OMB No. 0704-0188

1a. REPORT SECURITY CLASSIFICATION Unclassified	1b. RESTRICTIVE MARKINGS None
2a. SECURITY CLASSIFICATION AUTHORITY N/A	3. DISTRIBUTION / AVAILABILITY OF REPORT Unlimited
2b. DECLASSIFICATION / DOWNGRADING SCHEDULE	
4. PERFORMING ORGANIZATION REPORT NUMBER(S)	5. MONITORING ORGANIZATION REPORT NUMBER(S)
6a. NAME OF PERFORMING ORGANIZATION Massachusetts Institute of Technology 6b. OFFICE SYMBOL (If applicable)	7a. NAME OF MONITORING ORGANIZATION Hanscom Air Force Base
6c. ADDRESS (City, State, and ZIP Code) 77 Massachusetts Avenue Cambridge, MA 02139	7b. ADDRESS (City, State, and ZIP Code) Hanscom Air Force Base Massachusetts 01731-5320
8a. NAME OF FUNDING / SPONSORING ORGANIZATION ESD/Air Force System Command 8b. OFFICE SYMBOL (If applicable) USAF	9. PROCUREMENT INSTRUMENT IDENTIFICATION NUMBER F 19628-87-C-0173
8c. ADDRESS (City, State, and ZIP Code) Hanscom AFB Massachusetts 01731-5320	10. SOURCE OF FUNDING NUMBERS PROGRAM ELEMENT NO. / PROJECT NO. / TASK NO. / WORK UNIT ACCESSION NO.

11. TITLE (Include Security Classification)
OPTIMIZED PHOTOREFRACTIVE BARIUM TITANATE

12. PERSONAL AUTHOR(S)
Cardinal Warde and Hans P. Jenssen

13a. TYPE OF REPORT	13b. TIME COVERED	14. DATE OF REPORT (Year, Month, Day)	15. PAGE COUNT
Final	FROM 2/20/87 TO 5/31/90	2/11/92	

16. SUPPLEMENTARY NOTATION

17. COSATI CODES			18. SUBJECT TERMS (Continue on reverse if necessary and identify by block number)
FIELD	GROUP	SUB-GROUP	Photorefractive Barium Titanate, crystal growth, optical properties

19. ABSTRACT (Continue on reverse if necessary and identify by block number)

20. DISTRIBUTION / AVAILABILITY OF ABSTRACT ☒ UNCLASSIFIED/UNLIMITED ☐ SAME AS RPT. ☐ DTIC USERS	21. ABSTRACT SECURITY CLASSIFICATION
22a. NAME OF RESPONSIBLE INDIVIDUAL Cardinal Warde	22b. TELEPHONE (Include Area Code) 617-253-6858 22c. OFFICE SYMBOL

DD Form 1473, JUN 86 Previous editions are obsolete. SECURITY CLASSIFICATION OF THIS PAGE

Abstract

The goal of this research program was to investigate new and modified crystal-growth techniques that would lead to high-optical-quality $BaTiO_3$ with increased photorefractive speed and sensitivity. The research program consisted of (1) feed material purification, (2) crystal growth by the top-seeded-solution technique as well as by a barium borate flux technique, (3) new furnace design studies and (4) photorefractive characterization experiments. Iron and nickel-doped $BaTiO_3$ crystals were grown under the program.

$BaTiO_3$ is a promising photorefractive material due to its large electrooptic coefficient and excellent self-pumped phase conjugation. Our furnaces were limited by certain design and operating characteristics, and crystals grown in these furnaces were easily contaminated by the furnace itself. Two new furnaces, cylindrical and octagonal furnaces, were developed with commercially available parts that are cleaner, more mechanically reproducible , more uniform in temperature and more responsive to control action through reduced thermal mass. The two furnaces are equipped with precise computer control of the pulling and rotation system. The cylindrical furnace was found to be susceptible to cracking due to expansion when heated and to shrinkage after heating. To prevent cracking, expansion joints were provided and the insulation set was made of flat plates set up in an octagonal pattern.

In order to widen the scope of $BaTiO_3$ growth, we investigated the BaO-B_2O_3-TiO_2 system, which, compared to the conventional BaO-TiO_2 system, would allow crystallization under different chemical condition at a lower temperature and over a wider range of Ba to Ti ratio. Due to the high melt viscosity, the crystals grown from the borate fluxed melts exhibited block structure and overgrown layers. Though large crystals were grown, after extensive cutting and polishing only *mm size inclusion and crack free pieces could be found.*

In addition to changing the absorption coefficient of $BaTiO_3$, adding iron caused a light-induced absorption effect. The excitation of holes results in a light-induced increase in the absorption coefficient of the doped samples which is believed to be due to an increase in the Fe^{+4} concentration.

Electric field driven color-fronts were observed when the iron-doped samples were electrically poled in an oil bath. These color-fronts were shown to be due to the motion of oxygen vacancies in the applied electrical field. The study of the motion of these color-front yielded a value of the oxygen vacancy mobility at low temperature.

Nickel was also added into $BaTiO_3$ as dopant to optimize the photorefractive properties, in particular, beam coupling gain and response time. The Ni-doped $BaTiO_3$ crystals were more difficult to grow than the iron-doped material. The Ni-doped crystals have more cracks and defects, and hence were difficult to pole. In the doping level range, 0-50 ppm, no significant change of photorefractive properties were observed.

A subcontract was instituted at the Sanders Associates for feed purification, and the growth of large size $BaTiO_3$, and Ni-doped $BaTiO_3$. Two large undoped crystals were delivered to RADC under the program.

Accession For
NTIS GRA&I ☑
DTIC TAB ☐
Unannounced ☐
Justification
By
Distribution/
Availability Codes
Dist | Avail and/or Special
A-1

QUALITY INSPECTED 4

Contents

1 Introduction 5
- 1.1 The Photorefractive Effect 5
- 1.2 References 9

2 $BaTiO_3$: Physical Properties and Crystal Growth 12
- 2.1 Physical Propertity 12
- 2.2 Crystal Growth and Preparation 14
- 2.3 References 20

3 Improved Furnace Design and Assembly, and BaO-B_2O_3-TiO_2 Growth System 21
- 3.1 BaO-TiO_2 System 22
- 3.2 Crystal Growth Run 22
- 3.3 Top-Seeded Solution Growth of $BaTiO_3$-Review 24
- 3.4 BaO-B_2O_3-TiO_2 System 24
- 3.5 References 39

4 Characterization of $BaTiO_3$: Ni 49
- 4.1 Introduction 50
- 4.2 Absorption Spectroscopy 50
- 4.3 Two-Beam Coupling Measurement 51
- 4.4 Light-Induced Grating Erasure Measurement 54
- 4.5 Conclusions 58

5 Intensity-Dependent Absorption in $BaTiO_3$:Fe 60
- 5.1 Intensity-Dependent Absorption 61
- 5.2 Experimental Procedures 61
- 5.3 Results 66
- 5.4 Summary of Absorption Data 74
- 5.5 References 75

6 Color Front Dynamics in $BaTiO_3$ 76
- 6.1 Review of Literature 77
- 6.2 Difference Between $SrTiO_3$ and $BaTiO_3$ Color-Front Motion 78
- 6.3 Experimental Procedures and Results 78
- 6.4 Modeling 84
- 6.5 Summary 89
- 6.6 References 89

7 Appendix (Publications) 91
- 7.1 Photoinduced Optical Absorption in $BaTiO_3$:Fe 92
- 7.2 Intensity Dependent Photorefractive Properties of $BaTiO_3$ 95

8 Publication and Presentations 99

9 List of Personnel 100

1 Introduction

1.1 The Photorefractive Effect

The wide spread proliferation of laser technology and the growing interest in nonlinear optics during the early sixties, led to an intensive search for new optical materials. This early research was primarily concerned with parametric wave-mixing, such as frequency doubling,[1,2] and parametric amplification.[3,4] Since these processes required a variety of phase matching conditions, many birefringent crystals, such as ammonium dihydrogen phosphate (ADP),[5] potassium dihydrogen phosphate (KDP), [6] and barium sodium niobate $Ba_2NaNb_5O_{15}$,[7] were examined. Unfortunately, the high optical intensities required for optical parametric processes were also a source of optical damage.[8]

In $LiNbO_3$ and $LiTaO_3$, this damage was manifest as distortions in the refractive index along the path of the beam,[8] which could be reversed by heating the crystal, or by flooding it uniformly with light. This damage was also found to be a function of total energy incident on the crystal. That is, short exposure times and high intensities gave the same effect as long exposure times and low intensities. The ability of the crystal to integrate the optical power indicated that some type of microscopic transport process could be involved. Since the refractive index damage was photo-induced, the term photorefractive was coined.

In a similar phenomenon, known as the photochromic effect, the optical absorption could be changed by the application of light. This change in the absorption was shown to be the result of photo-induced charge transfer between impurity ions in the crystal.[9,10] Since different valence states of the ions had different absorption spectra, spatially varying intensity patterns generated spatially varying absorption centers in the crystal. An extension of this model was used by Chen[11] to explain the optical damage seen in $LiNbO_3$.

In Chen's model, Fig. 1, charge trapped in defects or impurities in the band gap, is photoexcited in the high intensity regions of the crystal. The liberated carriers then migrate to the dark regions of the crystal, resulting in a redistribution of charge with the same spatial variation as the incident light. This redistributed charge has an associated space charge field which, in noncentrosymmetric crystals, induces a change in the refractive index through the linear electrooptic effect. Since the symmetry requirement for phase matching is the same as that for the electrooptic effect, no inversion symmetry, many materials of possible use in parametric wave mixing were found to be subject to photorefractive damage. Some of the materials found to be photorefractive include ferroelectric $BaTiO_3$,[12] $Sr_xBa_{1-x}Nb_2O_6$ (SBN),[13] $Ba_2NaNb_5O_{15}$,[14] and $KNbO_3$,[15] non-ferroelectric $Bi_{12}SiO_{20}$ (BSO),[16] and GaAs,[17] and organic polymers.[18] Also certain PLZT ceramics,[19,20] which possess only a second order (Kerr) electrooptic effect, have been found to be photorefractive.

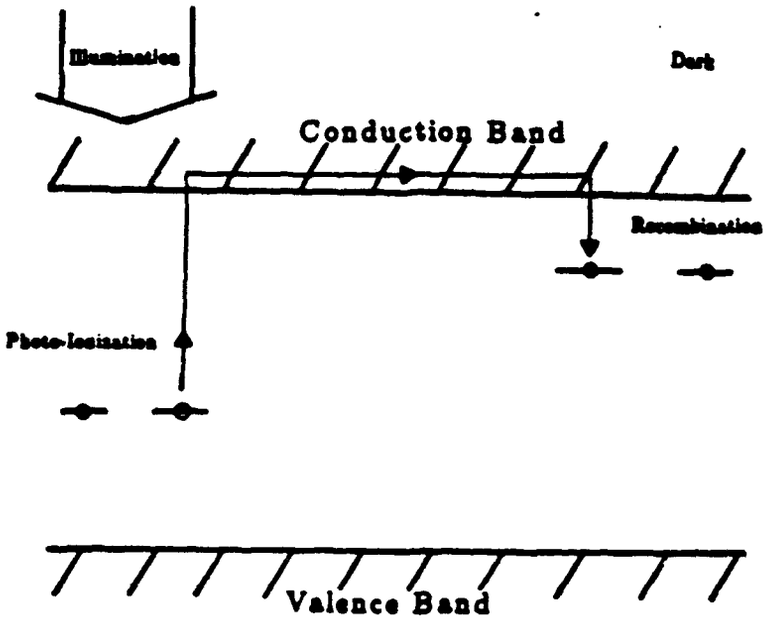

Figure 1: Basic mechanism of the photorefractive effect. Photoexcited electrons are redistributed, resulting in a space-charge field which modulates the refractive index through the electrooptic effect.

Chen was the first to devise the standard experiment for studying the photorefractive effect. He realized that the refractive index variations could be used to store phase holograms in the crystal.[21] In his experiment, the interference fringes of two coherent plane waves intersecting in the crystal, produced a pure phase grating through the photorefractive effect. This enables characterization of the effect in a crystal by measuring the diffraction efficiency of a light induced grating. In one experiment, more than 100 gratings were recorded in a $LiNbO_3$ crystal.[22]

Since this early work, the photorefractive effect has been used in a large number of nonlinear optical applications. The most widely known of these is optical phase conjugation.[23,24,25] This will be discussed in Chapter 6. Other applications include; image subtraction,[26] associative holographic memories,[27] phase-locking of lasers,[28] and optical bistability.[29] While many of these applications have shown great promise in the optical signal processing field, it is a promise which has so far been fruitless, since these applications are confined to relatively few research laboratories. Some of the reasons photorefractive materials have not been successfully integrated into useful devices are (1) a lack of a clear understanding of the photorefractive centers and their role in the photorefractive process, and (2) several anomalous photorefractive scattering processes that tend to degrade device performance. Other considerations are more in the nature of engineering problems such as the requirements of stability

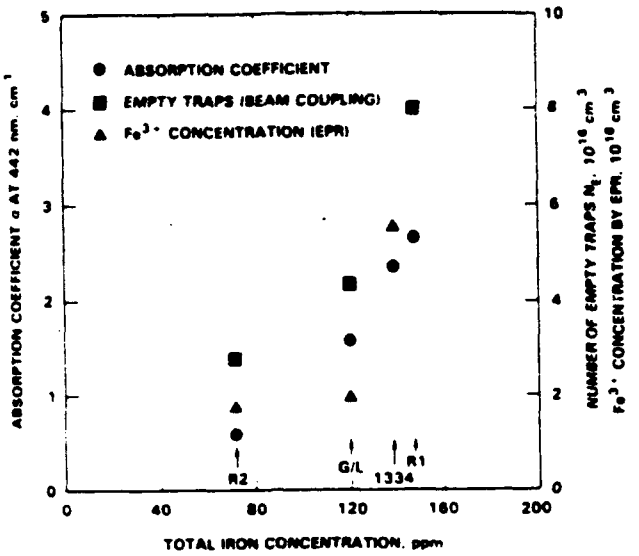

Figure 2: Correlation between iron concentration and the photorefractive trap density in $BaTiO_3$. (After Ref. 34)

and coherence needed for holography.

Identification of the photorefractive species in $LiNbO_3$ was attempted in the early seventies by Peterson et al. [30] Their method was to combine a number of techniques such as electron spin resonance, oxidation and reduction, and optical absorption to correlate the affects of selected doping on the photorefractive properties. They measured the diffraction efficiency of undoped crystals and crystals doped with 450 ppm Fe. The diffraction efficiency of the doped crystals was found to be two orders of magnitude larger than the undoped crystals. After annealing in a reduced oxygen partial pressure the diffraction efficiency of all the crystals was smaller than that of the as-grown or air-annealed crystals.

Their ESR measurements indicated that the dominant valence state of the iron in the as grown crystal was Fe^{+3}. Since the reduced crystals showed both a decrease in the diffraction efficiency and a decrease in the Fe^{+3} ESR signal, they concluded that the predominant photorefractive species in $LiNbO_3$ was Fe^{+3}. Unfortunately, most of the early photorefractive work did not include light-induced grating erasure and although there has been some work on the erasure rate kinetics, [31, 32, 33] the intensity dependence of the erasure rate has not been reported. Therefore, it is not known if the decay rate of $LiNbO_3$ exhibits a sublinear intensity response. Also, photo-induced absorption effects were not reported.

The first attempts to determine the photorefractive species in $BaTiO_3$ were only recently attempted by Klein and Schwartz. [34] Their research was patterned after that of Peterson et al. [30] with the exception that they used beam coupling to characterize the photorefractive effect. Chemical analyses of the crystals showed

that iron was the predominant impurity in their commercial samples, although other transition metal impurities were also present. These iron concentrations also seemed to correlate to the Fe^{+3} ESR signals from the samples. Since the beam coupling results showed a linear correlation to the iron concentration, they concluded that iron was also the dominant photorefractive species in $BaTiO_3$. Their data showed a four-fold increase in the trap density for only a two-fold increase in the iron concentration Fig. 2.

This result however, is in direct conflict with the results of Schunemann et al. [35] and the work presented in this thesis. The origin of this conflict is not completely understood, however the crystals used in this work were grown from purified materials and systematically doped with varying amounts of iron, constituting a better control group.

Ducharme and Feinberg [36] conducted oxidation reduction experiments on similar commercially available samples of $BaTiO_3$. They found that the dominant carrier, which was holes in as grown and oxidized crystals, could be converted to electrons after reduction at 650°c at a partial pressure of 10^{-6} atm. The sublinear intensity dependence of the decay rate usually observed for $BaTiO_3$, [37] was observed for their as grown and oxidized crystals. However, the crystals which had been converted to n type exhibited a linear intensity dependence for the decay rate.

1.2 References : Section 1

1. P. A. Franken, A. E. Hill, and G. Weinreich, "Generation of optical harmonics,"Phys. Rev. Lett. 7, 118 (1961)
2. R. C. Miller, "Optical second harmonic generation in piezoelectric crystals," Appl. Phys. Lett. 5, 17 (1967)
3. J. A. Giordmaine, and R. C. Miller, "Tunable coherent parametric oscillation in $LiNbO_3$ at optical frequencies," Phys. Rev. Lett. 14, 973 (1965)
4. C. C. Wang and G. W. Racette, "Measurement of parametric gain accompanying optical difference frequency generation," Applied Physics Lett. 6, 169 (1965)
5. G. E. Francois, "CW Measurements of the optical nonlinearity of Ammonium Dihydrogen Phosphate," Phys. Rev. 143, 597 (1966)
6. S. A. Akhmanov, A. I. Korrigin, V. A. Kolosov, A. S. Piskarskas, V. V. Fadeev, and R. V. Khokhlov, "Tunable parametric light generator with KDP crystal," Sov. Phys. J. Expt. Theor. Phys. Lett. (Engl. transl.), 3, 241 (1966)
7. J. E. Geusic, H. J. Levinstein, J. J. Rubin, S. Singh, and L. G. van Uitert, "Continuous 0.532-μ solid state source using $Ba_2NaNb_5O_{15}$," Appl. Phys. Lett. 12, 306 (1968)
8. A. Ashkin, G. Boyd, J.M. Dziedzic, R.G. Smith, A.A. Kallman, J.J. levinstein, and K.Nassau , "Optically-Induced Refractive Index Inhomogeneties in $LiNbO_3$ and $LiTaO_3$, Appl. Phys. Lett. 9, 72 (1966)
9. B. W. Faughnan and Z. J. Kiss, "Photoinduced reversible charge-transfer processes in transition-metal-doped single-crystal SrTiO3 and TiO_2." Phys. Rev. Lett. 21 (1968)
10. B. W. Faughnan and Z. Kiss, "Optical and EPR studies of photochromic $SrTiO_3$ doped with Fe/Mo and Ni/Mo," IEEE J. Quantum Electron. 5, 17 (1969)
11. F.S. Chen, "Optically Induced Change of Refractive Index in $LiNbO_3$ and $LiTaO_3$ ", J. Appl. Phys. 40, 3389 (1969)
12. R. L. Townsend and J. T. LaMacchia, "Optically Induced Refractive Index Changes in $BaTiO_3$" , J. Appl. Phys. 41, 5188 (1970)
13. J. B. Thaxter, "Electrical Control of Holographic Storage in Strontium-Barium Niobate", Appl. Phys. Lett., 15, 210 (1969)
14. J. J. Amodei, D. L. Staebler, and A. W. Stephens, "Holographic Storage in Doped Barium Sodium Niobate", Appl. Phys. Lett. 18, 507 (1971)

15. P. Gunter, U. Fluckiger, J. P. Huingnard, and F. Micheron, "Optically Induced Refractive Index Changes in $KNbO_3$:Fe ", Ferroelectrics 13, 297 (1976)

16. M. Peltier and F. Micheron, "Volume Hologram Recording and Charge Transfer Process in $Bi_{12}SiO_{20}$ and $Bi_{12}GeO_{20}$ ", J. ppl. Phys. 48, 3683 (1977)

17. M. B. Klein, "Beam Coupling in Undoped GaAs at 1.06 mm Using the Photorefractive Effect ", Opt. Lett. 9, 35 (1984)

18. R. A. Bartolini, A. Bloom, and H. A. Weakliem, "Volume Holographic Recording Characteristics of an Organic Medium ", Appl. Opt. 15 (1975)

19. F. Micheron, C. Mayeux, A. Hermosin, and J. Nicholas, "Holographic Storage in PLZT Ceramics" ,J. Amer. Ceram. Soc. 57, 306 (1974)

20. J. W. Burgess, R. J. Hurditch, C. J. Kirkby, and G. E. Scrivener, " Holographic Storage and Photoconductivity in PLZT Ceramic Materials ", Appl. Opt. 15, 1550 (1976)

21. F. S. Chen, J.T. LaMacchia,and D.B. Fraser, "Holographic Storage in Lithium Niobate", Appl. Phys. Lett. 13, 72 (1969)

22. D.L. Staebler, W.J. Burke, W.Phillips, and J.J. Amodei, "Multiple Storage and Erasure of Fixed Holograms in Fe-Doped $LiNbO_3$" ,Appl. Phys. Lett. (1975)

23. J. Feinberg and R. W. Hellwarth, "Phase-conjugating mirror with continuous wave gain," Opt. Lett. 5, 519 (1980)

24. P Hellwarth, "Generation of time-reversed wave fronts by nonlinear refraction," J. Opt. Soc. Am. 67, 1 (1977)

25. A. Yariv and D. Pepper, "Amplified reflection, phase conjugation, and oscillation in degenerate four-wave mixing," Opt. Lett. 1, 16 (1977)

26. S. Kwong, G. Rakuljic, and A. Yariv, "Real time image subtraction and "exclusive or" operation using a self-pumped phase conjugate mirror," Appl. Phys. Lett. 48, 20 (1986)

27. B. H. Stoffer, G. J. Dunning, Y. Owechko, and E. Marom, "Associative holographic memory with feedback using phase-conjugate mirrors," Opt. Lett. 11, 118 (1986)

28. J. Feinberg and G. D. Bacher, "Phase-locking lasers with phase conjugation," Appl. Phys. Lett. 48, 3 (1986)

29. R. W. Eason and A. M. Smout, "Bistability and noncommutative behavior of multiple beam self-pulsing and self-pumping in $BaTiO_3$," Opt. Lett. 12, 51 (1986)

30. G. E. Peterson, A. M. Glass, and T. J. Negran, "Control of the susceptibility of lithium niobate to laser-induced refractive index changes," Appl. Phys. Lett. 19, 130 (1971)

31. J. K. Tyminski and R. C. Powell, "Analysis of the decay dynamics of laser induced gratings in $LiNbO_3$," J. Opt. Soc. Am. B2, 440 (1985)

32. J. Baquedano, M. Carrascosa, L. Arizmendi, and J. Cabrera, "Erasure kinetics and spectral dependence of the photorefractive effect in Fe:$LiNbO_3$," J. Opt. Soc. Am. B 4, 309 (1987)

33. M. Carrascosa, and F. Agullo-Lopez, "Kinetics of optical erasure of sinusoidal holographic gratings in photorefractive materials," IEEE J. Quan. Electron. 22. 1369 1986

34. M. B. Klein and R. N. Schwartz, "Photorefractive effect in $BaTiO_3$: microscopic origins." J. Opt. Soc. Am. B 3, 293 (1986)

35. P. G. Schunemann, D. A. Temple, R. S. Hathcock, H. L. Tuller, H. P. Jenssen, D. R. Gabbe.and C. Warde, "Photorefractive effect in high purity $BaTiO_3$." Conference on Lasers and Electro-Opt., Technical Digest Series 14, 178 1987.

36. S. Ducharme and J. Feinberg , " Altering the Photorefractive Properties of $BaTiO_3$ by Reduction and Oxidation at 650 °C " , J. Opt. Soc. Am. B 3, 283 (1986)

37. S. Ducharme and J. Feinberg , " Speed of the photorefractive effect in a $BaTiO_3$ single crystal." J. Appl. Phys. 56. 839 (1984)

2 Barium Titanate: Physical Properties and Crystal Growth

The electrical and optical properties of Barium titanate have been studied intensively over the past forty years with much of this work performed at the MIT Laboratory for Insulation Research. This section primarily serves to give background on the material properties of $BaTiO_3$ relevant to the photorefractive effect.

2.1 Physical Properties

Above 130 ^{0}C, barium titanate exists in the cubic perovskite structure, ABO_3, shown in Fig. 2.1. [1] In this structure, the Ti^{4+} ions (B), are at the center of six O^{2-} ions forming regular octahedrons. The octahedrons are connected at the corners with Ba^{2+} ions, (A), occupying holes in this framework. Each Ba^{2+} ion is surrounded by twelve equidistant O^{2-} ions.

As the temperature is lowered below 130 ^{0}C, $BaTiO_3$ experiences three first order ferroelectric phase transitions. At 130 °C the unit cell becomes distorted along a [100] direction and the crystal symmetry reduces to tetragonal 4mm. It is believed that the Ti and O ions move to new equilibrium positions in opposite directions [see Fig. 4] resulting in a net polarization. This model was shown to fit neutron and x-ray diffraction data with the barium ions not contributing to the polarization. [1] Since this shift can occur in any one of six directions, cooling through the Curie temperature causes simultaneous nucleation of multiple domain structures in the crystal.

The first order electrooptic effect has it's origin in the quadratic electrooptic effect. To understand this consider the cubic structure of $BaTiO_3$ above 130 °C. In this phase the refractive index is isotropic. However, if we apply an electric field to the crystal we can induce birefringence through the quadratic electrooptic effect [2]

$$\Delta\left(\frac{1}{n^2}\right) \propto P^2 . \tag{1}$$

In this case the polarization P is the result of the applied field E.

Now consider the same $BaTiO_3$ crystal below 130 °C. In this tetragional phase there is a spontaneous polarization P_s and from Eq. 1 we expect that the crystal should be naturally birefringent. When an electric field E is applied to the crystal the net polarization P is composed of both the spontaneous polarization P_s and the polarization due to applied fields P_E. From Eq. 1 we see that the change in the refractive index now has several terms with

$$\Delta\left(\frac{1}{n^2}\right) \propto P_s^2 + P_E^2 + P_s P_E . \tag{2}$$

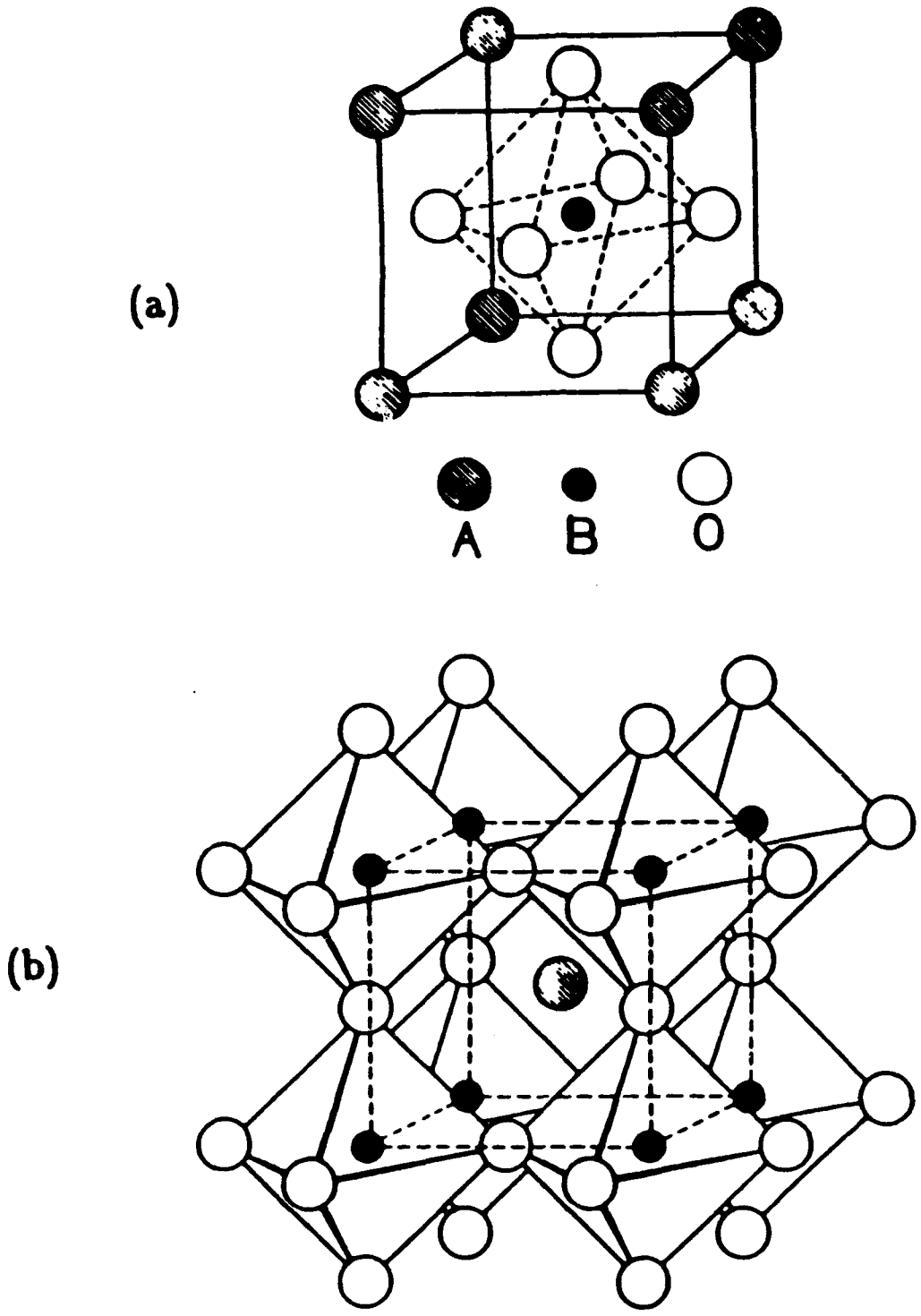

Figure 3: Perfect perovskite structure showing (a) the unit cell centered around the Ti^{+4} ion, and (b) the TiO_6 octahedra surrounding the Ba^{+2} ion. (After Ref. 1).

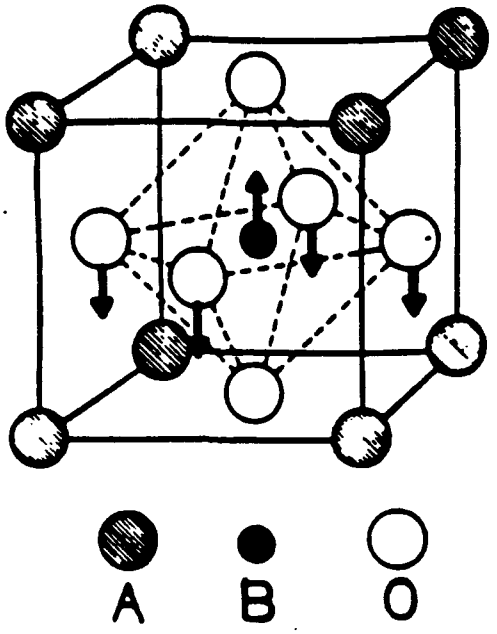

Figure 4: Ionic displacement in tetragonal $BaTiO_3$.

As stated, the natural birefringence is due to the spontaneous polarization P_s, with n_o-n_e $\propto P_s^2$. For small applied fields we can neglect the P_E^2 term. This leaves the cross term which is known as the first order electrooptic effect. Taking into account the tensoral properties of the crystal, the electrooptic effect can be written as [3]

$$\Delta n_{ij} = -\frac{n_i^3}{2} r_{ijk} E_k \tag{3}$$

where r_{ijk} is known as the electrooptic tensor. Using the symmetry properties of the tetragonal phase 4mm, the allowed tensor elements are $r_{131}=r_{311}=r_{232}=r_{322}$, $r_{113}=r_{223}$, and r_{333}. [3]

The two remaining phase transitions are found to be very destructive. Below 5 °C, the unit cell distorts to mm orthorombic symmetry with the spontaneous polarization along the [110] directions. Finally, below -90 °C, the spontaneous polarization is along the [111] direction with 3m trigonal symmetry.

The room temperature tetragonal phase is the one of interest to most optics researchers since its both ferroelectric and electrooptic with only a only a slight elongation of the unit cell in the polar direction.

2.2 Crystal Growth and Preparation

At present, the best technique of growing single crystalline $BaTiO_3$ is the top-seeded solution growth technique developed at the MIT Crystal Physics and Optical Electronics Laboratory. In this method, a solution of BaO and TiO_2 is prepared using

the phase diagram shown in Fig. 6(a). A composition of 66%TiO_2 and 34%BaO is found to give the widest growth range. The furnace, Fig. 2.2, is heated by silicon carbide heating elements and the thermal gradients are kept low by insulating fire bricks. The temperature is raised to approximately 1400 ^{0}C and a [100] seed of $BaTiO_3$ is introduced into the furnace above the melt. After equilibrium is reached, the seed is introduced into the melt. To initiate growth, the temperature is slowly lowered at approximately 0.4 ^{0}C/hr. After 5 to 10 hours, the seed is pulled from the melt at a rate of 0.2 to 1.0 mm/hr. After about 60 hours of pulling, the crystal is removed from the melt and the furnace slowly cooled to room temperature.

Because of the large differences in the size of Ba and Ti ions, doping is expected to be highly site selective. For instance, the transition metals are all similar in radius to the Ti ion, while the rare earth ions are closer in radius to the Ba ion. Therefore Fe^{+3} would be expected to be incorporated in the lattice at the Ti^{+4} site, while Ce would probably reside in the Ba site.

The first attempt at doping was made on crystals grown from a melt containing reagent grade TiO_2 and $BaCO_3$. These crystals were light green in color before doping. The addition of 20 ppm Cr to the melt, $\{0.66[(1\text{-}x)\,TiO_2 + x\,Cr_2O_3] + 0.34\,BaO\}$, resulted in crystals which were very dark red in color. Although these were not useful for the normal photorefractive studies, the strong beam fanning discussed in Chapter 6 was first seen in these crystals.

The second doping attempt was made on crystals known as nominally pure, that is, they were grown from a melt containing relatively pure TiO_2 and reagent grade $BaCO_3$. Crystals of this type are the same as those reported in the literature. These crystals were found to have a light yellow-orange color. The addition of 20 ppm Ce to the melt, $[0.66TiO_2 + 0.34(1\text{-}x)BaO + 0.34(x)CeO_2]$, resulted in moderately dark red samples. Strong beam fanning was observed in the Ce doped samples and photorefractive characterization was again hindered.

The third attempt at doping was performed by Peter Schunemann on a melt containing TiO_2 which he purified through a distillation process and $BaCO_3$ purified by David Gabbe through a solvent extraction processes. The undoped crystals showed very little absorption in the visible. The doped crystals were prepared by substituting Fe for Ti in the melt $[0.66(1\text{-}x)TiO_2 + 0.66(x/2)Fe_2O_3 + 0.34BaO]$ where x is the doping level. The melt doping levels were 50 ppm, 500 ppm, and 1000 ppm. The color of the as-grown doped samples varied from light yellow for the 50 ppm to brown for the 1000 ppm. The visible absorption in 50 ppm and 500 ppm crystals was small enough to allow photorefractive characterization.

Crystal growth from a $BaTiO_3$ Ba_2O_4 melt [see Fig. 6(b)] was also attempted. This has the potential of increasing the growth range and lowering the growth temperature. In this case only one growth run was attempted. The composition used was $[0.4B_2O_3 + 0.6TiO_2 + BaO]$ and the resulting seeding temperature was 1287^0. This melt seemed to be extremely viscous and the resulting crystal was simply a mass of dendritic growth. However, recently crystals have been successfully grown

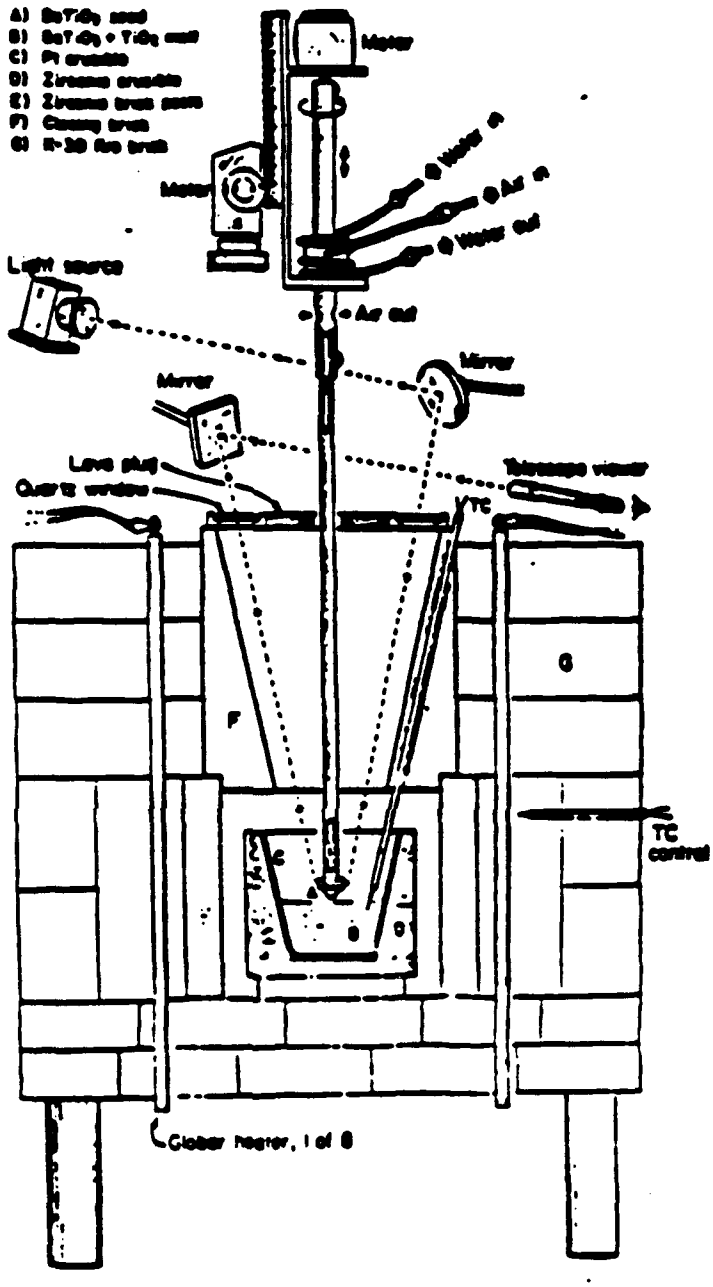

Figure 5: Schematic diagram of a typical furnace used for top-seeded solution growth of oxide crystals. (After Ref. 4).

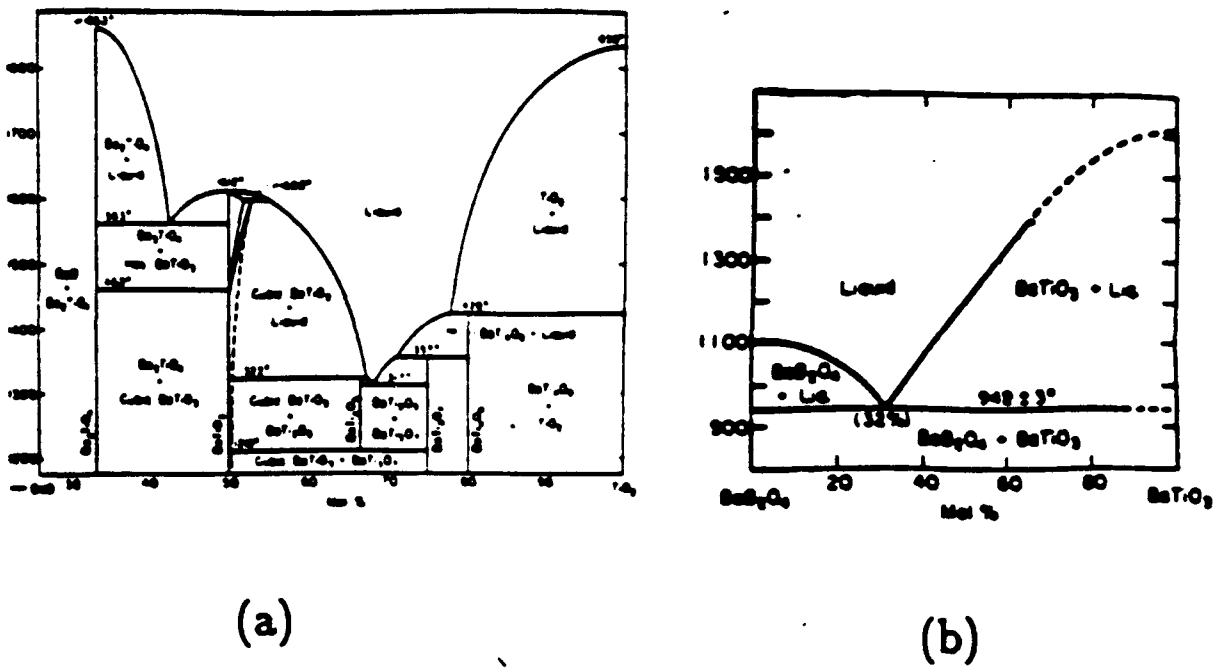

Figure 6: (a) The BaO-TiO_2 phase diagram and (b) the BaB_2O_4-$BaTiO_3$ phase diagram. (After Refs. 6 and 7)

from a similar melt by David Gabbe. [5]

As a final note, a weighing error by the author lead to a melt with approximately a 50/50 BaO/TiO_2 ratio. This resulted in a crystal which was extremely cracked and very unsymmetric. X-ray diffraction data taken by David Gabbe showed this crystal to have a hexagonal structure as expected by the phase diagram Fig. 6(a).

Since the Curie point is around 130 ^{o}C, crystals cut from the boules are found to have twinning of 90^{0} domains as shown in Fig. 7. These crystals are cut along [100] directions and polished first with 20 micron grit and then 3 micron diamond paste. The domains are eliminated by two methods. First the samples are subjected to hydrostatic pressure alternately along two perpendicular axes to eliminate the twinning. After each cycle the crystal must be repolished due to surface changes which can result in cracking if the poling were continued. This mechanical poling removes the 90^{o} domains leaving only the domains which are 180^{0} apart. These are aligned by heating the crystal near or above the Curie temperature, applying an electric field of approximately 1000 V/cm, and then slowly cooling the sample back to room temperature. Figure 8(a) shows the typical domain structure of an unpoled crystal placed between cross polarizers. Figure 8(b) shows the same crystal after mechanical and electrical poling with the c-axis parallel to the page and the long axis of the crystal. The size difference is due to the successive repolishing of the crystal during the poling cycles.

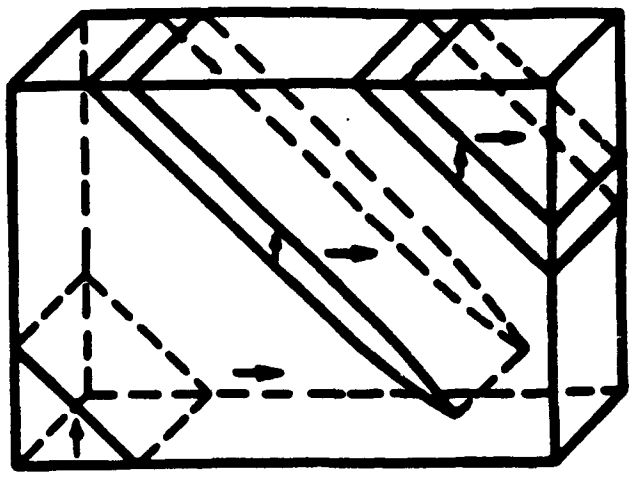

Figure 7: Domain twinning in $BaTiO_3$. The arrows denote the polar axis (After Ref. 1).

Figure 8: Photographs of a $BaTiO_3$ crystal (a) unpoled and (b) poled. The crystal was placed between crossed polarizers and in (b) the c-axis is parallel to the page.

Three samples doped with 50 ppm, 500 ppm, and 1000 ppm Fe were electroded on the c faces, placed in a quartz tube and annealed at 800 °C in an argon atmosphere with 100 ppm oxygen (10^{-4} atm) for 36 hours. The samples were then quenched to 175 °C by moving the quartz tube to another furnace at 175 °C. A poling field was then applied and the temperature slowly lowered to room temperature at a rate of approximately 5 °C/hour. [9, 8]

2.3 References : Section 2

1. A. von Hippel, *Dielectrics and waves* , (The MIT Press, Cambridge Massachusetts 1954)
2. G. Burns, Solid State Physics, (Academic Press, Inc. New York, 1985)
3. J. F. Nye, Physical properties of crystals, (Oxford University Press, London 1957)
4. V. Belruss, J. Kalnajs, A. Linz and R. Folweiler, "Top-Seeded solution growth of oxide crystals from non-stoichiometric melts," ater. Res. Bull. 6, 899 (1971)
5. David Gabbe, (private communication)
6. D. E. Rase and R. Roy, J. Am. Ceram. Soc. 38, 111 (1955)
7. Y. Goto and L. Cross, Yogyo Kyokai Shi 77, 355 (1969)
8. P. G. Schunemann, D. A. Temple, R. S. Hathcock, C. Warde, H. L. Tuller, and H. P. Jenssen. "Effects of iron concentration on the photorefractive properties of $BaTiO_3$," Accepted for publication in the J. Opt. Soc. Am. B Feature Issue on Photorefractive Materials, Effects and Devices, August 1988.
9. Peter Schunemann, Masters Thesis, MIT (1987)

3 Improved Furnance Design and Assembly, and BaO-B_2O_3-TiO_2 Growth System

3.1 $BaO-TiO_2$ System

The binary system $BaO-TiO_2$ was studied by Rase and Roy(1) who found that the phase field for crystallization of $BaTiO_3$ from the melt extends from 60 to 34 mol% BaO. On the BaO rich side of stoichiometric $BaTiO_3$, the lowest liquidus temperature is ~1450 and only hexagonal $BaTiO_3$ crystallizes from the melt. On the TiO_2 rich side, hexagonal $BaTiO_3$ solid solution crystallizes from 50 mol% TiO_2 at 1650C to 60% TiO_2 at ~1600 C. From that composition and temperature a cubic solid solution is shown to crystallize, decreasing to virtually zero width at 65 mol% TiO_2 and 1460C. Cubic stoichiometric $BaTiO_3$ crystallizes up to the next transition which is either the incongruent melting point of $BaTi_2O_5$ or the eutectic with $BaTi_3O_7$. The existence of the incongruently melting $BaTi_2O_5$ is questionable and is not shown by all workers.

$BaTiO_3$ has a number of polymorphs, an orthorhombic form stable below ~5C, a tetragonal ferroelectric phase from ~5C to ~120C, a cubic phase from 120C to ~1460 C, and an hexagonal phase from ~1460 to the congruent melting point of 1650 C. Titanium rich hexagonal and cubic solid solutions stable above ~1460 are also known.

3.2 Crystal growth runs

A list of crystal growth runs carried out under this program is shown in Table 1. The runs were done with the multifold purposes of providing samples as well as investigating the effect of growth parameters and techniques on the formation of the cap. A series of runs was also carried out to investigate the utility and behavior of borate and fluoride-borate fluxes. In addition to the foregoing, runs carried out in the new cylindrical Zircar (Zircar Products, Inc., Florida NT) furnaces were also intended to test the furnace performance.

Table 1. Summary of Crystal Growth Runs.

RUN	CRYSTAL	NOTEBOOK	PAGE
1469	$BaTiO_3$	23	1w-2
1469(a)	$BaTiO_3$	23	2y-3w
1470	$BaTiO_3$	23	3w-5w
1472	$BaTiO_3$	23	5y-7w
1475	$BaTiO_3$	24	1-6
1476	$BaTiO_3$	23	7y-11y
1477	$BaTiO_3$	23	12w-14y
1497	$BaTiO_3$	24	19-24
1499	$BaTiO_3$	24	25-31
1504	$BaTiO_3$	24	32-35
1507	$BaTiO_3$:Cr(5ppm)	24	37-41
1517	$BaTiO_3$:Cr(5ppm)	24	43-47
1518	$BaTiO_3$	23	26w-27y
1524	$BaTiO_3$:Cr(5ppm)	24	48-53
1532	$BaTiO_3$:Cr(10ppm)	24	54-57
1534	$BaTiO_3$:Cr(10ppm)	24	59-62
1535	$BaTiO_3$:Cr(10ppm)	24	63-66
1538	$BaTiO_3$:Cr(10ppm)	24	67-72
1540	$BaTiO_3$:Cr(10ppm)	24	73-76
1542	$BaTiO_3$:Cr(10ppm)	24	77-80
1543	$BaTiO_3$:Cr(10ppm)	24	81-84
1545	$BaTiO_3$:Cr(30ppm)	24	85-87
1547	$BaTiO_3$:Cr(10ppm)	24	89-91
1549	$BaTiO_3$:Cr	24	92-94
1550	$BaTiO_3$:Cr	24	95-97
1596	$BaTiO_3$	26	1w-2y
1601	$BaTiO_3$	26	3w-3y
1Z	$BaTiO_3(BaB_2O_4\text{-}BaF_2)$	2Z	2w-5w
2Z	$BaTiO_3(BaB_2O_4\text{-}BaF_2)$	2Z	6w-12w
3Z	$BaTiO_3(BaB_2O_4\text{-}BaF_2)$	2Z	12y-15w
4Z	$BaTiO_3(BaB_2O_4\text{-}BaF_2)$	2Z	15y-16y
5Z	$BaTiO_3(BaB_2O_4\text{-}BaF_2)$	2Z	17w-19y
6Z	$BaTiO_3(BaB_2O_4\text{-}BaF_2)$	2Z	20w-23w
7Z	$BaTiO_3(BaB_2O_4\text{-}BaF_2)$	2Z	24w-25w
8Z	$BaTiO_3(BaB_2O_4\text{-}BaF_2)$	2Z	25y-28y
9Z	$BaTiO_3(BaB_2O_4\text{-}BaF_2)$	2Z	30y-34w
12Z	$BaTiO_3$	2Z	35y-38y
14Z	$BaTiO_3$	2Z	39y-41w
16Z	$BaTiO_3$	2Z	41y-43w
24Z	$BaTiO_3(BaB_2O_4)$	1Z	16w-18y
24Z	$BaTiO_3(BaB_2O_4)$	1Z	16w-18y
27Z	$BaTiO_3(BaB_2O_4)$	1Z	19w-20w
29Z-A	$BaTiO_3(BaB_2O_4)$	1Z	20y-21w
29Z-B	$BaTiO_3(BaB_2O_4)$	1Z	21w-22w
29Z-C	$BaTiO_3(BaB_2O_4)$	1Z	22w-23y
32Z	$BaTiO_3(BaB_2O_4)$	1Z	24w-26y
35Z	$BaTiO_3(BaB_2O_4)$	1Z	27w-27y
36Z	$BaTiO_3(BaB_2O_4)$	1Z	28w-30w
37Z	$BaTiO_3(BaB_2O_4\text{-}BaF_2)$	1Z	30y-38w

3.3 Top Seeded Solution Growth of $BaTiO_3$ - Review

In early work(2), $BaTiO_3$ was grown from a flux containing KF and PbO . In addition to incorporation of flux ions as impurity dopants, the crystals grew with a thin, plate-like morphology characterized as butterfly wings on account of the appearance of the commonly occurring twins. Belruss et. al.(3) were the first to grow euhedral tetragonal $BaTiO_3$ single crystals from a melt in the BaO-TiO_2 system using the Top Seeded Solution method. They established that single crystals can be grown from composition starting at 34 mol% BaO-66 mol% TiO_2 with a liquidus temperature of ~1390 and extending to ~ 68 mol % TiO_2 at ~1330 as crystallization continued.

A resistance furnace, Figure 1, with low thermal gradients was used. Crystal growth was initiated on an oriented single crystal seed in the shape of a rectangular prism attached with platinum wire to closed end Pt-20%Rh tube or seed rod in the manner shown in Figure 2 . Air flowing through a coaxial inner tube cools the seed and allows some regulation of the thermal gradient required for crystal growth. Additional gradient control intended to reduce direct cooling of the melt surface by the seed rod is provided by an alumina sleeve. Crystal growth was driven by lowering the furnace temperature on the order of 0.5C/hr. Crystallization temperatures and yield were in good agreement with the phase diagram. However, intergrowth of other phases especially at the start of a crystal to form a cap of fractured inclusion filled material and a general disruption of crystallization occurring when the initial TiO_2 content of the melt is less than 66% are not explained by the phase diagram.

3.3.1 Brick Furnace

During the first part of this program, crystal growth was carried out in the furnace cited above. It was constructed of insulating firebrick and heated with twelve SiC (I Squared R Element Co., Inc., Akron, NY) resistance elements connected in parallel and mounted in a square pattern. Except for modernization of the temperature controls, few changes have been made to the design developed in this laboratory (3). Figure 1 shows a schematic of the furnace and pulling mechanism. The drill press stand and other furnace supports are not shown not shown.

Temperature is measured with a Pt-Pt 13%Rh thermocouple positioned between two heating elements and regulated by a Barber-Colman 570 programmable controller. A feedback controlled DC motor and variable ratio gearbox are used to set the pulling rate, while an uncontrolled variable speed motor is used for the seed rotation.

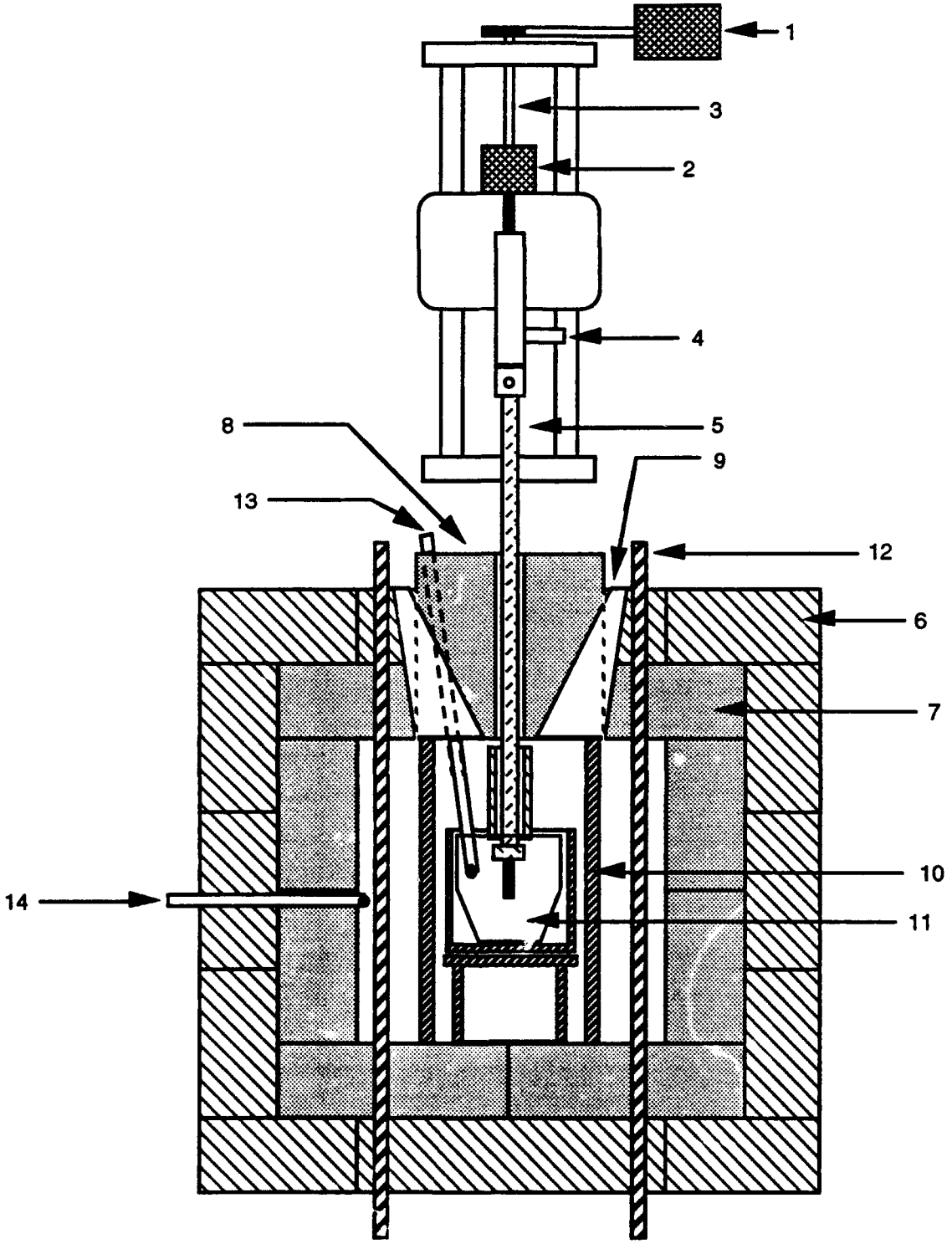

Figure 1. Cross section of the brick furnace. 1. pulling motor; 2. rotation motor; 3.lead screw; 4. cooling air inlet; 5. seed rod; 6. K20 firebrick; 7. K30 firebrick; 8. closing brick; 9. sight port with quartz window; 10. alumina muffle and furniture; 11. platinum crucible; 12. silicon carbide heating elements; 13. measuring thermocouple; 14. control thermocouple.

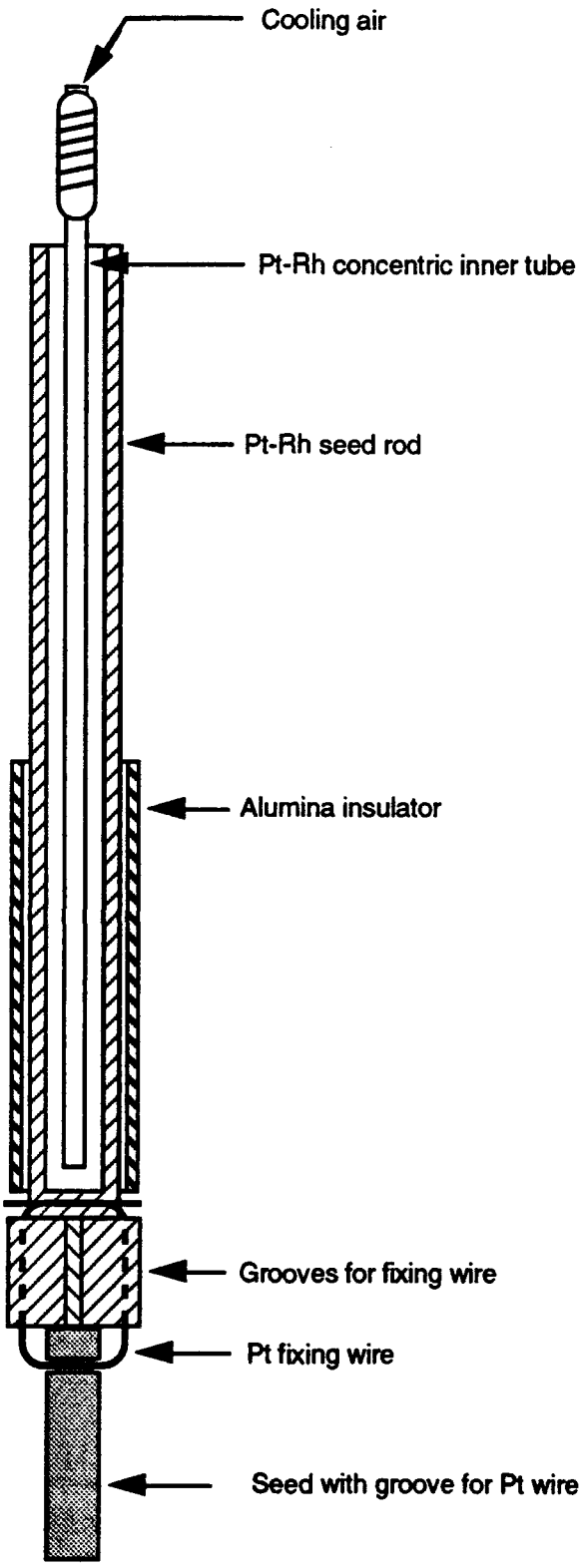

Figure 2. Cross section of the platinum seed rod and detail of a mounted seed.

The furnace is limited by certain design and operating characteristics. Silicon carbide elements age as a function of service time and temperature due to oxidation of the silicon dopant, resulting in an increase in resistance. Non-uniform ageing of a set of elements matched when new is typical, leading to asymmetry of the thermal field in the melt which causes irregular, off axis crystal growth and very likely contributes to the factors causing temperature fluctuations which give rise to stress and defect formation.

At the growth temperature of ~1400 used for $BaTiO_3$, where the surface temperature of the heating elements is ~1450, a set of elements may last from 6 to 9 months. Higher temperatures needed for growth of Sr doped $BaTiO_3$ can be reached but ageing is so rapid that the element lifetime may be reduced to as little as six weeks.

Contamination of the melt by furnace components is problematic when purity is a significant factor. Firebrick is a fragile, friable material that releases dust to the crucible, especially when the closing brick is fitted into place at the start of the run. Vapor phase transport of iron and other impurities from hot bricks to the melt is suspected as being a serious source of contamination. To a limited extent, the use of a high purity alumina wash on the exposed brick surfaces alleviates these problems.

The furnace structure itself is inaccurate and asymmetric. It is constructed in house without the use of special jigs to ensure reproducible dimensions. Centering of the crucible and seed rod within the heater array is difficult and the bricks can shift position as the temperature is increased. The thermal field is asymmetric about the seed due to heating element placement and power dissipation variations, to asymmetric heat loss through the closing brick and to off center placement of other components. Prior experience in this laboratory has shown that successful crystal growth is influenced by these irregularities. In the worst case, which is not uncommon, the thermal center of the furnace is far from the seed axis and the crystal grows in a highly skewed and sometimes polycrystalline way.

3.3.2 Cystal Characteristics

When grown by the top seeded solution method in a low thermal gradient, $BaTiO_3$ forms a faceted, three dimensional crystal in contrast to the two dimensional butterfly wings that are obtained when growth is carried out from a PbO-KF flux under conditions of spontaneous nucleation. At the growth temperature, $BaTiO_3$ crystallizes as the cubic polymorph which transforms at ~ 120C to the tetragonal ferroelectric phase. The transition results in the formation of a polycrystalline material consisting of 90 and 180 degree domains which gives the crystal a cloudy appearance and

produces a characteristic pattern of tilts and boundaries visible on the surface of the facets.

Numerous reentrant angles are formed on the crystal surface at the intersections of facets. Liquid adheres to the crystal in the reentrant spaces and also forms a drop on the bottom when it is withdrawn from the melt at the end of a run. The liquid solidifies on cooling forming a layer that stresses the crystal and initiates cracks in the underlying material.

One of the most significant features of top seeded solution grown $BaTiO_3$ is the so called cap. (The cap is discussed more fully in a separate subsection.) The top portion of the crystal starting from the seed and extending several mm or more into the bulk, depending upon the shape and growth conditions, contains numerous inclusions and cracks which frequently extend into the inclusion free material beyond the cap. As a result, the size and number of samples that may be obtained from a given crystal is significantly reduced. Characterization of the cap and the conditions under which it forms has been studied in this program.

3.3.3 New Furnaces

Two new furnace types were developed under this program in response to the limitations and design characteristics of the brick furnaces. The goals of that effort were to have furnaces that are cleaner, more mechanically reproducible, constructed from commercially available parts, easier to clean, more uniform in temperature and more responsive to control action through reduced thermal mass. The first type called cylindrical because of its shape, uses conventional SiC elements, while the second called octagonal, the design of which was based on experience with the first, is heated with $MoSi_2$ elements. Both were obtained from Zircar Products.

3.3.3.1 Cylindrical Furnace

A new crystal growing furnace incorporating higher purity and less friable insulation than firebrick was built to specification by Zircar. Temperature and power control, crystal pulling and rotation were placed under computer control. Figure 3 shows a schematic of the furnace. Three concentric pieces of tubular insulation, each of a different thermal conductivity and temperature range are closed top and bottom by three discs of the same materials to form the furnace chamber. Fitted to the top of furnace is a plug with two viewing ports and a seed rod access hole. SiC heating elements are used. All of the interior ceramic parts are fabricated from 99.8% high

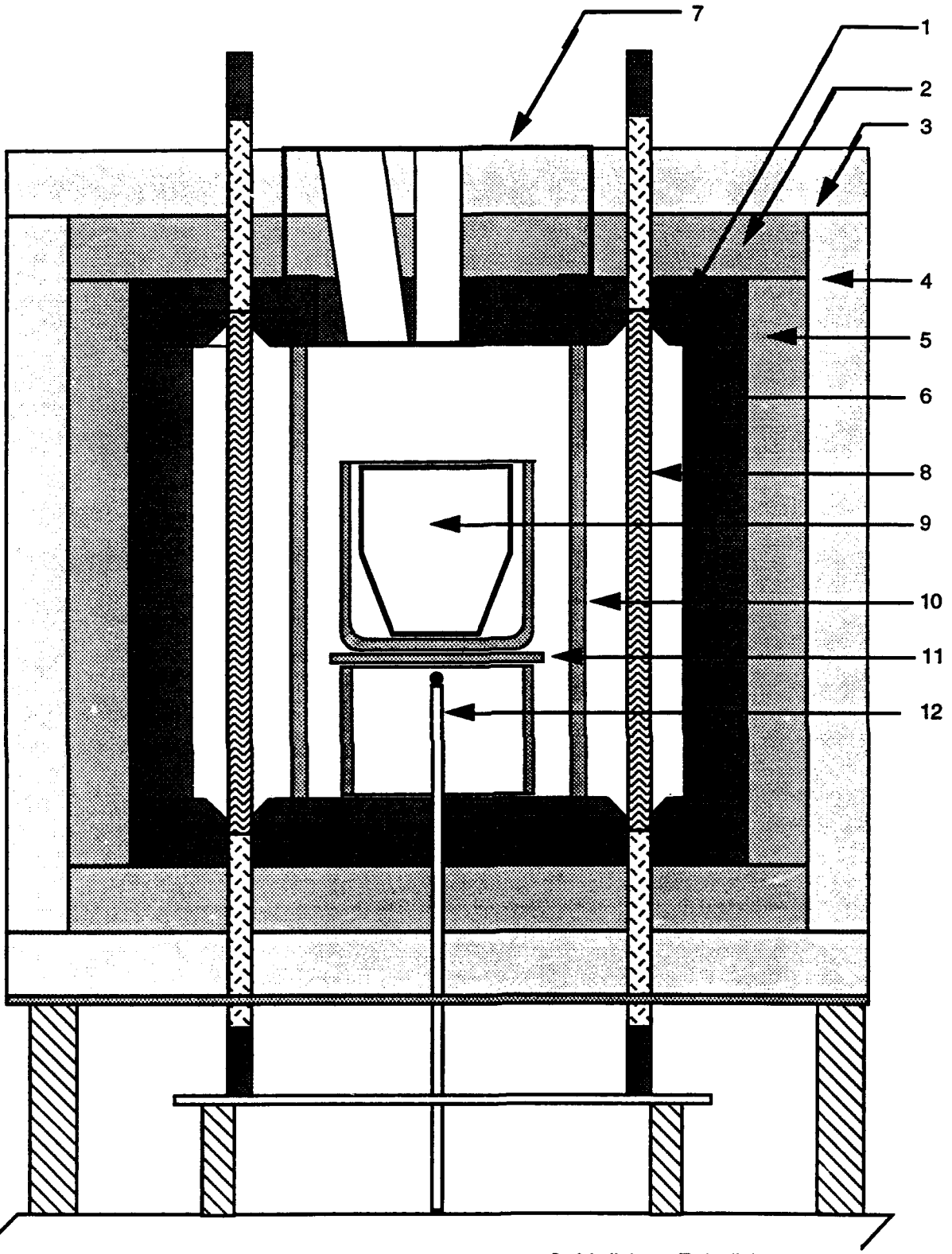

Figure 3. Cross section of the cylindrical zircar furnace. 1. SALI disk; 2. ZAL disk; 3. ASH disk; 4. ASH cylinder; 5. ZAL cylinder; 6. SALI cylinder; 7. layered plug; 8. silicon carbide heating element; 9. platinum crucible; 10. alumina muffle; 11. alumina furniture; 12. measuring and control thermocouple.

purity alumina (McDanel Refractory Co., Beaver Falls, PA or Ceramicon Designs Ltd., Golden CO). A cylindrical muffle separates the heating elements from the crucible chamber. The crucible is positioned inside a cup which is supported on a disc and a set of alumina rings of variable height. Measurement and control of the temperature is done with a Pt-Pt/Rh13% thermocouple positioned on the furnace axis 3 mm below the crucible supports. The pulling track and furnace are supported on a drill press stand and table.

3.3.3.2 Furnace Structure

The cylindrical Zircar furnaces were found to be susceptible to cracking due to expansion when heated and to shrinkage after being heated. Coefficients of expansion of the various grades of Zircar insulation used in assembling the nested set of cylinders are not available; however, the manufacturer's data does indicate ~ 1 to 3% shrinkage after being heated to the working temperature. With the furnace at a temperature of ~ 1200 to 1400C a 3/16" vertical crack opened in the outermost ASH cylinder and the topmost ASH disk was raised through expansion of inner components. Internal cracking of the inner cylinders and discs also occurred. Figure 4 shows the pattern of cracks observed when the furnace was demounted for service. The bold lines drawn across the ends of the cylinders indicate cracks that extend from top to bottom. The effect of expansion and movement of insulation on the the seed rod centering and thermal symmetry was not known. It appears that the crack pattern was stable with time and was of no consequence unless the furnace had to be disassembled for cleaning of a spill.

3.3.3.3 Ceramic Seed Rod

A ceramic seed rod, shown in Figure 5, was developed to replace the platinum rods. The purpose was to have a seed rod with improved characteristics including: straightness and concentricity, thermal contact to the seed, less influence on the furnace gradient and surface temperature of the melt

3.3.3.4 Heating Elements

The furnace is heated by eighteen SiC elements 3/8" dia x 16" long x 8" hot zone equally spaced in a circular pattern on the axis of the furnace. Three sets of six elements connected in parallel are wired in series, giving an overall resistance that does not require the use of a low voltage, high current transformer. Silicon carbide elements age as a function of use time and temperature. Two signs of ageing are an

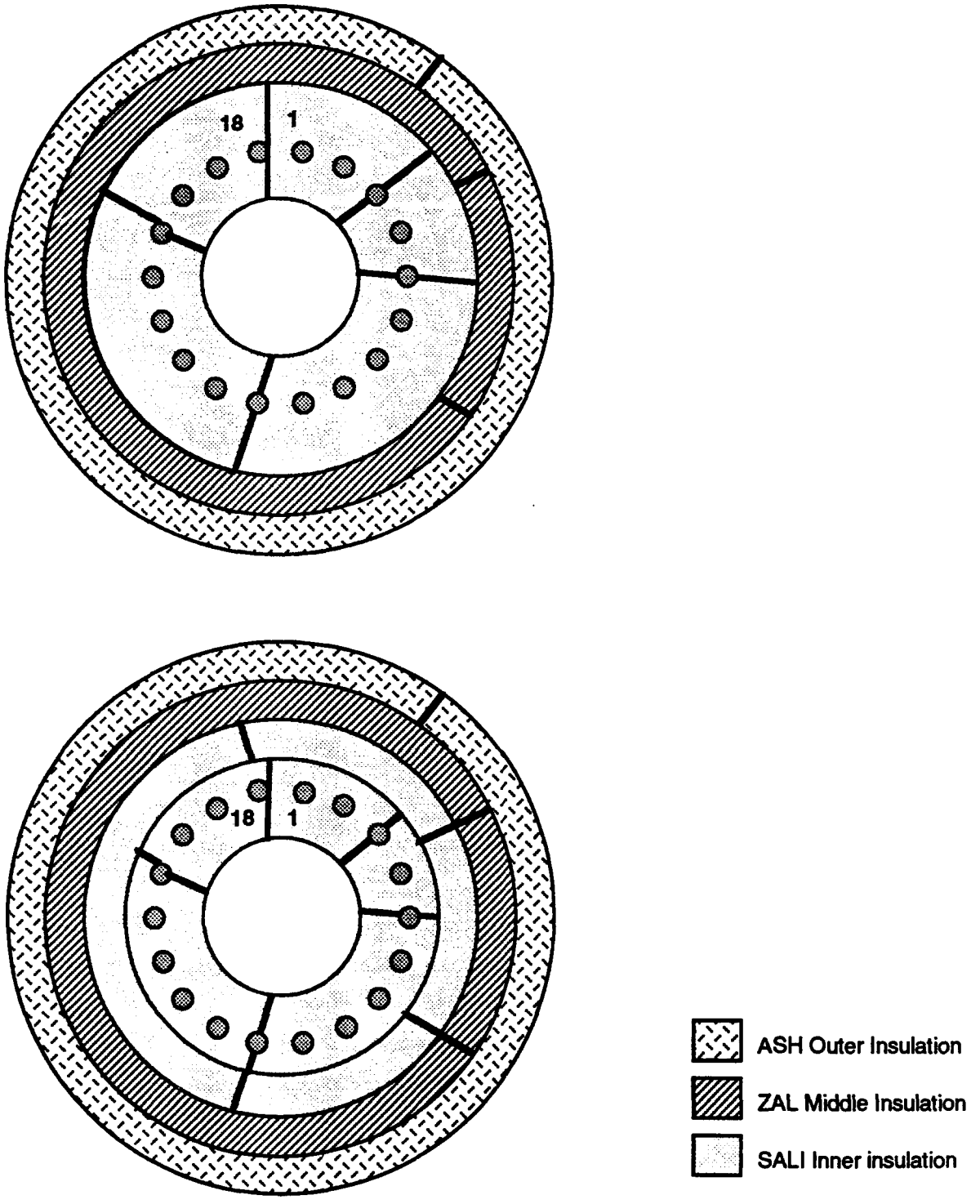

Figure 4. Pattern of cracks in the Zircar insulation. Top: the inner SALI disk covers the inner SALI cylinder. Bottom: the inner SALI disk cut away to expose the inner SALI cylinder.

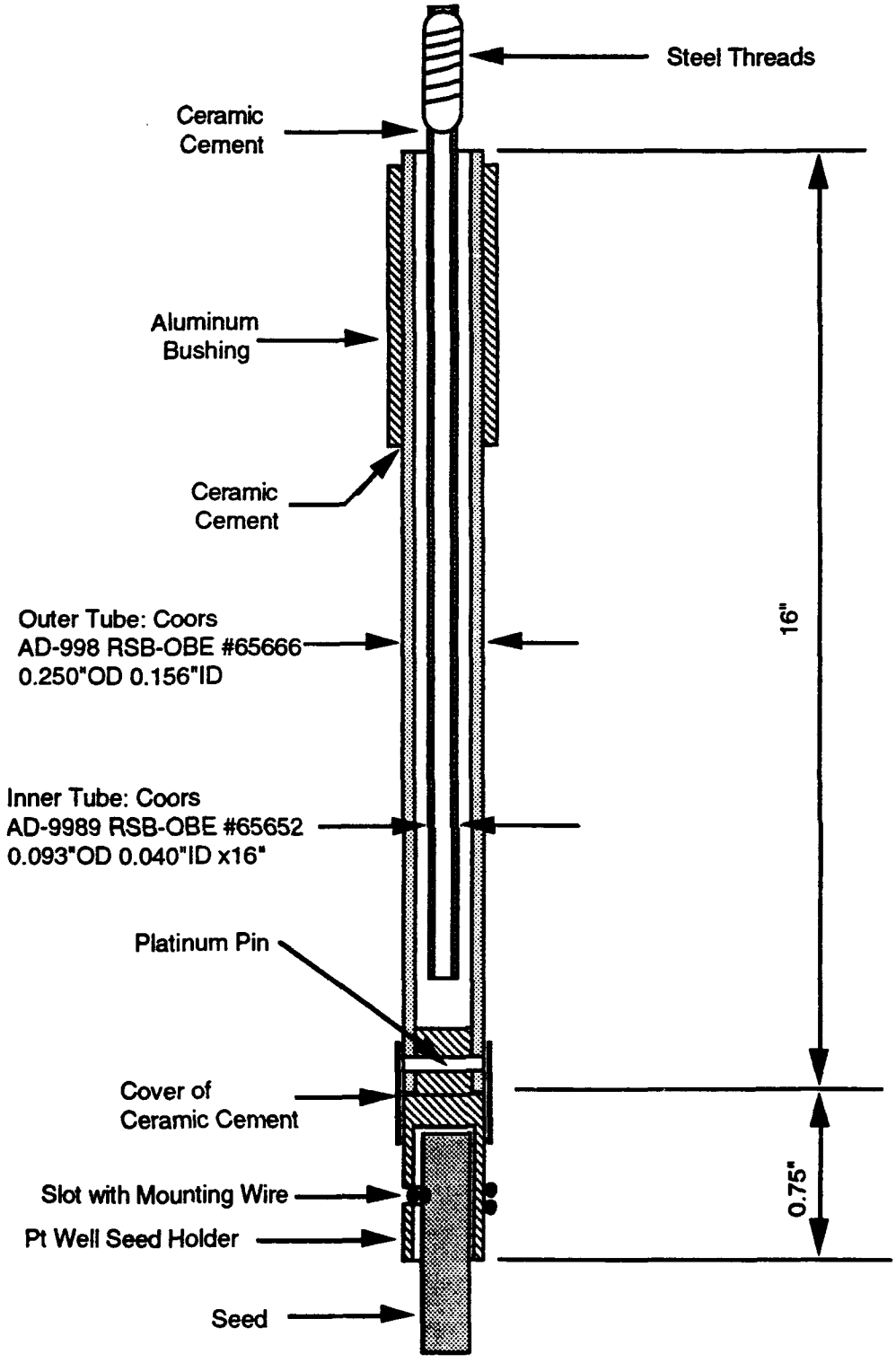

Figure 5. Cross section of the ceramic seed rod and detail of a mounted seed.

increase in resistance and visible physical deterioration. In an initially matched set, resistances diverge as a result if nonuniform ageing . This behavior is inhibited in the parallel wiring mode because the bars with the higher resistance, i.e. the most aged, dissipate the least power. In the series circuit bars, with the highest resistance dissipate the most power which accelerates the ageing. The series-parallel circuit used in the round furnaces is a compromise. Qualitative data indicates that elements in the round furnaces have a shorter lifetime than those in the brick furnaces. Silicon carbide elements have three distinct sections, a central hot zone, a low resistance cold end which extends through the furnace wall and a terminal end that is impregnated with aluminum for electrical contact. Compared with the elements used in the brick furnace, those used in the Zircar furnace have a shorter cold end to limit projection above the plane of the furnace top. As a result, at an operating temperature of ~1300, the terminal end on the top side of the furnace ran hot enough to cause oxidation of the aluminum and to draw the temper from the terminal clamps resulting in very poor electrical contact. The net effect of the SiC heating element behavior has been to limit the maximum temperature to ~1350 to avoid excessively rapid ageing. For continuing use of the furnace, new elements have been purchased with one inch longer cold ends that will project 2.5" from the top surface.

3.3.3.5 Pulling and Rotation

The pulling mechanism (Thompson Systems, Port Washington, NY) is a high precision linear slide driven by a ball screw. It is mounted to the drill press column with a standard table clamp. Predrilled holes allow direct mounting of a stepper motor to the screw. A spindle incorporating a gland for circulation of air through the seed rod is attached to the slide. The seed rod is rotated by a direct coupled stepper motor. Both motors are operated under computer control. This equipment allows precise control and display on the computer terminal of the rotation rate and seed position, the latter function being of great importance in correct nucleation of a crystal on a seed.

3.3.3.6 Thermal Symmetry

After setting up the furnace, its performance was evaluated in several growth runs carried out from a 66 mol% TiO_2 in the traditional way using a 100 seed attached to an air cooled Pt seed rod. Care was taken to center the crucible and seed rod to the furnace axis. Crystallization was typically asymmetric about the seed rotation axis indicating a distorted radial gradient not centered on the furnace center. This behavior

has been correlated with failed or very low output heating elements in numerous brick furnace runs.

A second observation was that of persistent formation of a crystal floating on the melt surface whose position could not be attributed to careless furnace assembly and seeding. The floater remained in one place but could be induced to change position as a function of the rotational position of the furnace plug and sight ports. These observations again indicate a disturbed radial gradient influenced by heat loss through the sight ports resulting in a local surface temperature equal to the liquidus temperature. For successful crystal growth, the liquidus temperature should occur at the crystal melt interface while temperatures elsewhere should be higher. Lack of motion of the floater may also indicate that there is little convective stirring in the melt.

Adjustment of thermal gradients is usually done by modulating the heat input and loss through changes in the heater and insulation configuration. At the temperatures required for $BaTiO_3$ growth, this is not practical because heater power input was close to the maximum allowed, as dictated by the element ageing characteristics.

3.3.4 Investigation of Seeding

This work was carried out in the brick furnaces. Seeding is the term for the technique of nucleating new growth on a piece of BaTiO3, usually in the form of an oriented single crystal prism. Initially, seeds are developed from polycrystalline or small, not necessarily oriented, single crystal fragments using an iterative crystal growth process to obtain larger single crystals and oriented seeds. Defects such as low angle grain boundaries and stress which can be reintroduced during seeding propagate into the growing crystal. Initial suspicions about the cap were that the technique of seeding played a role in its formation. One of the undertakings of this work was to investigate the seeding process and determine its relation to cap formation.

The seed is attached to the air cooled seed rod to create a thermal gradient and to provide the mechanical means for rotation and pulling. When the seed is touched to the melt which is held a few degrees above its liquidus temperature, melting or crystallization will take place depending upon the melt temperature and the amount of cooling applied to the seed. Figure 6 schematically shows what will happen to the seed under different conditions at a fixed level of seed cooling. The rate at which growth or melting occurs is a function difference between the actual melt temperature and a target temperature at which no changes in the seed will take place. If the

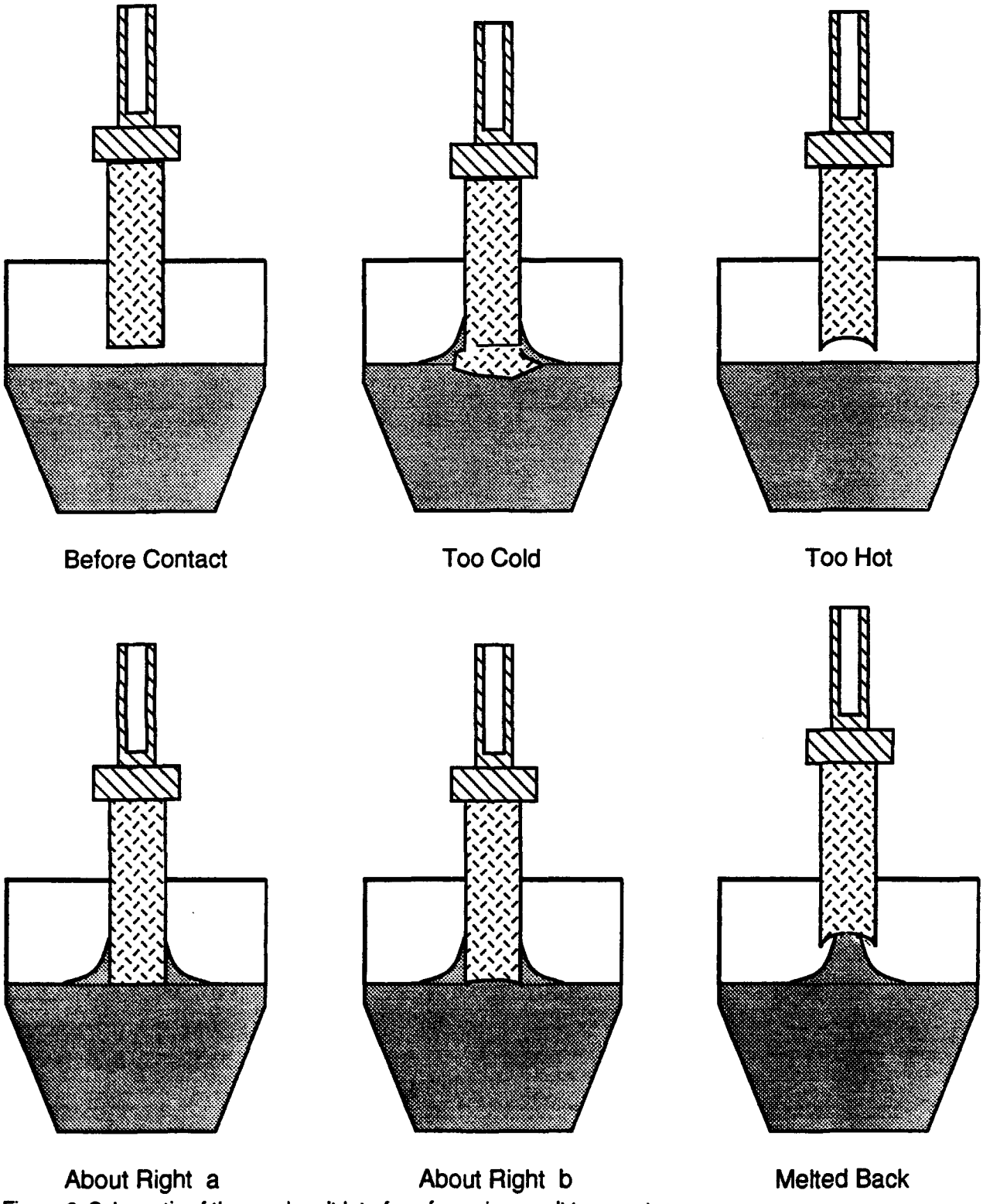

Figure 6. Schematic of the seed-melt Interface for various melt temperatures.

temperature difference is on the order of a few degrees, it can take several hours after a contact with the melt is made for the seed to finish melting or growing. In the steady state and neglecting supercooling, the liquidus isotherm is found at the liquid solid boundary. Similarly, if a steady state exists, response to a step change of one degree can take an hour or more.

The first frame in Figure 6 shows a seed ready to be touched to the melt. Contacting a melt that is too cold, second frame, leads to uncontrolled and often rapid growth of a large mass of material that may not be commensurate with the seed, while touching a melt that is too hot results in melting of the seed until contact with the melt is lost. Ideal seeding is shown in the frame labeled meltback. Here a small column of liquid is supported by surface tension. The purpose of achieving this condition is to ensure that stress, random growth and other defects caused by contacting the melt at too low a temperature have been melted away and therefore will not propagate into the crystal. Seeding in the about right range can also yield good quality crystals.

Two methods of reaching the meltback condition, the dipping and the visual will be discussed below. Following seeding, a crystal growth regime of temperature lowering and pulling is begun.

3.3.4.1 Dipping Method

The dipping method is the one that has been used in this laboratory for TSS crystal growth. As the seed is lowered to the melt, the position of contact is noted. After a period of time which ranges from 10 minutes to 1 hour, the seed is disconnected and reconnected. Whether the seed has melted or grown is reflected in the new measure of the contact position. An appropriate temperature adjustment is made and a new disconnect/connect cycle is begun. This is repeated until the contact position shows that some of the seed has been melted away and that the melting rate is low. A matter of judgement comes into play here in knowing when the seed will continue to melt and whether it will melt off or whether the temperature lowering of the growth regime will compensate for the melting.

Manual measurement of the seed position from a scale attached to the pulling guide is reproducible to ±.3 mm. Using computer controlled stepper motors the measured contact position is reproducible to ± 0.1 mm. Contact is determined visually by observing a reflection of the viewing lamp from the meniscus at the edge of the seed. Being able to observe the seed and melt surface is not a requirement of the dipping method. The resistance of the circuit between the crucible and the Pt seed rod measured with an ohm meter also serves as a reliable indicator of contact.

3.3.4.2 Visual Method

There has been some suspicion that the dipping method does not always lead to the optimum seeding conditions. If a visual indication of the states shown in Figure 6 can be obtained then it is possible to reach the correct seeding condition by varying the temperature without the disturbance of disconnecting and reconnecting the seed. In fact, a visual process is used in the seeding of fluoride crystals where all of the details shown in Figure 6 can be seen. The seed and surrounding melt can be seen through the furnace sight port but due to the small thermal gradients and the general background radiation, visibility is poor and illumination through the other port provides only a small enhancement of observable details.

In the visual method developed during this work for determining the correct meltback temperature, the amount of material melted or grown on the seed is judged from the radial position, relative to that at the time of contact, of the reflection of the viewing light from the meniscus and its locus as the seed is rotated. The reflection describes a path that is correlated with the shape of the solid intersecting the melt surface. The seed cross section is typically square and new growth formed in the too cold condition is often irregular.In the meltback condition, a column of liquid supported by surface tension intervenes between the seed and the melt surface and the cross section becomes circular. In the about right view, the tip and corners of the seed may be partially melted and the locus of the reflection is intermediate between square and circular.

To facilitate visual observation of the seed and the reflections from the meniscus a TV camera and monitor was used. The average radial position of the reflection as well as the locus of reflection was easily seen and could be marked on the screen for reference.

Typically the seed is contacted to the melt at a temperature as close to correct as possible. If temperature adjustments are required during the visual seeding method, they are made by a continuous ramp varying from 2 to 0.5 C/hr until the desired amount of meltback is obtained. At higher rates, considerable overshoot occurs, which means that if the ramp is stopped, melting or dissolving of the seed continues for several hours. Within a few degrees of the temperature for meltback, the ramp can not exceed 0.5C/hr.

3.3.5 Observations on Cap Formation

Barium titanate crystals are characterized by the so called cap. This is the topmost portion of the crystal that is cracked and contains numerous inclusions and voids. The cap typically starts just below the seed at the point where the boule begins to expand and terminates roughly at the point where expansion is finished. A cross section of the crystal cut just below the seed and perpendicular to the growth direction shows a border of continuous $BaTiO_3$ phase and a central section of polycrystalline material. Other similar pockets of polycrystalline material are found throughout the cap. Voids and elongated traces of inclusions are also found. The X-ray powder diffraction pattern of the inclusion material shows mainly tetragonal $BaTiO_3$ along with a phase tentatively identified as hexagonal $BaTiO_3$ and reflections from unidentified phases which may have formed when trapped liquid solidified.

Formation of the cap is related to melt composition, seed rod cooling, expansion of the crystal diameter and to the morphology of the crystal. These correlations are qualitative and warrant further investigation.

Because $BaTiO_3$ is grown from solution, the melt composition becomes richer in TiO_2 as the mass of the crystal increases. In observing the formation and termination of the cap, it appeared to be correlated with the TiO_2 content of the melt. From the mass of the melt and the mass of $BaTiO_3$ crystallized over the cap region, the melt composition at which the cap terminates can be estimated. Several crystals were grown from melts with starting compositions enriched in TiO_2 to the composition and beyond where this model indicates cap formation should not occur. Formation of the cap was observed in all crystals in this set indicating that melt composition is not the sole factor in cap formation. The role of composition, however, can not be excluded. Crystal growth started in melts leaner than 66mol% TiO_2 is disrupted by formation of other phases. For example, a large crystal of hexagonal $BaTiO_3$ was obtained in one run using a melt accidently prepared with too little TiO_2.

Seed rod cooling is measured by the flow of air into the seed rod rotation gland. In earlier work in this laboratory it was established that a low air flow on the order of 3 to 4 l/min reduced the tendency toward cap formation and generally promoted better crystal growth than obtained with higher air flow rates. The low air flow decreases the thermal gradient along the seed, making the seed melt contact less stable in the sense that the acceptable and melt back conditions in Figure 6 exist over a narrower furnace temperature range. During earlier parts of this work, while investigating seeding techniques, the air flow was increased for improved contact stability. In a series of runs over which the air flow was systematically reduced, the cap appeared to become less prominent. A run carried out in the new round Zircar furnace using a 66 mol% TiO_2

melt was done with only ambient cooling. Yet a cap developed that extended over the range of crystal expansion showing that seed cooling is not simply related to cap formation.

The effect of careful seeding, expansion and growth are epitomized by the results of growth run in which seeding was done by the visual method followed by a period of slow temperature lowering and pulling to grow neck of the same diameter as the seed. The boule was then gradually expanded to the final diameter. The join between the seed and the neck had no visible defects. The neck itself was grown to a length of ~8mm and remained free of the defects associated with cap formation as long as the diameter was constant. At the point where expansion of the boule started, cap defects were formed. These continued until expansion was terminated and the boule reached its final diameter.

The fourth factor that appears to be important in cap formation is the morphology of the crystal and how it evolves during the growth. Belruss et. al. (3) show the typical morphology of the finished crystal with its reentrant angles and {210} facets. Earlier work in which crystals were disconnected from the melt shortly after the start of the growth showed that the morphology had evolved from either a cube or octahedron to that of the finished form. In this work, we have also seen that the final morphology can depend upon the relationship between the pulling and temperature lowering rates and the rate at which the crystal is allowed to expand during the initial stages of the growth. In one run the relationship among these factors was such that the {111} form persisted throughout the growth yielding a crystal with no reentrant angles to trap melt. This crystal did not have the usual cap. Formation of the cap is related to this change in morphology during expansion of the crystal and to the trapping of liquid in reentrant angles on the faceted melt-solid interface.

There is insufficient data to properly account for the cap formation, although it appears that thermal gradients, morphology of the melt crystal interface and mass transport in the melt play a primary role, while bulk melt composition is of secondary importance unless the TiO_2 content is less than 66 mol%.

3.4 $BaO\text{-}B_2O_3\text{-}TiO_2$ System

In order to widen the scope of $BaTiO_3$ growth, another system was sought which, compared to the $BaO\text{-}TiO_2$ system, would allow crystallization under different chemical conditions at a lower temperature and over a wider range of Ba to Ti ratio.

Goto and Cross (4) found that the cut $BaTiO_3$ - BaB_2O_4 in the ternary system $BaO\text{-}B_2O_3\text{-}TiO_2$ forms a simple binary system with no solid solution formation and one

eutectic occurring at 32 mol% $BaTiO_3$ and 942C. The primary phase field for $BaTiO_3$, therefore extends from 100 mol% to the eutectic composition. The three binary end members, BaO-TiO_2 (1),(8) BaO-B_2O_3 (5) and B_2O_3-TiO_2 (8) have also been studied. A ternary compound, $BaTi(BO_3)_3$ (7) has been reported but its stability range is not known. Nothing else is known about the interior of the ternary system.

It has been suggested that Ba vacancies play a role in the appearance of the photorefractive effect in $BaTiO_3$. There was, therefore, interest in studying the relation between this phenomenon and the defect structure of $BaTiO_3$. In the BaO - TiO_2 system the ratio of Ba to Ti over which $BaTiO_3$ is grown is restricted to the range 0.52 to 0.48, while in the BaB_2O_4 - $BaTiO_3$ system the ratio is >1. Further, if we consider the entire BaO - B_2O_3 - TiO_2 system, then we may speculate that $BaTiO_3$ can be crystallized over a wide range of Ba to Ti ratios. The beginnings of a proposed phase diagram for this system is shown in Figure 7. The shaded region represents a roughly estimated primary phase field for $BaTiO_3$. The join between stoichiometric $BaTiO_3$ and B_2O_3 represents a Ba to Ti ratio of unity. The cross lines are compositions within the $BaTiO_3$ field along which the Ba to Ti ratio varies from >1 to <1 while the B_2O_3 fraction remains constant. Liquidus temperatures will rise with decreasing B_2O_3 fraction. Thus, $BaTiO_3$ with roughly the same impurity content (roughly because while the impurity content will be a function of the impurities present in the raw feed, the distribution coefficients will vary somewhat with the melt temperature and composition) can be crystallized over a wide range of Ba to Ti ratios.

The mass of $BaTiO_3$ that may be crystallized from some borate melt compositions is greater than can be obtained from a BaO-TiO_2 containing a similar amount of $BaTiO_3$. A BaO -TiO_2 melt containing 1 mol of $BaTiO_3$ can yield a maximum of 38g of $BaTiO_3$ crystal, while in the BaB_2O_4 - $BaTiO_3$ system a melt at the 0.5 mol fraction mark containing 1 mol of $BaTiO_3$ will yield 83g of crystal. Yields from other compositions in the ternary system can not be predicted because compositions of the relevant phase boundaries are not known.

3.4.1 DTA

The preliminary diagram of the BaO-B_2O_3-TiO_2 ternary system was constructed from the known points and some estimated extensions of the binary eutectic compositions into the interior of the three component system The subsystems were assumed to be of the simple eutectic type and were used to estimate the extent of the $BaTiO_3$ field. Although crystals can be grown without the benefit of a phase diagram, knowledge of the phase relations in a system can assist in the selection of

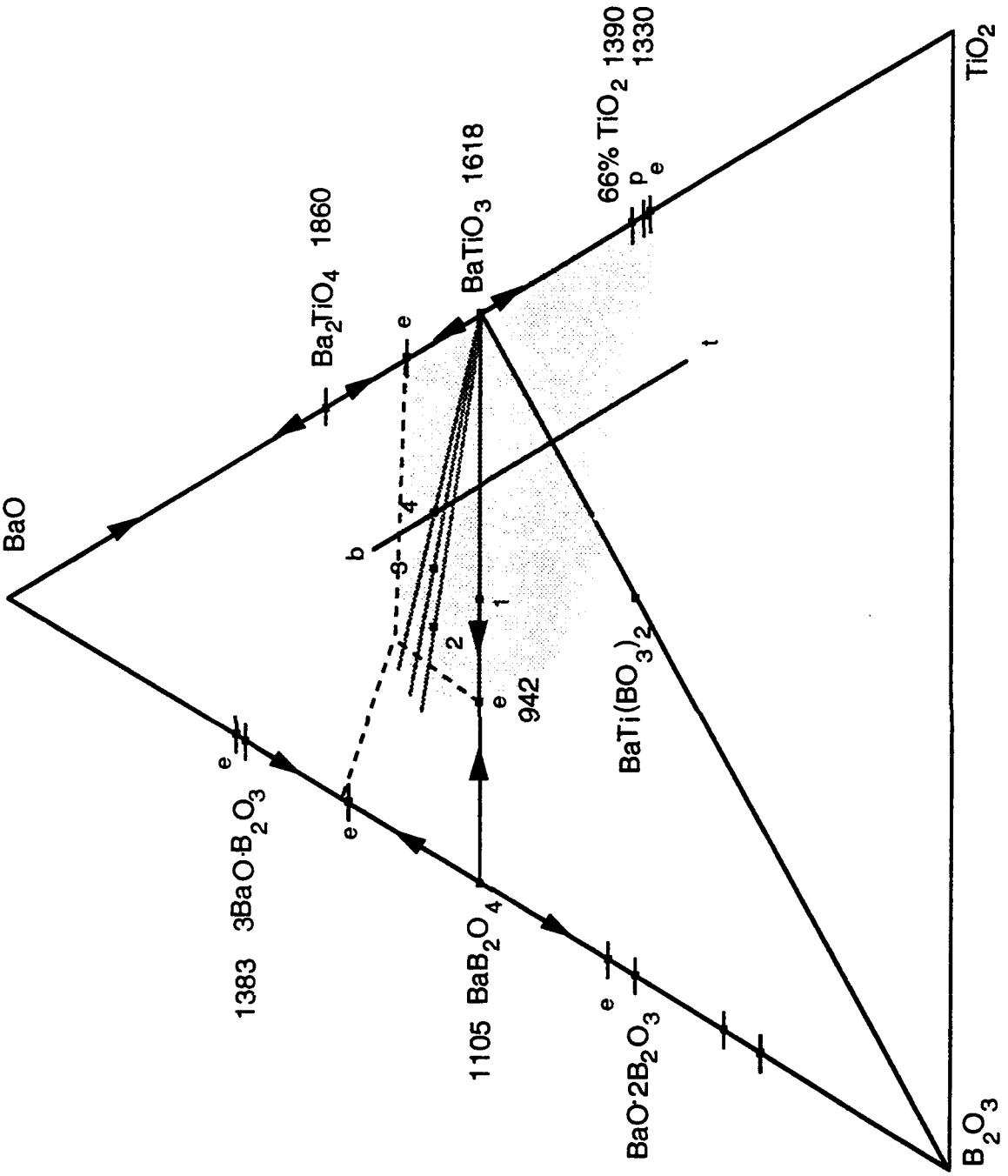

Figure 7. Phase relations in the BaO-B_2O_3-TiO_2 system.

experimental conditions such as composition, soak and seeding temperatures and can assist in understanding the crystallization path the formation of solid solutions and other phases and the mass of the crystal formed.

A detailed elaboration of the BaO-B_2O_3-TiO_2 system was beyond the scope of this work, However, to support crystal growth experiments in this system and to add additional data to the proposed phase diagram, DTA (differential thermal analysis) measurements were done to define liquidus temperatures, the general shape of the liquidus surface and the temperature range of the crystallization path for compositions of interest to crystal growth. Powder x-ray diffraction patterns of the material remaining in the DTA cup after a measurement gave an indication of the adjoining phase field intersected by the crystallization path. Figure 8 shows a typical thermogram. Three exothermic transitions on the cooling curve have been tentatively identified. Transition temperatures plotted as a function of composition are shown in Figure 9. The liquidus which varies with composition, occurs at the highest temperature; a second transition which is also composition dependent may be a two phase boundary and a third which occurs at a constant temperature independent of composition is probably a eutectic. The liquidus transition observed in the cooling curve in Figure 8 at 1423C is weakly defined and only became unambiguous when thermograms for a given composition were repeated using a fresh sample with the heating cycle taken to successively higher temperatures during each repetition. Visual observation of the sample during a DTA run and agreement with crystallization temperatures obtained in crystal growth experiments confirmed the assignment of the liquidus transition.

The series of compositions investigated on a 55 mol% BaO line are shown as points 2, 3 and 4 in Figure 7. The observed liquidus temperatures fell on a curve of the same general shape as the 50 mol% BaO line (the BaB_2O_4 - $BaTiO_3$ system) but displaced to higher temperatures. After a thermogram was measured, the contents of the Pt DTA sample cup were inspected under the microscope. The largest crystals identified as $BaTiO_3$ by powder x-ray diffraction were taken to be the primary phase. The other abundant phase was BaB_2O_4. The temperature of the two phase boundary was obtained from the thermograms, but determination of the composition of the boundary requires additional measurements. Nevertheless, the preliminary measurements begin to define the phase diagram.

A DuPont 2000 system with 1600 cell DTA apparatus was used for measurement of thermograms. Samples were prepared by grinding together weighed amounts of TiO_2, $BaCO_3$ and B_2O_3, sintering in a Pt crucible at ~900C for 1 to 2 hours followed by regrinding. A 40 mg sample was measured against an alumina reference.

Fig 8

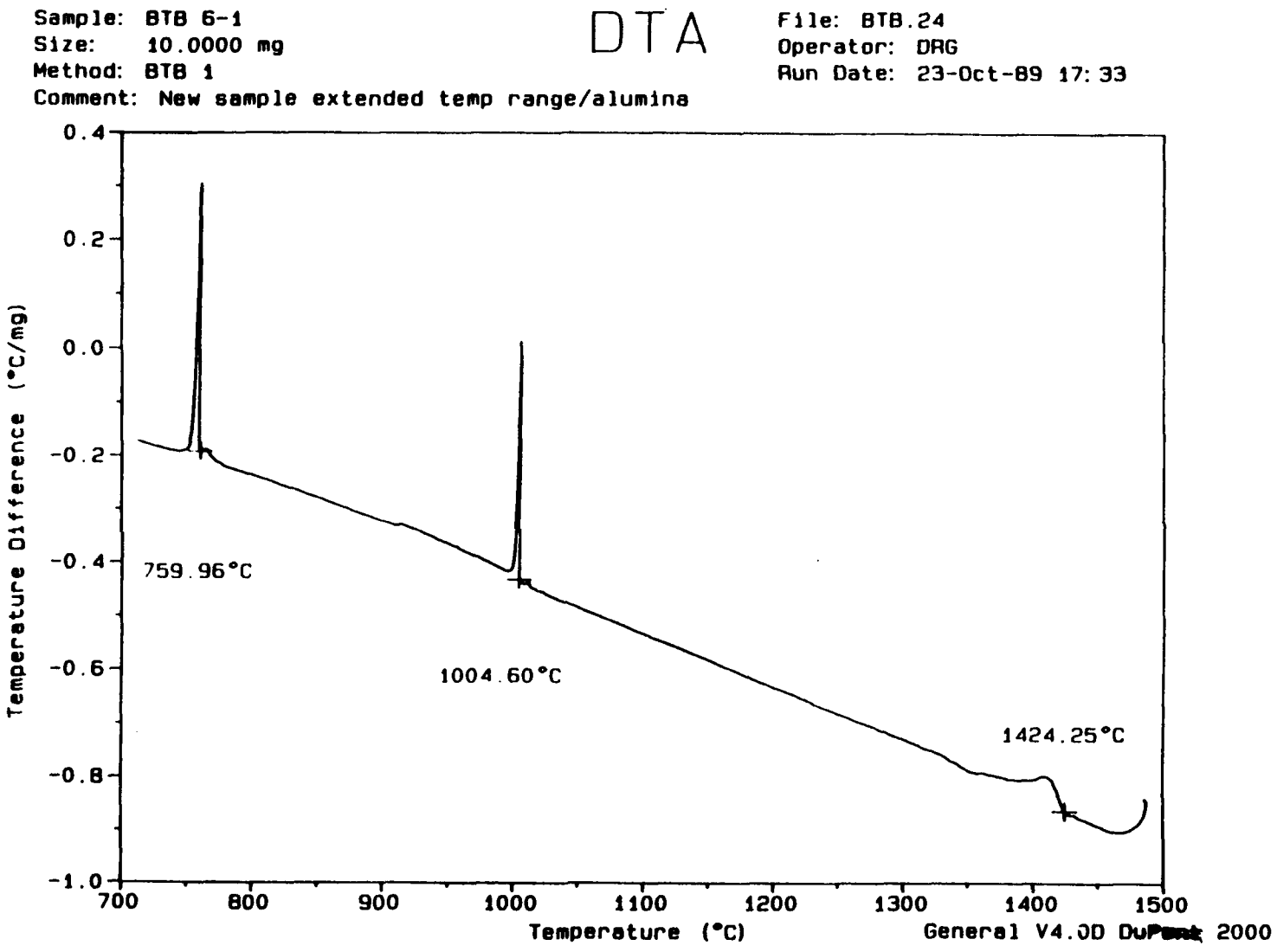
Sample: BTB 6-1
Size: 10.0000 mg
Method: BTB 1
Comment: New sample extended temp range/alumina
DTA
File: BTB.24
Operator: DRG
Run Date: 23-Oct-89 17:33
Temperature Difference (°C/mg)
0.4
0.2
0.0
-0.2
-0.4
-0.6
-0.8
-1.0
759.96°C
1004.60°C
1424.25°C
700
800
900
1000
1100
1200
1300
1400
1500
Temperature (°C)
General V4.0D DuPont 2000

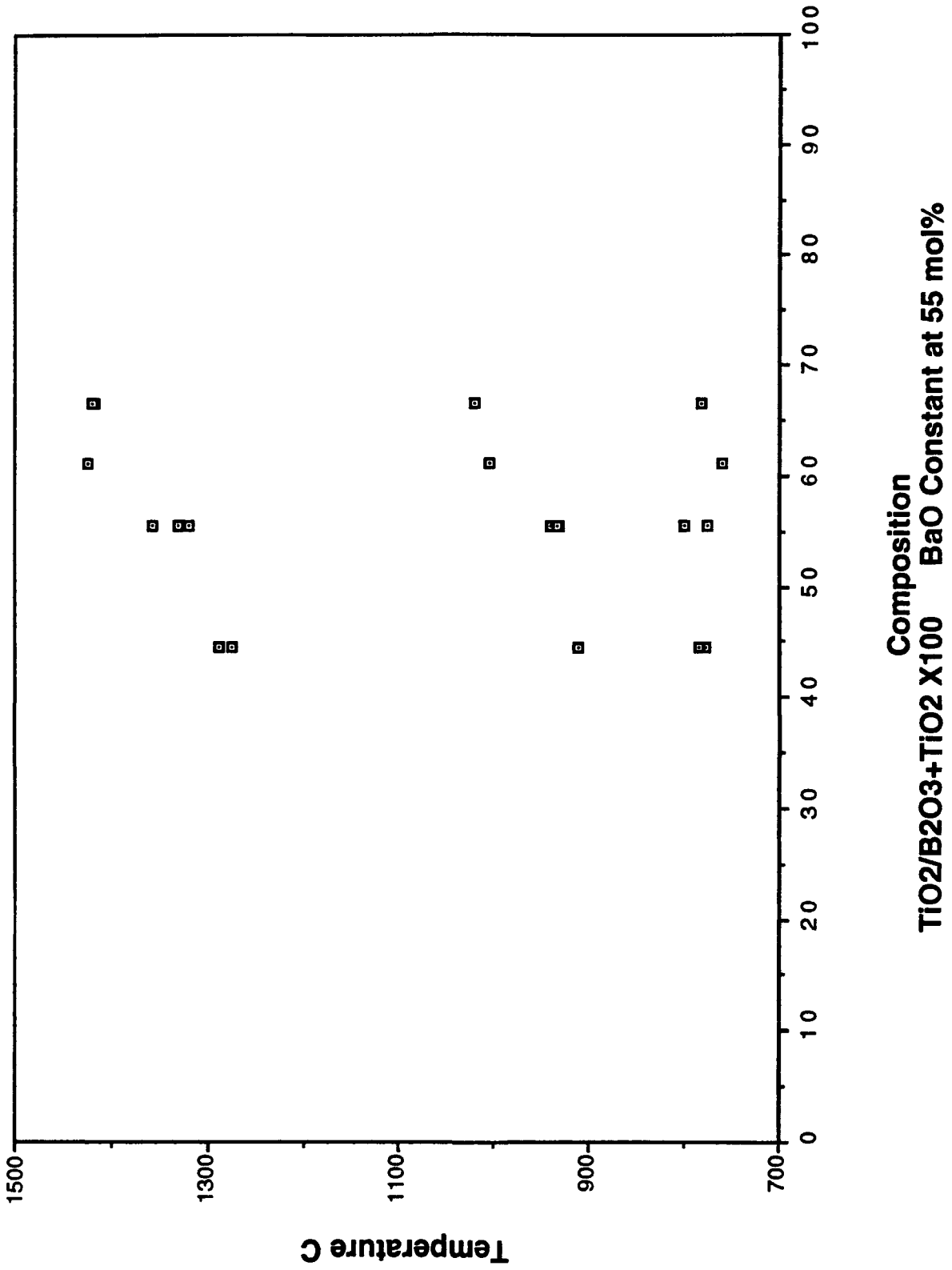

Figure 9. Transition temperatures as a function of the sample composition. in the BaO-B2O3-TiO2 system.

Seamless Pt cups obtained from Perkin Elmer Corp. were used. Samples were heated from ~ 700C to 1400 or 1500C at 10C/min and cooled to 700C at 10C/min. Sufficient time for subsolidus equilibration was not allowed and heating curves did not yield interpretable information. A quartz window placed on the top of the alumina furnace liner, instead of the cap supplied by DuPont, allowed sintering and melting phenomena to be observed.

Cooling curves showed a small high temperature exotherm taken to be the liquidus temperature and two larger exotherms taken to be a two phase boundary and eutectic respectively. With additional study, these assignments may be revised. The observed liquidus temperature depends upon the maximum temperature to which the specimen was heated.

3.4.2 Crystal Growth

Crystal growth runs in the BaO-TiO_2-B_2O_3 system are listed in Table 2. Compositions are also shown on the phase diagram shown in Figure 7. Melts were prepared by heating a mixture of BaO, B_2O_3 and TiO_2 to 50C above the melting point followed by stirring overnight with a spiral shaped Pt sheet. Single crystal {100} $BaTiO_3$ seeds were used. The ceramic seed rod was used except in some of the early runs. Seeding was carried out by the dipping method. Typical growth parameters were: temperature lowering between 0.25 and 1C/hr, pulling 0.05 to 0.1 mm/hr, rotation rate 20 rpm, air cooling to the seed rod, 0 to ~6 l/m. All runs in this phase of the work were carried out in the cylindrical Zircar furnaces.

Table 2. Crystal Growth from Barium Borate Flux.

Run	BaO	TiO_2	B_2O_3	BaF_2	Comments
24Z	0.50	0.25	0.25	-	Block structure ,layers ,suggesting constitutional supercooling
27Z	0.50	0.25	0.25	-	Sets of overgrown cubes
29Z-A	0.55	0.30	0.15	-	Temp too high for furnace. Small cubes in frozen melt
29Z-B	0.55	0.25	0.20	-	Dendritic Growth
29Z-C	0.55	0.20	0.25	-	{110} layered growth.
32Z	0.55	0.20	0.25	-	Effect of crucible position. Surface nucleation observed.
35Z	0.55	0.20	0.25	-	Effect of crucible position. Surface nucleation observed.
36Z	0.55	0.20	0.25	-	Effect of crucible position. layered growth obtained.
37Z	0.50	0.20	0.25	0.05	Layered growth obtained. Dark blue-green crystal.

The first crystal growth experiments (24z and 27z) were carried out from a 50% BaB_2O_4 - 50% $BaTiO_3$ melt marked 1 on the binary join in Figure 7. The results were essentially the same as obtained from a similar run carried out earlier in the brick furnace. Single phase $BaTiO_3$ was obtained and the temperature at which crystal growth started was in rough agreement with the published liquidus temperature (5). Physically, the crystals obtained consisted of numerous square or rectangular blocks and layers separated by boundaries of solidified liquid. The bottom surface of the crystal shows that for the most part the blocks are oriented, but some are clearly not indicating that nucleation of the misoriented blocks had occurred in the liquid in front of the crystal-melt interface through constitutional supercooling. This implies accumulation at the interface, as a result of poor mixing with the bulk of the melt, of a liquid layer containing an excess BaB_2O_4 relative to the concentration in the melt. A vertical cross section through the crystal and seed shows the individual blocks to be highly irregular, some increasing in volume in the direction of crystal growth and others decreasing or terminating within the crystal. The boundaries between the blocks are often a few tenths of a mm wide and filled with solidified liquid. The cellular structure and dendritic growth typical of constitutional supercooling is clearly visible at some of the internal boundaries.

Additional crystal growth runs, collectively labeled 29z, were carried out on the 55 mol% BaO line over a range of TiO_2 fractions. Melt compositions and comments on the results are listed in Table 2. DTA measurements were also made on these compositions. Liquidus temperatures measured by DTA and obtained from the crystal growth runs agreed to about 20C. The appearance of the material crystallized in the furnace was similar to that in corresponding DTA cup, for example, the dendritic growth observed in Run 29Z-B was also seen in the material crystallized in the DTA sample cup.

Nucleation on the melt surface was a limiting factor in many of the runs. In the worst case the independent floating crystals attached to the main seeded crystal and eventually grew over some larger portion of the melt surface. Thermal gradients at the melt surface are influenced by its position and are important factor in surface nucleation. Runs 32Z to 36Z were carried out from a melt of fixed composition order to evaluate the relationship between the vertical position of the crucible and spurious nucleation. In the highest crucible position used, spaced 3" from the bottom of the furnace, nucleation was not observed, while in the lowest position,the phenomenon was troublesome.

3.4.3 Addition of BaF_2

It was found in this laboratory that addition of BaF_2 to melts fluxed with BaB_2O_4 can reduce spurious nucleation by reducing the viscosity of the melt. A set of growth runs was carried out in the cylindrical furnace to test the furnace and to investigate the effect of added fluoride. Nucleation on the melt surface, multiple nucleation and block type growth were obtained. The addition of BaF_2 to the melts did not significantly alter the crystallization of $BaTiO_3$ from the borate fluxed melt and additionally caused the crystals to become very dark blue-green and, therefore, unsuited for optical purposes.

Run 37z was carried out to verify earlier results and to compare growth of $BaTiO_3$ with and without added fluoride under similar conditions.

3.4.4 Discussion

All of the crystals grown from the borate fluxed melts exhibited the same block structure and overgrowth layers. Although several large crystals were grown, after extensive cutting and polishing only mm size inclusion and crack free pieces could be found. The most likely cause of the interface instability which gives rise to constitutional supercooling and formation of overgrowth layers and inclusions is poor mass transport and compositional inhomogeneity at the crystal melt surface. High melt viscosity is the dominant parameter. The rate limiting step for crystal growth in this system is mass transport. In the absence of this limit, the rate of formation of solid phase is a function of the temperature lowering rate. In a real system, too high a temperature lowering rate leads to instability. In the case of the BaB_2O_4 - $BaTiO_3$ melts, temperature fluctuations due to controller noise exceeded the rate required for stable crystallization.

3.5 References

1. R. Rase and R. Roy, J. Am. Cerm. Soc. 38, 11 (1955)
2. J. P. Ramika, J. Am. Chem. Soc. 76, 940 (1954)
3. V. Belruss, J. Kalnajs, A. Linz and R. C. Folweiler, Mat. Res. Bull 6, 899 (1971)
4. Y. Goto and L. E. Cross,Yogyo Kyohai Shi 77, 355 (1969)
5. E. M. Levin and H, F. McMurdie, J. Res. NBS. 42,135 (1949)
6. H. M. O'Bryan and J. Thomson, J. Am. Cerm. Soc. 57, 522 (1974)
7. Nat. Bur. Stand.(U.S.) Monogr. 21 (1984)
8. T. Negas, R.S. Roth, H. S. Parker, and D. Minor, J. Solid State Chem., 9, 300 (1974)

4 Characterization of $BaTiO_3$: Ni

4 Characterization of $BaTiO_3$:Ni

4.1 Introduction

Barium titanate is a photorefractive crystal which has a large two beam coupling gain but slow response time. Until now there has been no conclusion about the origin of the photorefractive effect in barium titanate. To improve its performance, beam coupling gain and the speed, we have chosen to add impurities into the crystal.

In this project, the influence of Ni on the barium titanate was investigated. The Ni-doped crystals were grown and poled at the Sanders Associates. Samples include undoped, 10 ppm, 25 ppm and 50 ppm Ni-doped barium titanate, but the 25 ppm Ni-doped barium titanate has defects inside the crystal.

Here we report the characterization of the photorefractive properties of Ni-doped barium titanate, which include absorption spectroscopy, two beam-coupling gain, and light-induced grating erasure.

4.2 Absorption Spectroscopy

When light is incident on the crystal, the absorption coefficient α is defined by the equation

$$I_t = I_0 \exp(-\alpha d), \tag{1}$$

where I_t is the transmission beam intensity, I_0 is the incident beam intensity and d is the crystal thickness.

The optical absorption coefficient was measured using a Perkin-Elmer λ-9 spectrometer. The monochromatic light from the spectrometer is incident on the crystal and its transmitted beam intensity is measured by the photomultiplier at each 0.5 nm interval within the wavelength from 400 nm to 860 nm. The transmittance T is related to the absorption by the equation

$$T=\frac{I_t}{I_0}=\frac{(1-R)^2\exp(-\alpha d)}{1-R^2\exp(-2\alpha d)}. \quad (2)$$

If the product $\alpha d << 1$, then the transmittance equation can be rewritten as

$$\alpha d=\ln(\frac{I_0}{I_t})+2\ln(1-R), \quad (3)$$

where R is the normal reflectance with

$$R=\frac{(n-1)^2}{(n+1)^2}, \quad (4)$$

where n is refractive index. From the transmittance data the absorption coefficient can be calculated from the above equations. The results are shown in the Figures 1 and 2 with electrical field parallel and perpendicular to the c axis.

The undoped crystals appear clear. From the absorption spectra, the addition of Ni does not show significant absorption change in the visible range with the doping level of 50 ppm.

4.3 Two Beam Coupling Measurement

Two-beam coupling gain measurement was used for characterizing the photorefractive properties. From the dependence of two beam coupling with grating wavevector the effective trap density can be calculated. Carrier type can be determined from the gain direction relative to c axis. According to the photorefractive theory when the grating modulation index m created by two writing beams is small, the coupling gain γ_{eo} is the function of grating wavevector k_g as given by

$$\gamma_{eo}=A\frac{k_g}{k_g^{\,2}+k_0^{\,2}}, \quad (5)$$

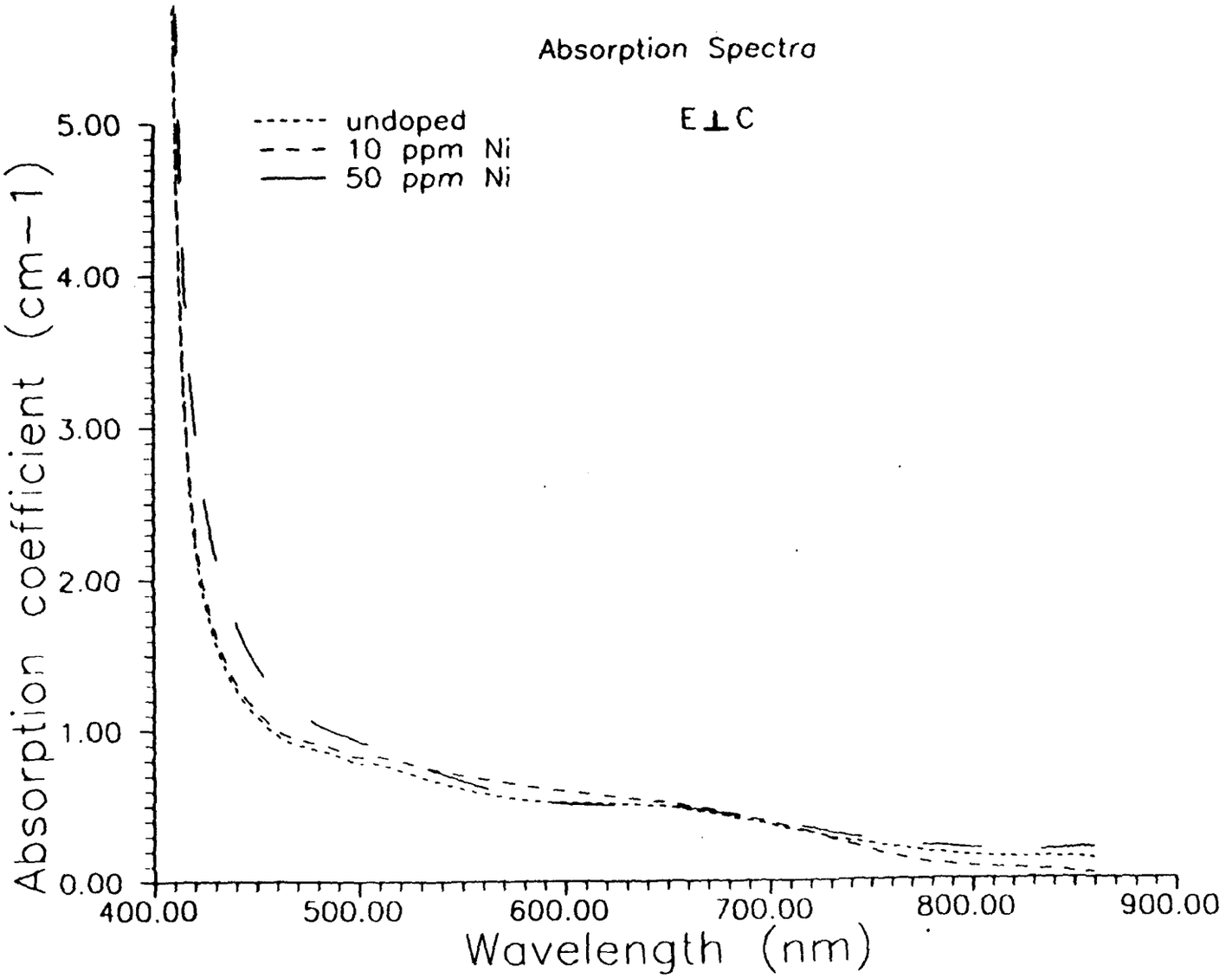
Absorption Spectra
E⊥C
undoped
10 ppm Ni
50 ppm Ni
Absorption coefficient (cm-1)
5.00
4.00
3.00
2.00
1.00
0.00
400.00
500.00
600.00
700.00
800.00
900.00
Wavelength (nm)

Fig. 1

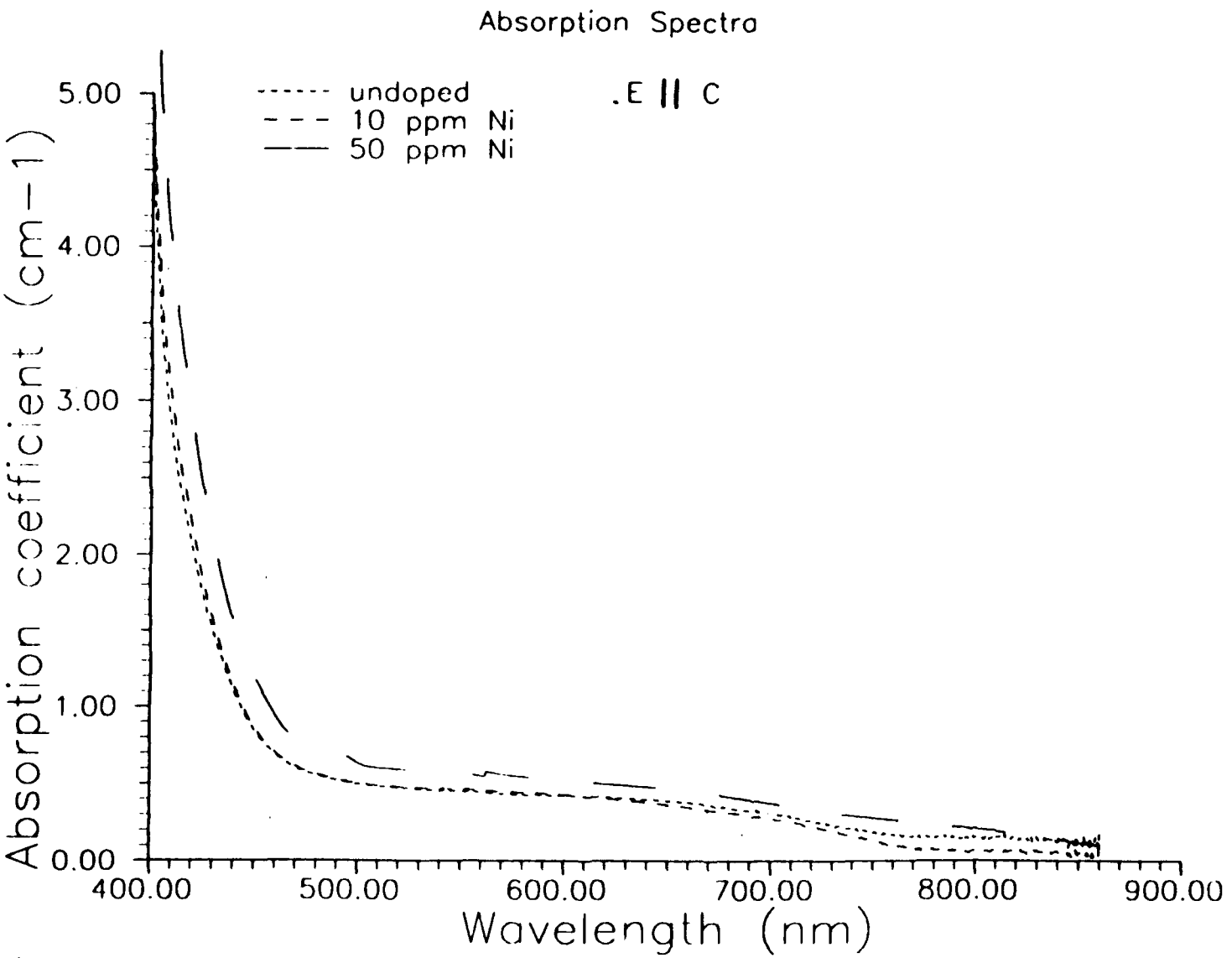
Absorption Spectra
undoped
10 ppm Ni
50 ppm Ni
.E || C
Absorption coefficient (cm-1)
5.00
4.00
3.00
2.00
1.00
0.00
400.00
500.00
600.00
700.00
800.00
900.00
Wavelength (nm)

Fig. 2

where A is a constant, and k_0 is the screening length which is proportional to the square root of the effective trap density N_T. So from this relation, the trap density can be determined by measuring the dependence of the coupling gain γ_{eo} with the grating wavevector k_g.

The experimental setup is shown in the Figure 3. The Argon laser beam was expanded and separated into two beams, signal beam and pump beam. The pump beam intensity was 22m W/cm^2, and the signal beam intensity was 0.22 mW/cm^2 to keep the modulation ratio m << 1. The crystal is at the standard configuration where the c axis is in the incident plane of two writing beams and parallel with the grating wavevector. The polarization of the light is set to be perpendicular to the incident plane to avoid the large fanning effect in the barium titanate. After turning on the pumping beam, the signal beam exponentially increases to the saturation state which is monitored by the AT&T personal computer. The gain is given by

$$\gamma_{eo} = \frac{1}{d} \ln\left(\frac{I_1}{I_{10}}\right), \tag{6}$$

where I_1 and I_{10} are the signal beam intensities with and without the pump beam, respectively, shining on the crystal at the steady state. The result is shown in the Figure 4. The fit between the coupling gain and the grating wavevector was made with the PC version of the commercial math package, Mathlab, and the effective trap density was obtained.

The majority carrier was found to be holes for all three crystals. The maximum measured gain for these Ni-doped barium titanate crystal was in the range of 2 - 3 cm^{-1}. The 10 ppm Ni-doped barium titanate has the highest gain, and the 50 ppm Ni-doped sample had the same gain as the undoped sample. The undoped sample had an effective trap density 1.96x10^{16} cm^{-3}, the 10 ppm Ni sample has 2.26x10^{16} cm^{-3} and the 50 ppm Ni sample has 2.0x10^{16} cm^{-3}.

4.4 Light-Induced Grating Erasure Measurement

Speed is another parameter for characterizing the photorefractive effect. Usually, it is measured via the erasure of the grating with light.

The setup is shown in the Figure 5. As in the case of the two-beam coupling measurement, the

Setup for Beam Coupling

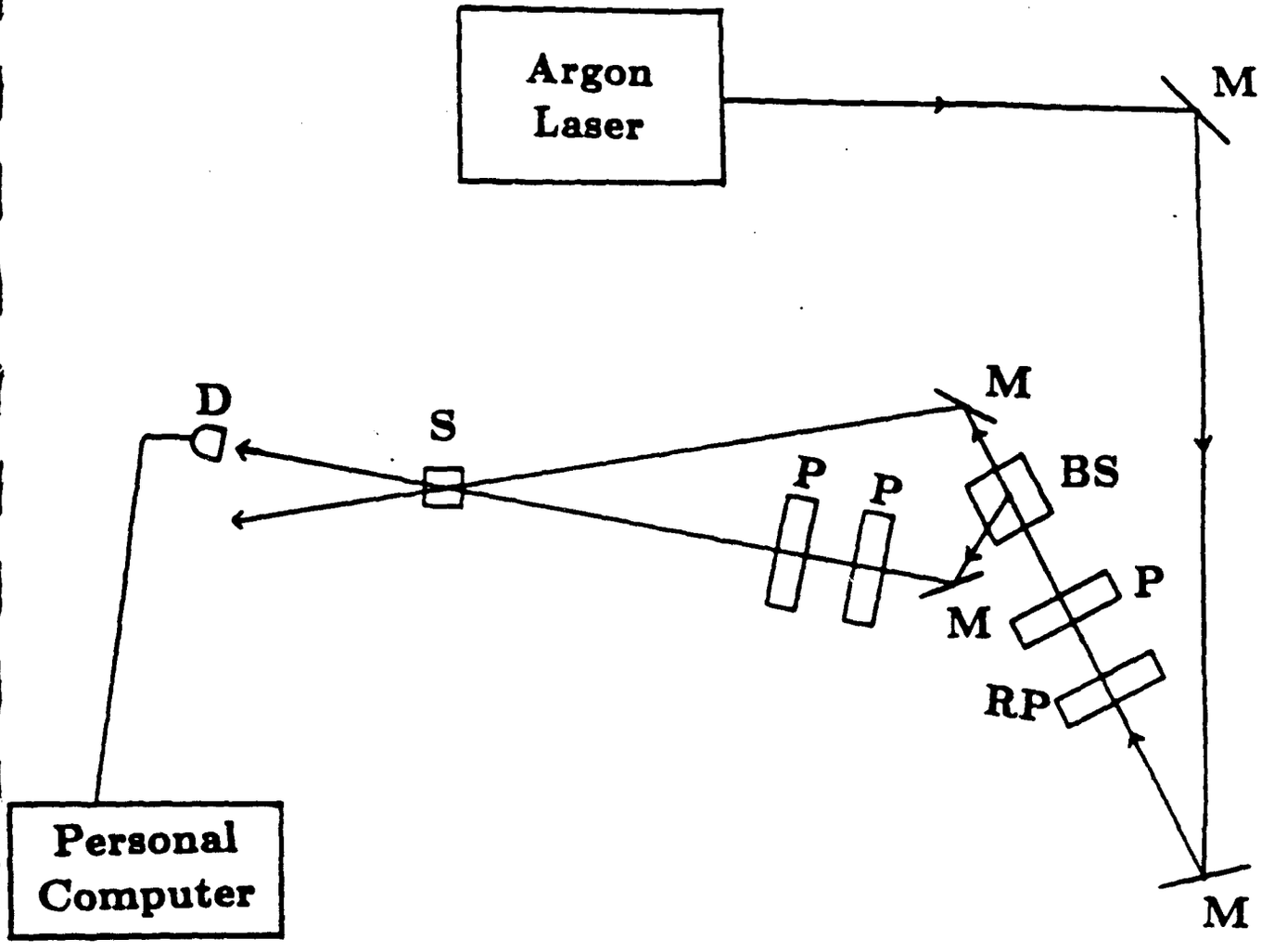

Fig. 3

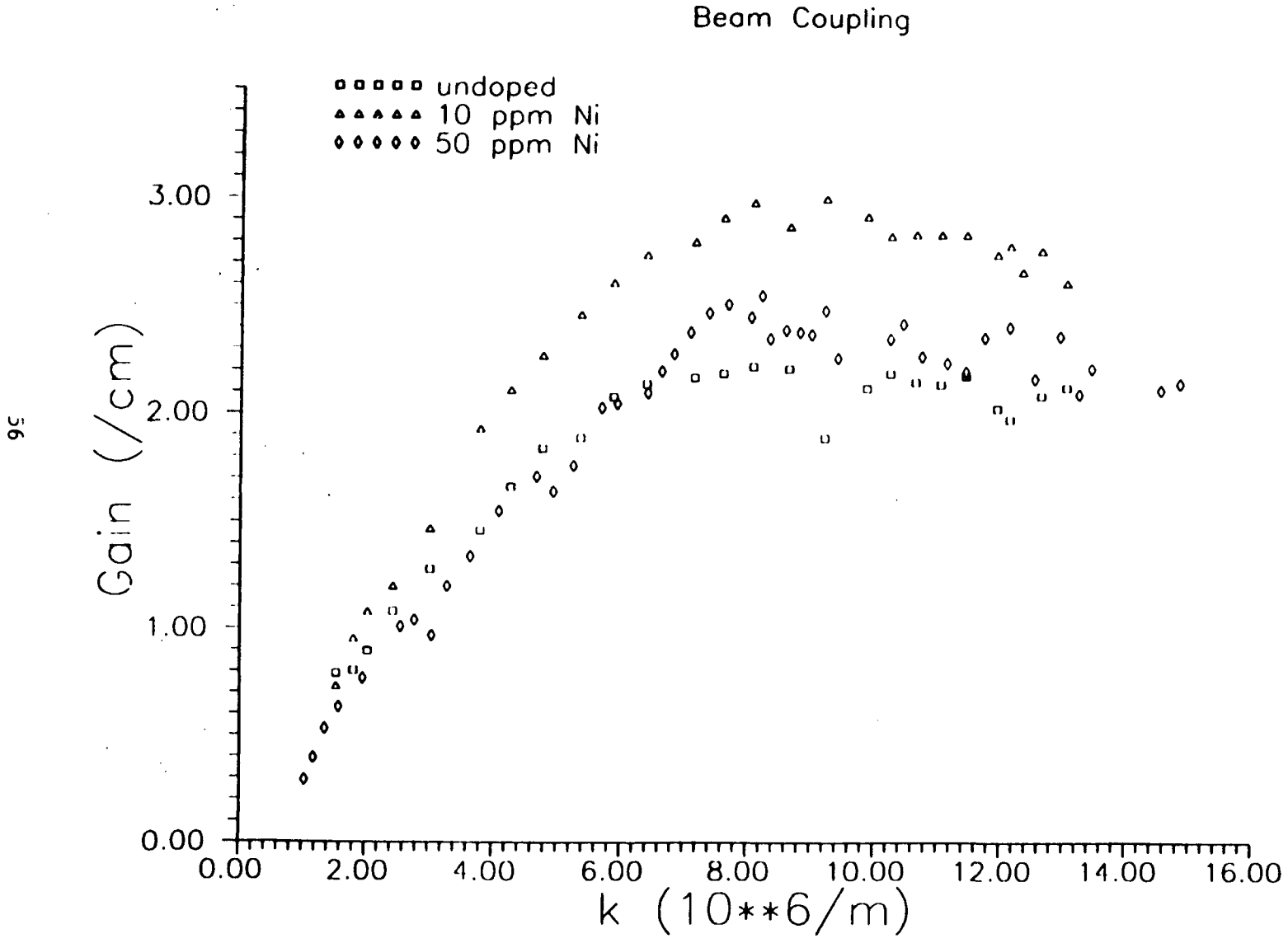
Beam Coupling
undoped
10 ppm Ni
50 ppm Ni
Gain (/cm)
3.00
2.00
1.00
0.00
0.00
2.00
4.00
6.00
8.00
10.00
12.00
14.00
16.00
k (10**6/m)

Fig. 4

Setup for Decay Rate

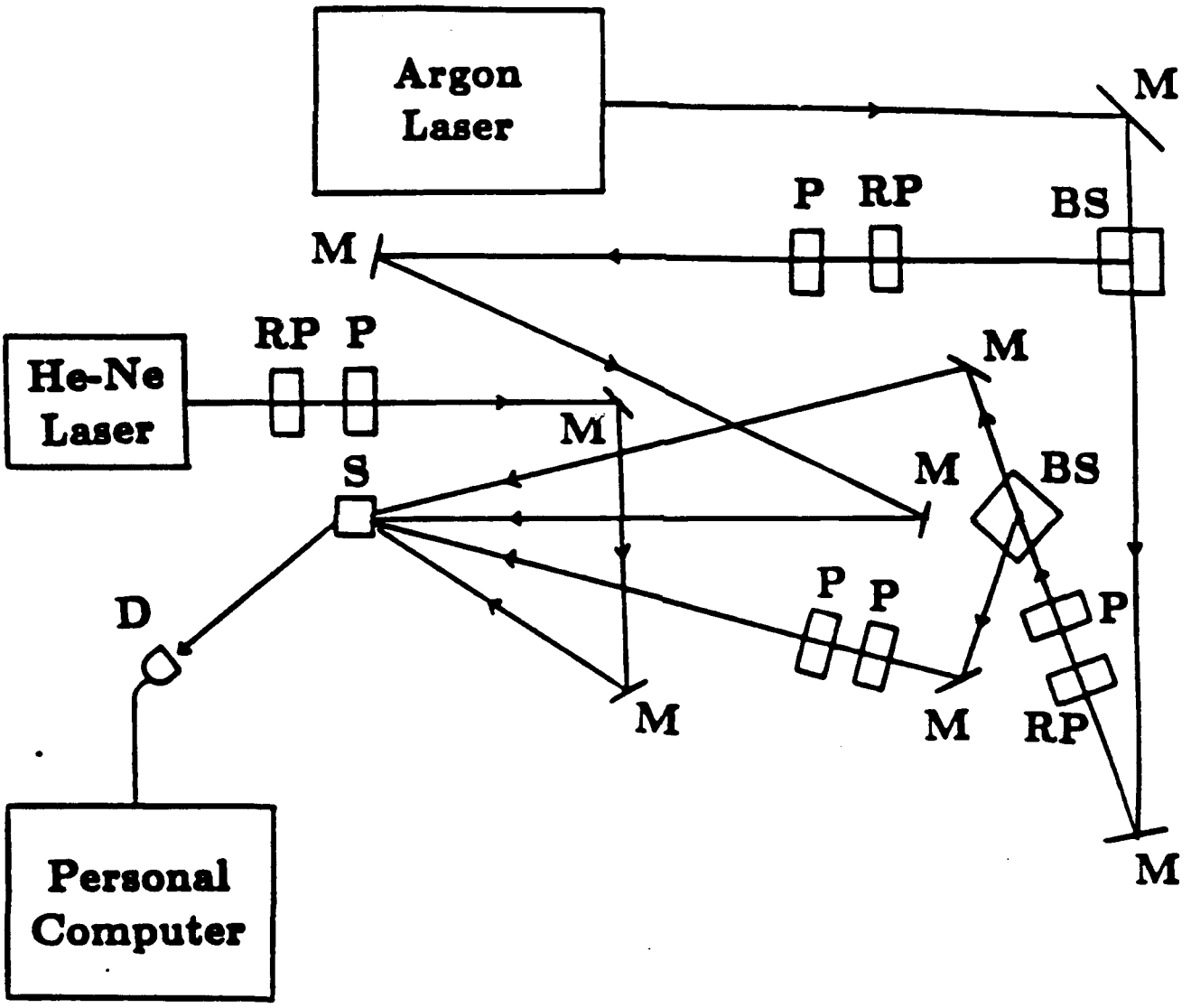

Fig. 5

grating was written by two writing beams from the argon laser. The space-charge field strength is monitored by the Bragg diffracted beam from a He-Ne laser. To avoid the interference with the grating, the readout beam intensity is about 1 $\mu W/cm^2$. After the grating reached the saturation level, the grating was erased with another uniform beam with intensity of 10 mW/cm^2 from the argon laser. The diffracted beam showed a single exponential decay (Figure 6).

From the results, the decay rate is around 0.01 to 0.1 sec^{-1}. The 10 ppm Ni-doped barium titanate has the highest decay rate, as compared with the undoped and 50 ppm Ni-doped samples.

4.5 Conclusions

Nickel was added as a dopant into barium titanate crystal to optimize the photorefractive properties (two beams coupling gain and response time). Absorption spectra, two-beam coupling and decay rate measurements were made for the undoped, 10 ppm and 50 ppm Ni-doped barium titanate. From the results, 10 ppm Ni-doped barium titanate has higher gain and speed than both the undoped and 50 ppm Ni-doped barium titanate. However, in the range of Ni concentration studied, we did not find a significant change of the photorefractive properties by adding Ni into barium titanate crystal.

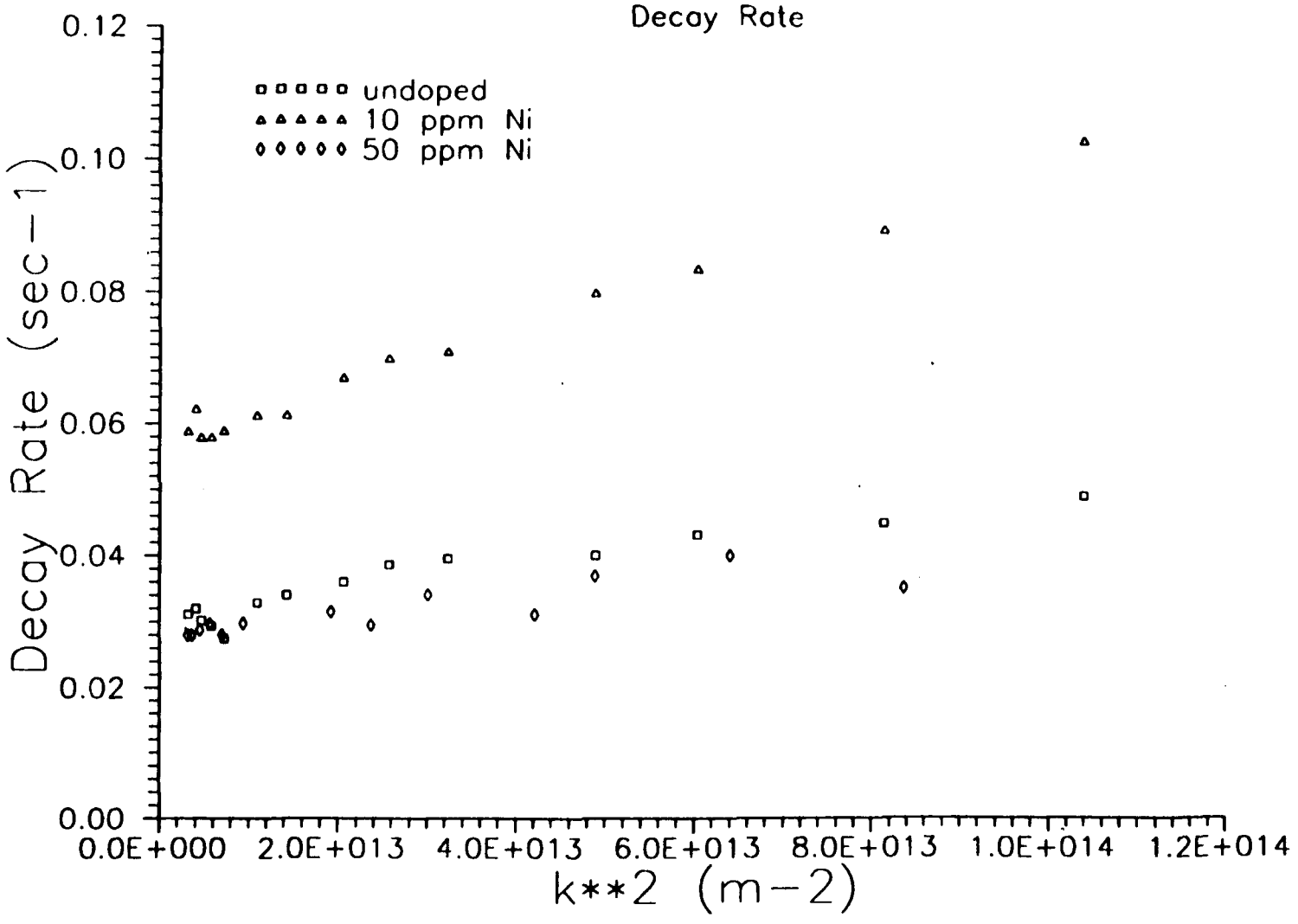
Decay Rate
undoped
10 ppm Ni
50 ppm Ni
Decay Rate (sec-1)
0.12
0.10
0.08
0.06
0.04
0.02
0.00
0.0E+000
2.0E+013
4.0E+013
6.0E+013
8.0E+013
1.0E+014
1.2E+014
k**2 (m-2)

Fig. 6

5 Intensity-Dependent Absorption in $BaTiO_3$:Fe

INTENSITY-INDEPENDENT ABSORPTION IN $BaTiO_3$:Fe

Iron-doped $BaTiO_3$ crystals were grown at MIT by the standard top-seeded solution growth technique. In addition to the increase in the absorption coefficient, the addition of iron to $BaTiO_3$ causes an increase in the intensity dependent part of absorption coefficient. This is an effect in which the measured absorption coefficient increases with increasing intensity. This behavior represents interesting physics, but is undesirable in practical application.

Intensity-dependent absorption in nominally pure $BaTiO_3$ was first reported by Motes and Kim[1] in 1987. They were studying an anomalous behavior, reported by Klein *et al*[2] which consisted of an observed change in the sign of the two beam-coupling gain at large grating spacings. The sign reversal was explained by Strohkendl *et al.*[3] and separately by Valley[4] as a competition between electrons and holes having different densities and diffusion lengths. Motes and Kim observed similar behavior when the crystal was oriented to cause the weak signal beam to increase. However, when the crystal was rotated 180 degrees which caused the weak signal beam to decrease, the sign reversal was not observed.

Asymmetric behavior of the coupling with regard to the direction of the c-axis is not predicted by any of the theories, but can be explained by assuming that the absorption increases when the pump beam is turned on. Indeed this behavior was observed by Motes *et al.* and used as an alternative theory to explain the anomalous behavior. Motes and Kim,[5] and Brost[6] attempted to measure the absorption coefficient as a function of pump intensity and correlate this with the intensity dependence of two beam-coupling. They measured the transmission of a weak probe beam and pumped with a much more intense beam. The two beams were made incoherent to eliminate beam-coupling. Unfortunately this experiment was performed using the usual two beam-coupling arrangement and the absorption of the pump beam was not taken into account. They observed that the absorption coefficient increased with intensity and then began to saturate. In their experiment, the saturation may be due to the absorption of the pump beam. Brost *et al.* attempted to fit their data to a three impurity level model with a large number of parameters.

Experimental Procedure

As mentioned above, the published methods of measuring the change in the absorption coefficient of $BaTiO_3$ as a function of power are flawed due to nonlinear absorption of the pumping beam. Since the actual absorption can not be obtained from the data without first assuming a functional form for the intensity dependence of the absorption, these measurements only verify the fact that an intensity dependence does exist. In view of these difficulties, an experimental arrangement was chosen such that the absorption of the pump intensity along the path of the probe beam is negligible. The probe beam intensity must also be low enough so that its affect on the absorption is negligible compared to the pump. The geometry which satisfies these criteria is one with the pump and probe beams perpendicular to each other. The probe beam must have a small diameter and

be very near the surface of the sample so the absorption of the pump can be neglected.

When these conditions are met, we can replace the absorption coefficient with

$$\alpha = \alpha_0 + \Delta\alpha(I_{pump}) \tag{1}$$

where α_0 is the low intensity absorption coefficient and $\Delta\alpha(I_{pump})$ is the change in the absorption coefficient due to the pump intensity. This form is very convenient because we can measure the change in α without the errors associated with measuring α. This is done by measuring the transmitted intensity without the pump beam and then making the same measurement with the pump beam. Since the sample is not moved during this experiment, it is possible to measure $\Delta\alpha$ without the calibration needed to measure the absolute value of α. The value of $\Delta\alpha$ is given by:

$$\Delta\alpha(I_{pump}) = \frac{1}{d} ln\left(\frac{I_{probe}(I_{pump} = 0)}{I_{probe}(I_{pump})}\right) \tag{2}$$

where d is the sample thickness in the probe direction.

Preliminary measurements of the intensity-dependent absorption were made with the apparatus illustrated in Fig. 1. The pump beam was from the 488 nm line of an Ar-ion laser, and it was expanded to approximately 1.0 cm. In order to avoid beam-coupling, the probe beam was from a second Ar-ion laser and data were taken at each of the wavelengths; 476.5, 488.0, 501.7, and 514.5 nm. This beam was apertured to 1.6 mm and entered the crystal very close to the face being pumped. In this way, the change in the pump intensity across the probe beam was minimized. The intensity of the probe beam was monitored as a function of time after each exposure to the pump beam. These rise curves were measured as a function of the pump intensity. From these data and the crystal thicknesses the variation in the absorption coefficient was obtained.

Although Motes *et al.*[1] reported that the observed change in the optical absorption of nominally undoped $BaTiO_3$ decreased with increasing temperature, this does not insure that the apparent intensity-dependent absortion is not a thermal effect. It might be some form of defocusing of the beam due to thermal gradients in the crystal. In order to insure that the decrease in the transmitted light intensity was not due to heating by the pump beam, the change in the transmitted intensity and the crystal temperature (via the pyroelectric effect) were monitored simultaneously.

The experiment shown in Figure 1 was modified by coating the c-faces of the sample with liquid In-Ga electrodes leaving a small area near an a-face uncoated to allow the probe beam to pass through the sample. Silver paint was also used for the electrodes and found to give unreliable results. The electrodes were attached to a transimpedance amplifier, and the output of the amplifier was recorded by the computer simultaneously with the intensity measurement from the photodetector.

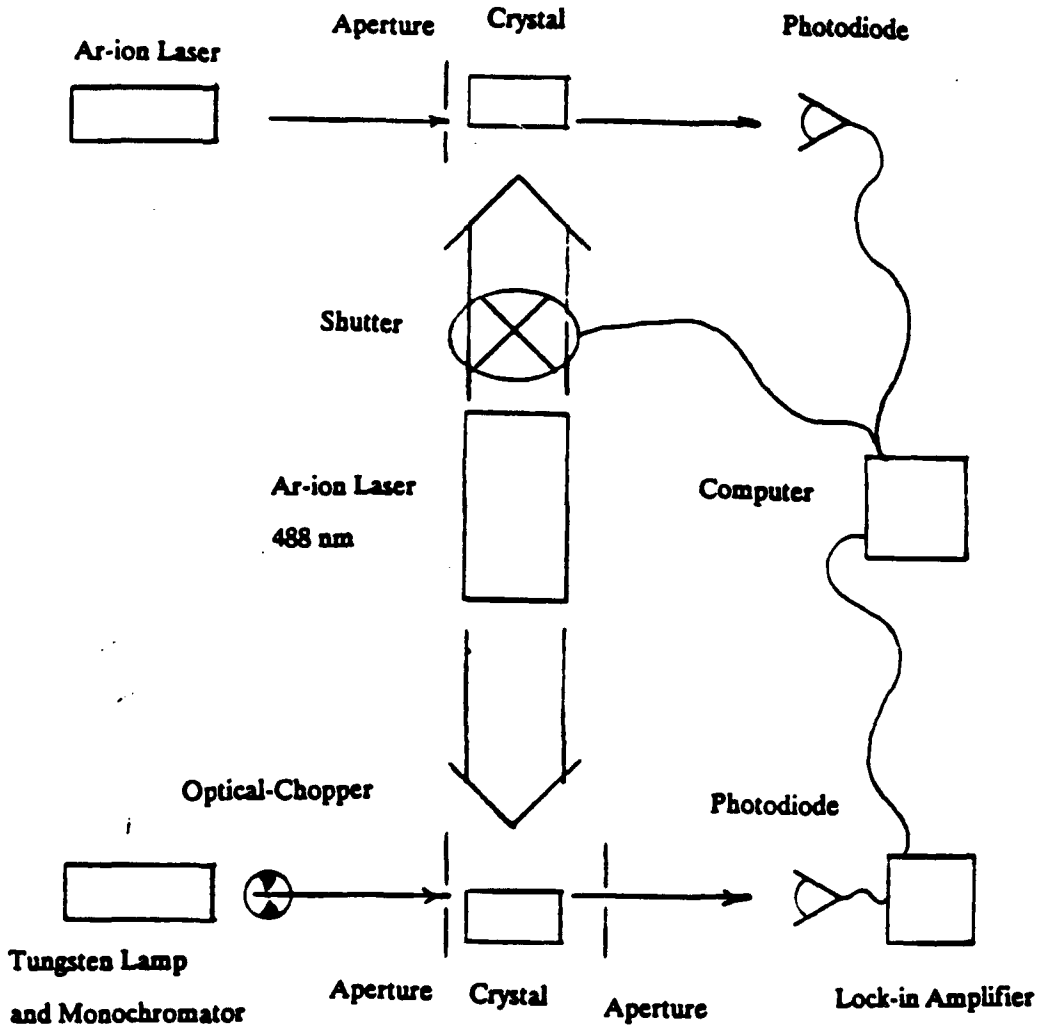

Fig. 1. Apparatus used to measure intensity-dependent absorption. The probe beam could be generated by a laser or a lamp and monochromator.

Figure 2 shows the decay of the intensity and the rise in the pyroelectric current. The change in temperature is given by

$$\frac{dT}{dt} = \frac{i}{A\,p} \tag{3}$$

where i is the measured current, A is the area of the crystal and p is the pyroelectric coefficient. Thus the change in temperature is given by the integration of Eq. 3 which was done numerically and the results are shown in Figure 3. The temperature changes exponentially with time with a time constant of approximately 27 seconds which is much longer than time constant, 0.07 seconds, of the intensity-dependent absorption measured simultaneously. Based upon the results of the above experiment and the literature[1] the intensity-dependent absorption is not due to a change in temperature of the crystal when illuminated by the pump laser.

Another possible explanation of the decrease in the transmitted intensity is scattering from photorefractive gratings. It is well known that scattered light from a coherent beam will cause noise gratings which are responsible for beam fanning. These noise gratings could also cause scattering of an incoherent light beam and result in a decrease in the transmitted intensity as observed. However, this is not the cause of the observed effect. The time constant of the intensity-dependent absorption is much smaller than that of the photorefractive effect, and this suggests that they are physically different processes. In addition, the polarization dependence of the intensity-dependent absorption is similar to that of the standard, low-intensity absorption. Finally, the change in the magnitude of the intensity dependent absorption with reduction was opposite of what is expected if it were due to photorefractive gratings.

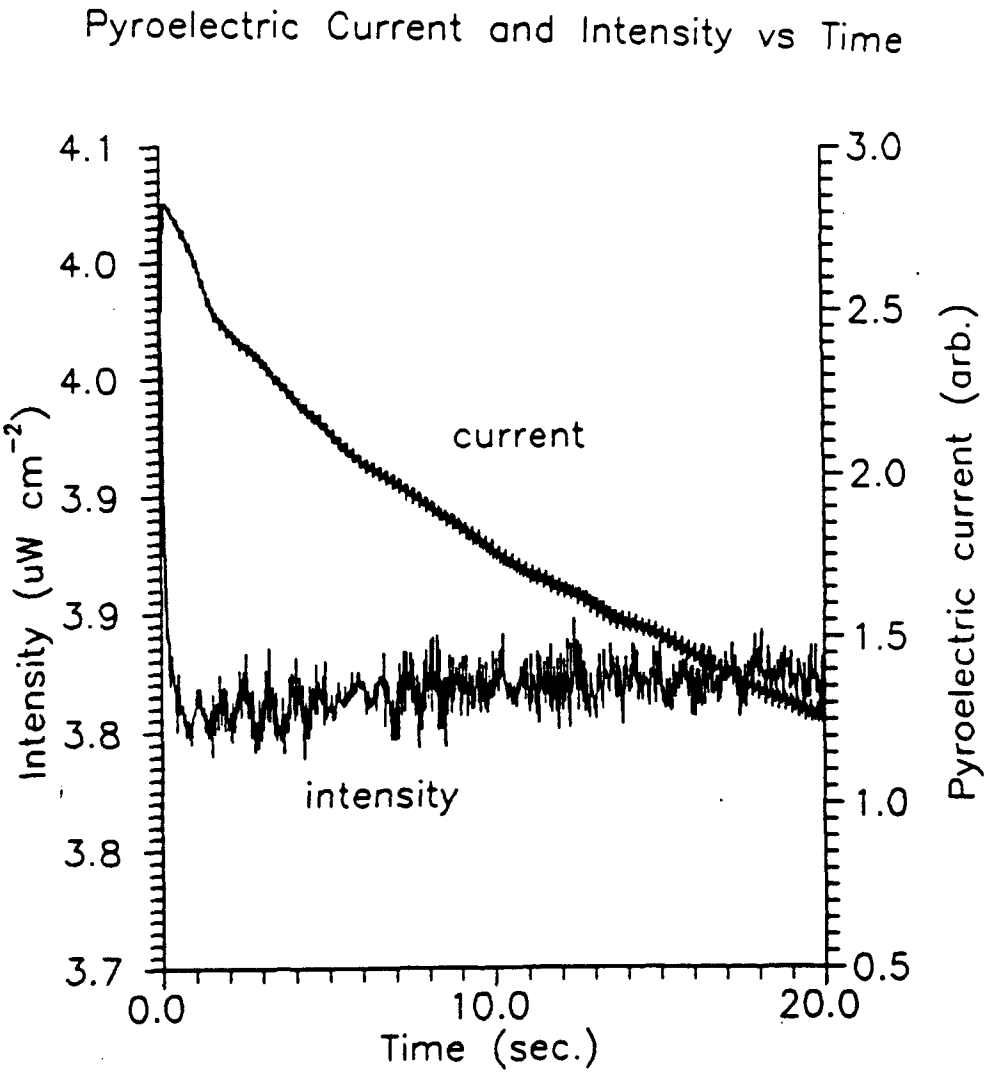

Fig. 2. **Simultaneous measurement of transmitted intensity and pyroelectric current.**

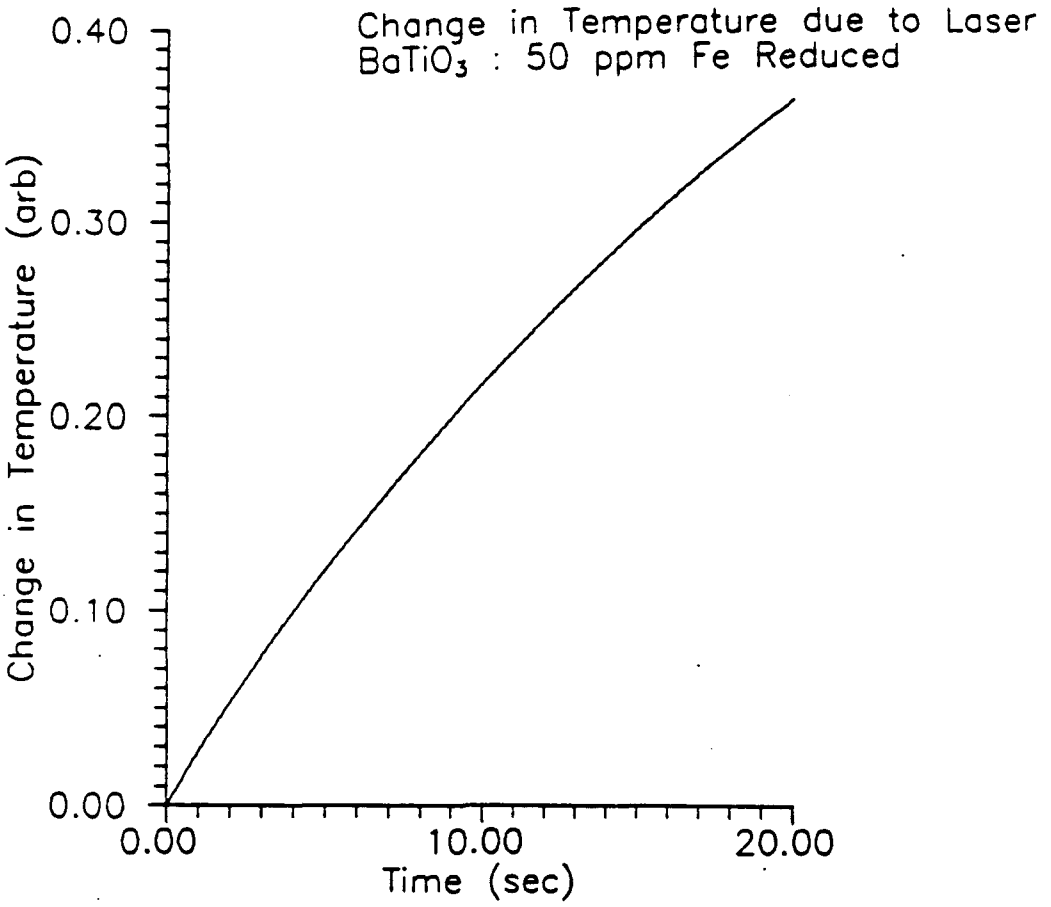

Fig. 3. Temperature change of the $BaTiO_3$ sample in arbitrary units as a function of time.

A variation of the apparatus described above was used to measure the spectral variation of the intensity-dependent absorption. In this apparatus, the probe beam was generated using a tungsten-halogen lamp and a Jarrell-Ash monochromator. Since the output of the monochromator was not collimated, lenses and apertures were used to achieve a narrow beam through the crystal. In addition an optical chopper and lock-in amplifier were used to improve the signal-to-noise ratio and eliminate the effects due to the scattering of the intense pump beam into the detector. This technique works as long as the small signal response of the photodetector is constant over a wide range of dc offsets. This assumption was tested experimentally by intentionally scattering part of the pump into the detector without a sample in the apparatus. Using an EGG BQ1100 photodiode as a detector, the output of the lock-in amplifier was unchanged exceptfor an initial transient which was expected. The experiment was attempted with a photomultiplier tube, but the photomultiplier was found to be too nonlinear to meet the above requirement. Due to the long relaxation time of the intensity-dependent absorption coefficient all sets of data were taken starting at the lowest pump intensity and progressing to the highest intensity.

The monochromator was calibrated against two standards. The first standard was an Oriel interference filter at 488 nm. The second standard was a garnet crystal which has both broad features and narrow lines in its visible

spectrum. The absorption spectra of this sample, taken with the Perkin-Elmer λ-9 spectrometer, was compared to the spectra taken in the intensity-dependent absorption apparatus. Figure 4 shows both of these spectra. A shift of 17 nm was required for overlap of the spectra. However, the overlap is good across the visible and the shift is in agreement with that found for the interference filter. All of the reported data have been shifted by this correction and represent true wavelength.

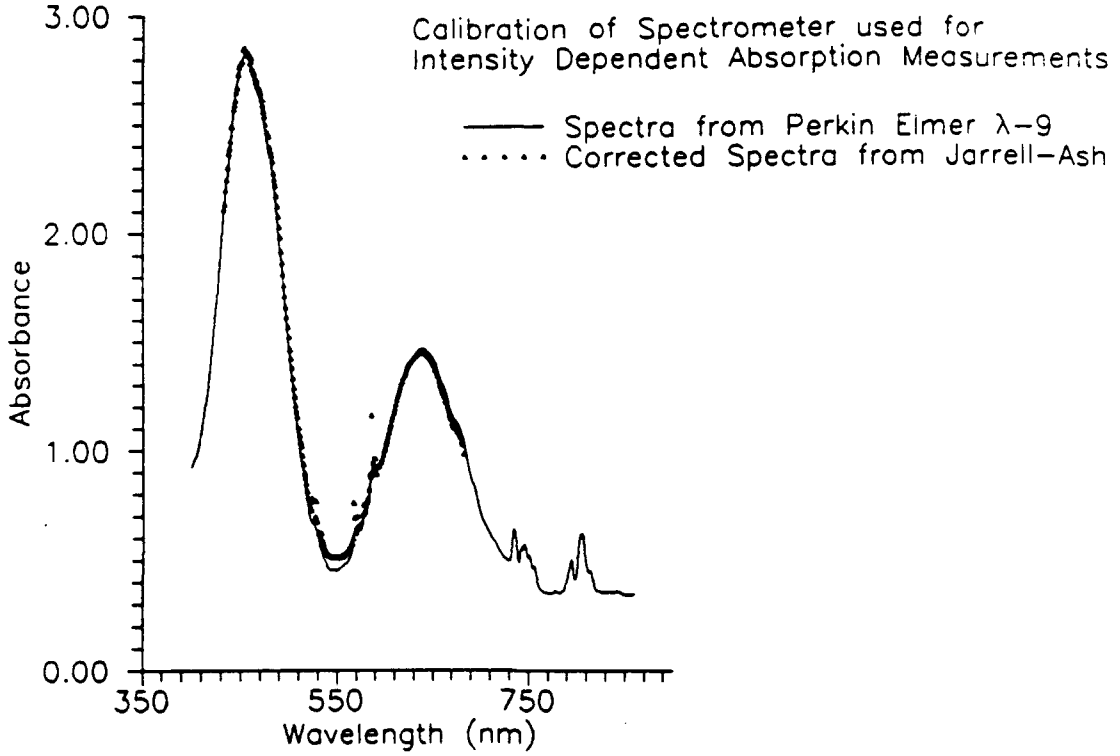

Fig. 4. Calibration spectra of the intensity-dependent absorption apparatus.

Results

The spectra of the change in the absorption coefficient is discussed next followed by the intensity dependence of the absorption coefficient. Finally, the time dependence of the intensity-dependent absorption is presented.

Figure 5 and 6 show the spectra of $\Delta\alpha$ for the pure as-grown and reduced crystal respectively. There are two important conclusions which can be observed from these data. First, there is almost no change in the absorption coefficient over the range of pump intensities used in this study. Second, the change is larger in the reduced sample than the as-grown sample. This is in contrast to reports in the literature which show significant intensity-dependent absorption in "nominally pure" samples.

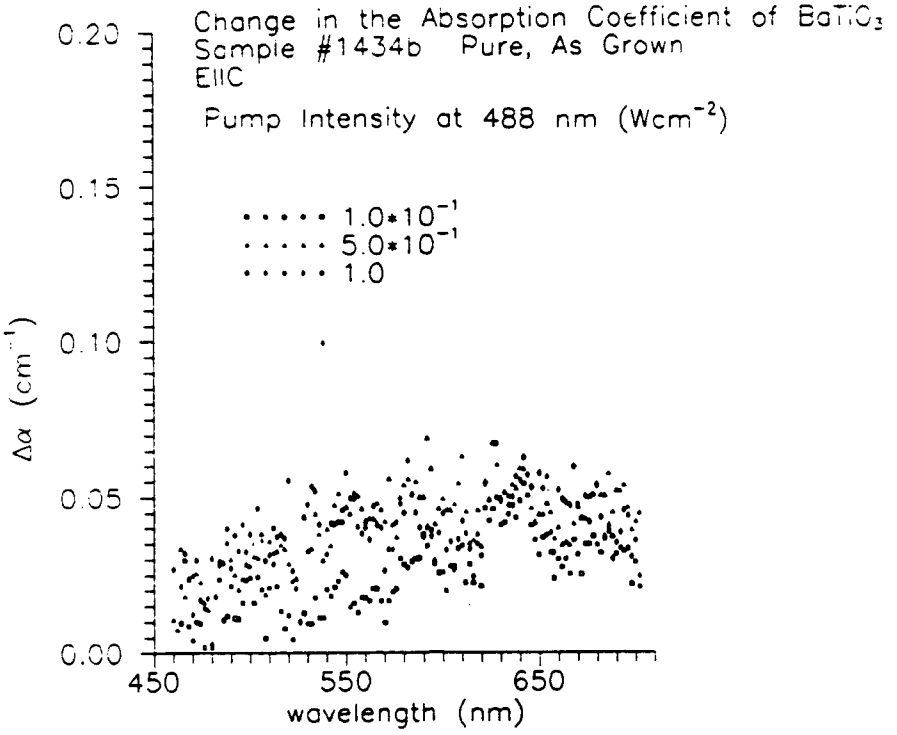

Fig. 5. Intensity-dependent absorption spectra of pure, as-grown $BaTiO_3$.

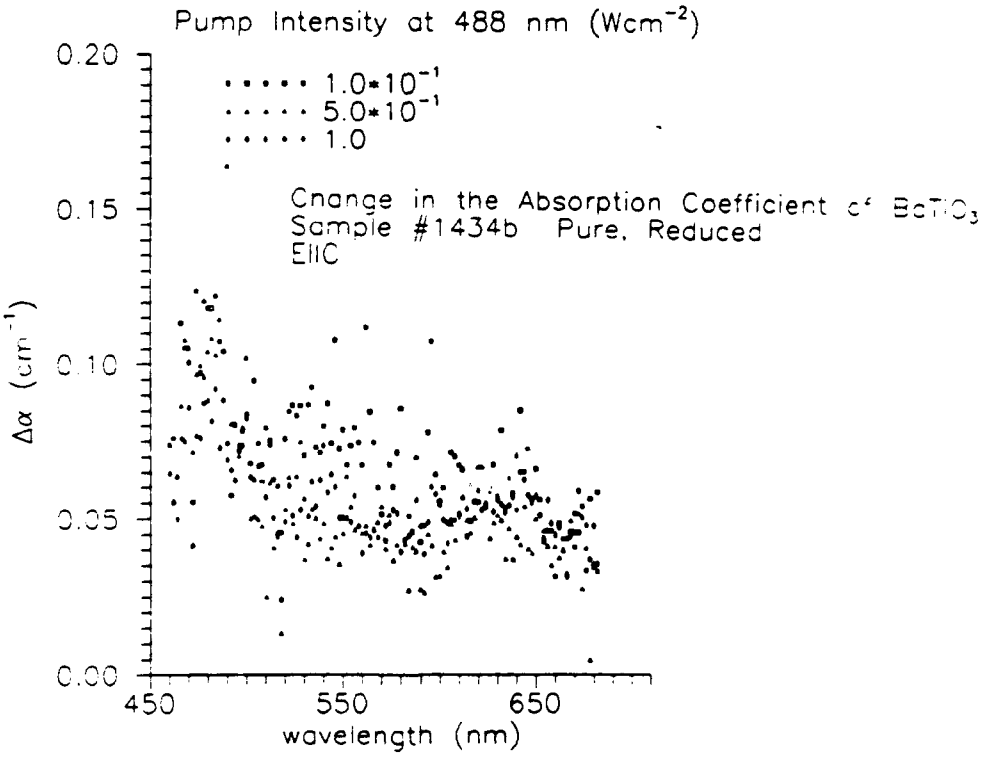

Fig. 6. Intensity-dependent absorption spectra of pure, reduced $BaTiO_3$

The effect of iron on this behavior is evident in Figs. 7 and 8 which how the spectra of the 50 and 500 ppm Fe doped samples in the as-grown state. The addition of iron increases the magnitude of the intensity-dependent absorption. In addition, the change iin the absorption coefficient is seen to always increase with intensity over the measured range. A very important feature of these spectra is that the greatest change in the absorption coefficient is at photon energies which are higher than the pump. Also the spectra are similar to the change in the low intensity absorption spectra with the addition of iron or with oxidation.

Figure 9 shows the spectra of the reduced, 50 ppm Fe doped sample. The intensity-dependent absorption is slightly less in this sample than in the as-grown sample of the same doping. Finally, Fig. 10 and 11 show the data for the as-grown, 1000 ppm Fe doped sample with the optical polarization parallel and perpendicular to the polar axis of the crystal respectively. All of the previous data were for the optical polarization parallel to the c-axis. Comparing Figs. 6 and 7 shows that the change in the perpendicular absorption coefficient is greater than the parallel absorption coefficient. This behavior was also observed in the 50 ppm Fe doped samples. Again, this is similar to the change observed in the low intensity absorption due to either adding iron or to oxidation.

These spectra indicate that the optical absorption increases with intensity, and the intensity dependence was examined using the two laser apparatus which yielded more reliable data. This was due to the more accurate control of the probe wavelength and collimated nature of the probe beam. Because there is no significant change in the absorption coefficient of the pure crystals these were not examined.

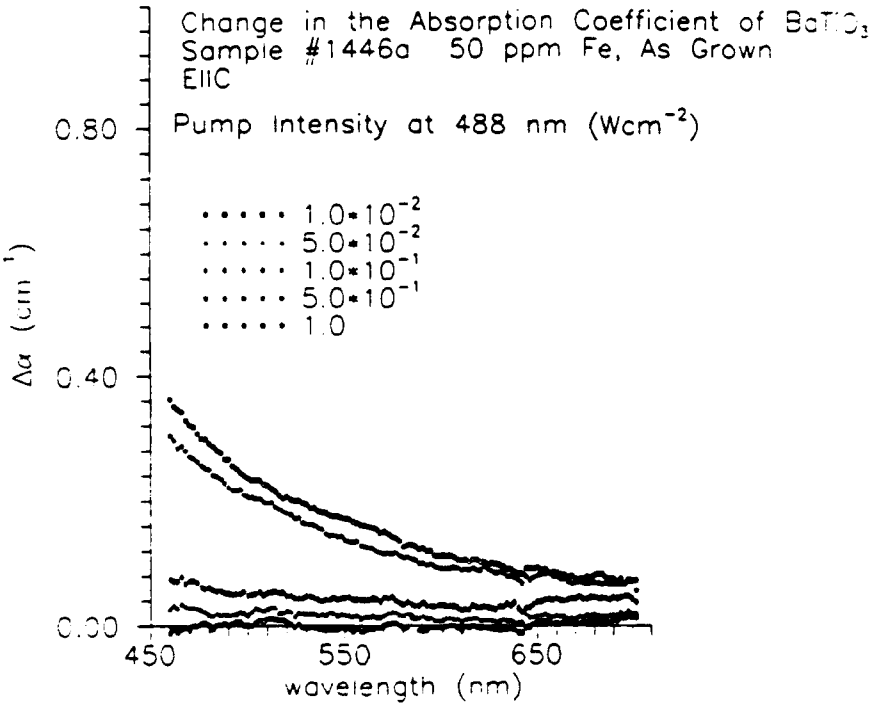

Fig. 7. Intensity-dependent absorption spectra of as-grown $BaTiO_3$ doped with 50 ppm Fe

The variation of $\Delta\alpha$ for the as grown, 50 ppm Fe doped crystal with pump intensity is shown in Fig. 12. The pump was 488 nm and the probe wavelengths are shown in the figure. This is a log-log plot and the lines are a least squares fit to a power law. The absorption is greater at the shorter wavelengths in agreement with the spectral data. Also, this provides a confirmation of changes in the absorption coefficient at photon energies greater than the pump photon energy. Data for the 50 ppm reduced crystal are shown in Fig. 13, and is similar to the as grown crystal. Again, in agreement with the spectral data, the change in the absorption of the reduced crystal is less than that of thew as grown crystal. Finally, Figure 14 shows the data for the 500 ppm sample. All of the data show similar trends. The change in absorption is larger at shorter wavelengths and it varies with intensity according to a power law within the range of intensities studied.

The temporal behavior of the absorption coefficient was also observed in these experiments. As discussed previously, the saturation intensity and the intensity without the pump can be used to find the change in the absorption coefficient. However, it is not necessay to wait for saturation. The measured time dependent intensity can be converted into a time dependent change in the absorption coefficient using Eq. 2. This was done and the curve was fit to an exponentiall. The time constants from the numerical fits were plotted against the pump intensity.

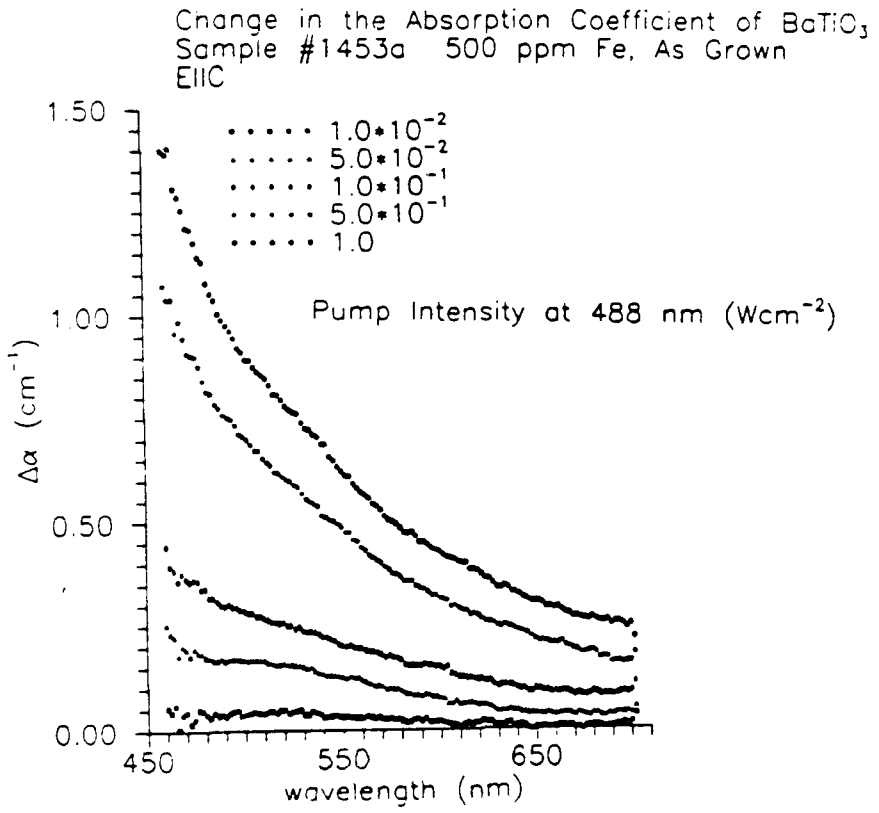

Fig. 8. Intensity-dependent absorption spectra of as-grown $BaTiO_3$ doped with 500 ppm Fe.

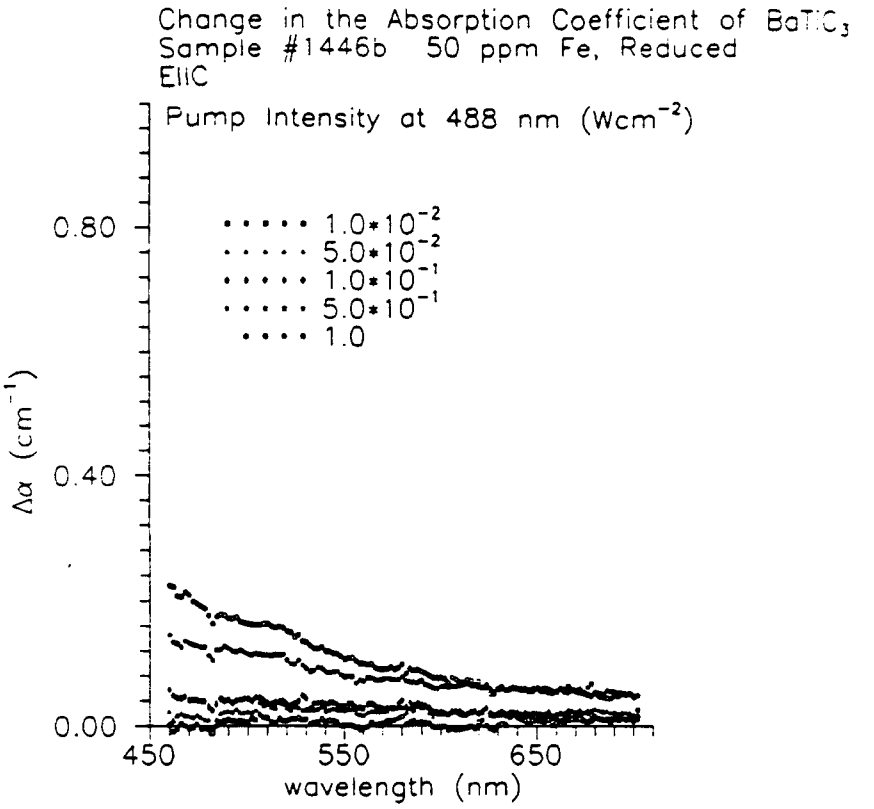

Fig. 9. Intensity-dependent absorption spectra of reduced $BaTiO_3$ doped with 50 ppm Fe.

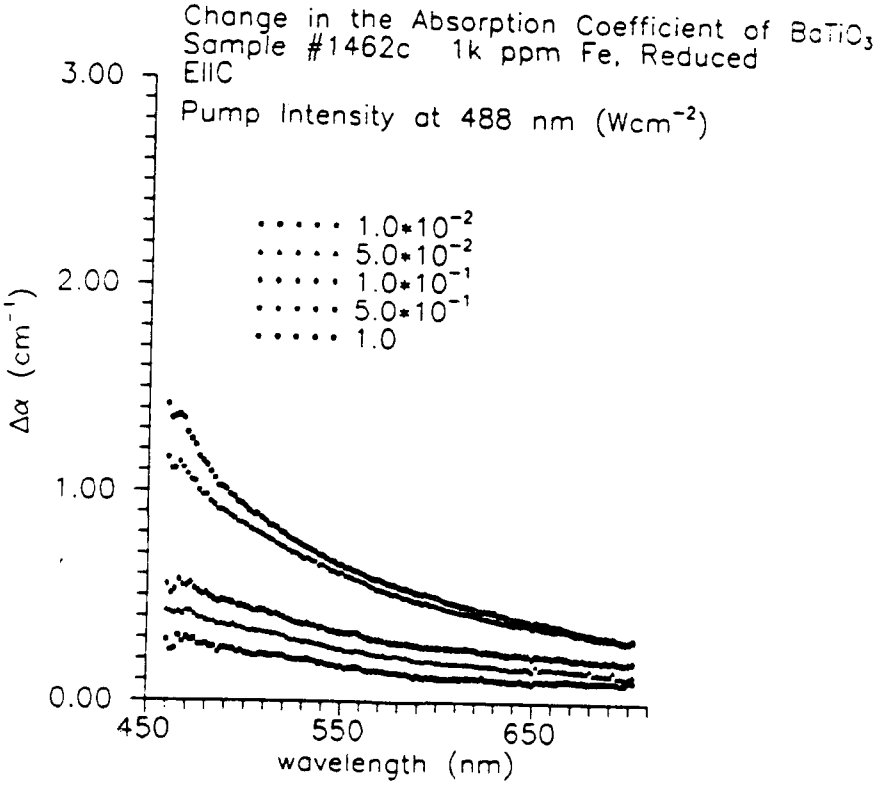

Fig. 10. Intensity-dependent absorption spectra of reduced $BaTiO_3$ doped with 1000 ppm Fe, E parallel to the c-axis.

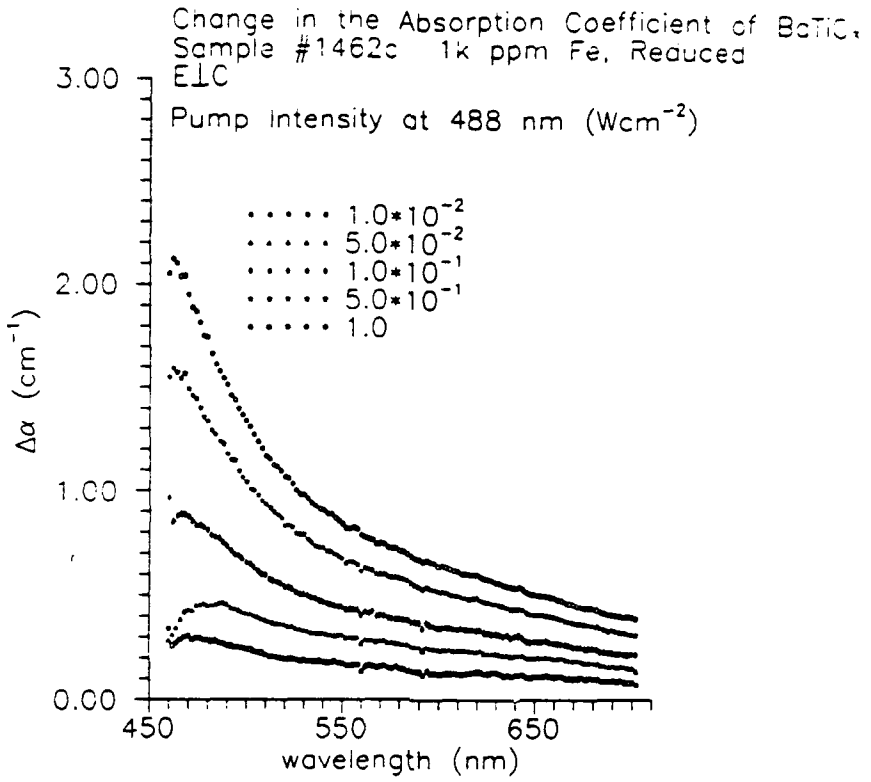

Fig. 11. Intensity-dependent absorption spectra of reduced $BaTiO_3$ doped with 1000 ppm Fe, E perpendicular to the c-axis.

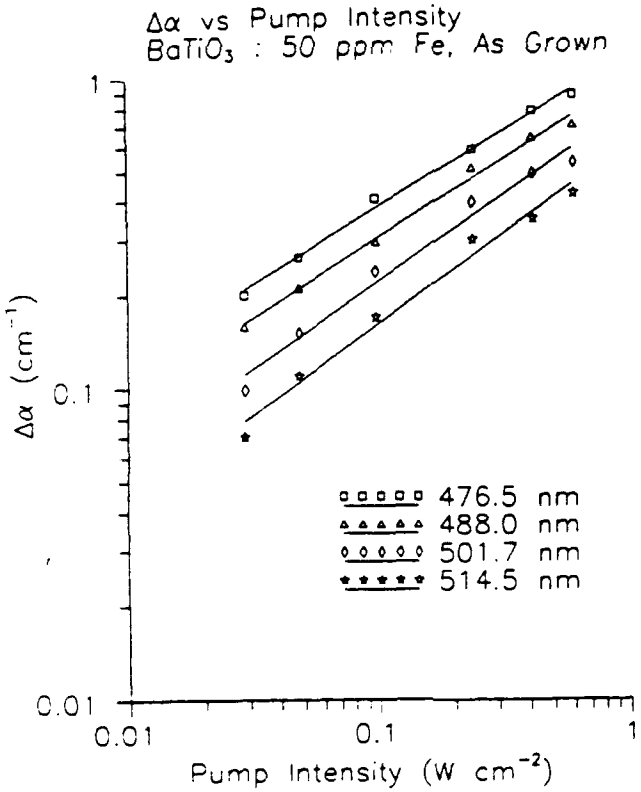

Fig. 12 Intensity dependence of $\Delta\alpha$ for as-grown $BaTiO_3$ doped with 50 ppm Fe

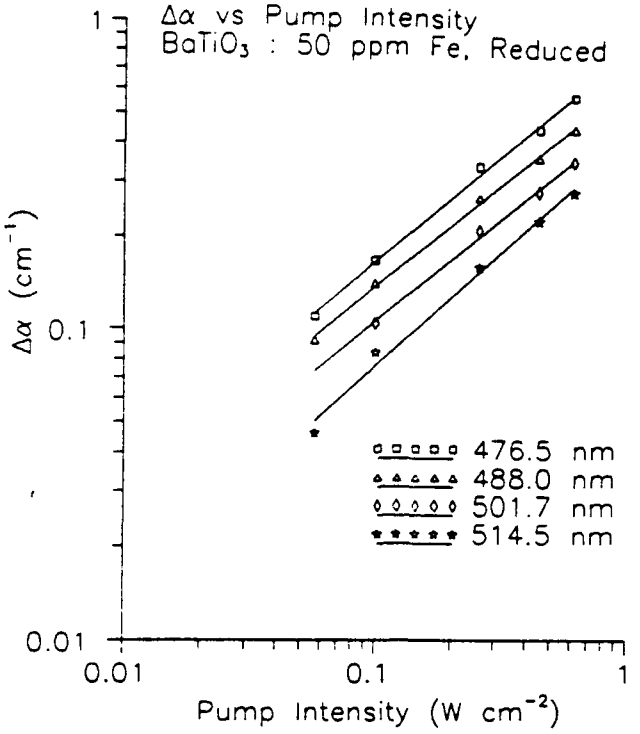

Fig. 13. Intensity dependence of Δα for reduced $BaTiO_3$ doped with 50ppm Fe.

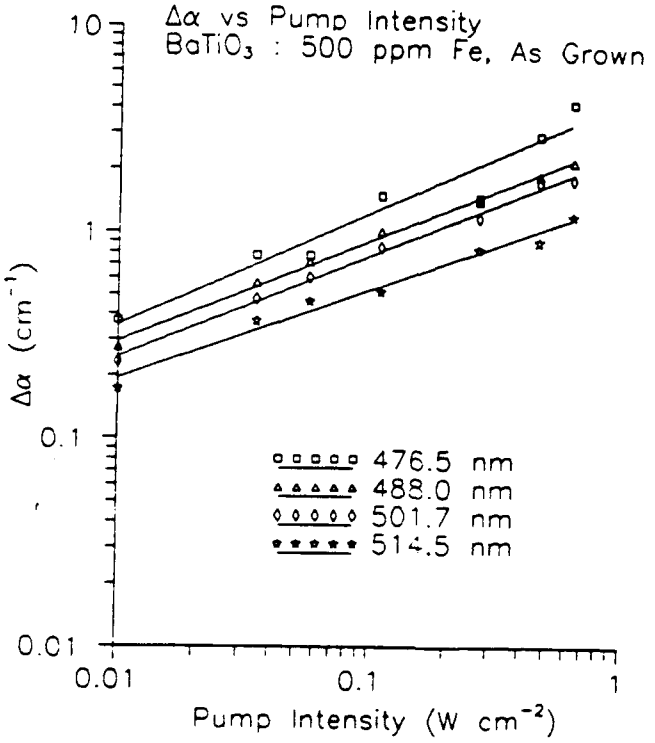

Fig. 14. Intensity dependence of Δα for as-grown $BaTiO_3$ doped with 500 ppm Fe.

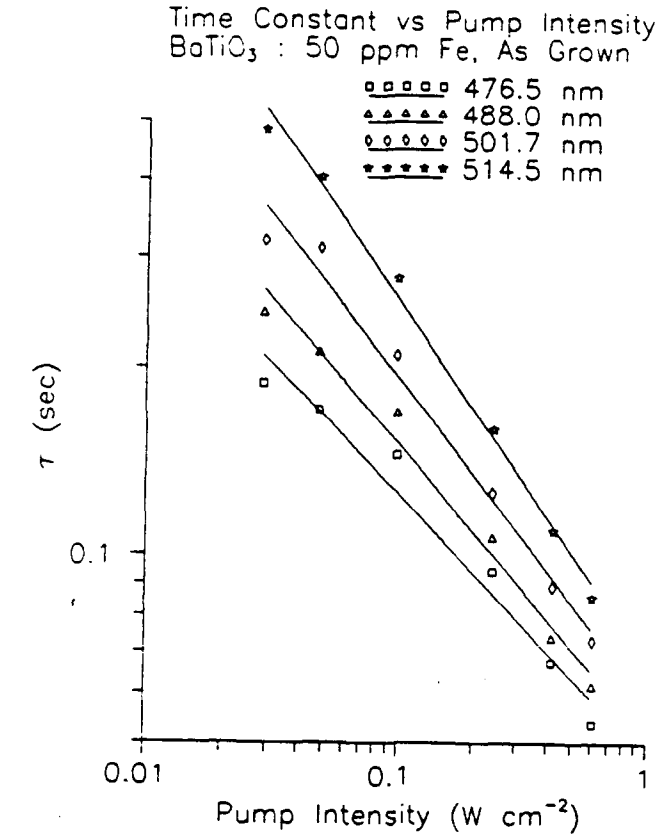

Fig. 15. Time constant of intensity-dependent absorption for as-grown $BaTiO_3$ doped with 50 ppm Fe.

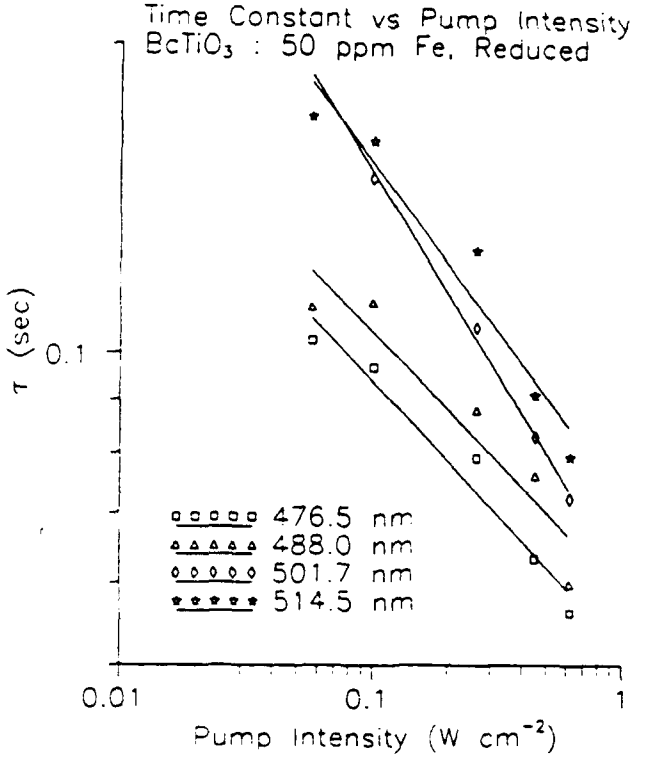

Fig. 16. Time constant of intensity-dependent absorption for reduced $BaTiO_3$ doped with 50 ppm Fe.

Figures 15 and 16 show the effects of reduction on the 50 ppm Fe doped samples. Both of these sets of data exhibit power law behavior. Apparently the reduction results in a smaller slope. Thhe addition of iron from 50 to 500 ppm causes an increase in the slope and an increase in the overall time constant at a given intensity as shown in Fig. 17.

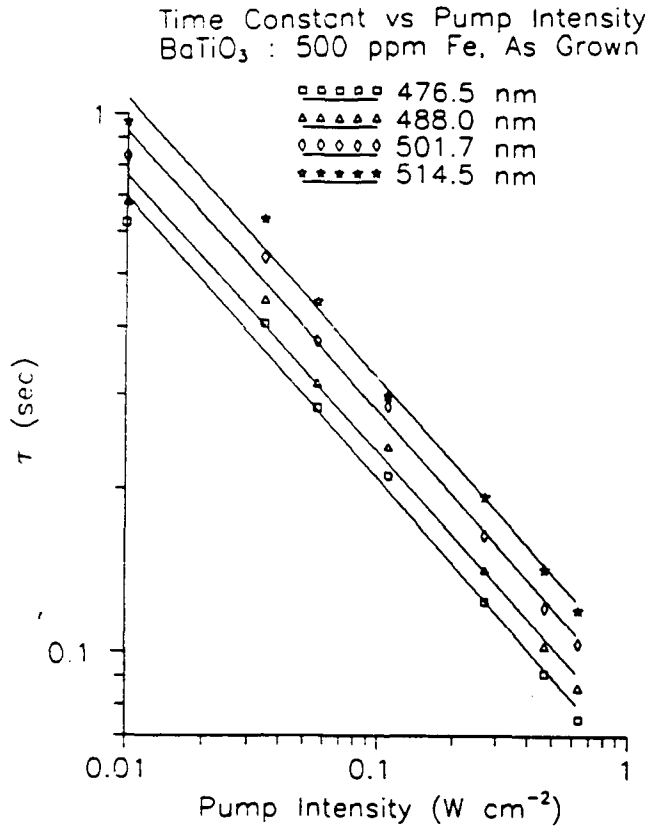

Fig. 17. Time constant of intensity-dependent absorption for as-grown $BaTiO_3$ doped with 500 ppm Fe.

Summary of Absorption Data

The absorption coefficient as measured by Schunemann *et al.*[7] increases with iron concentration and with oxidation at a fixed iron concentration. At high iron concentrations the absorption coefficient varies as $[Fe^{4+}]$ while at lower concentrations the data deviate from this model. The deviationcan be qualitatively explained by a model which includes both absorption by Fe^{4+} and an Urbach tail which is observed at wavelengths shorter than 500 nm.

Intensity-dependent absorption is observed in iron doped $BaTiO_3$. The absorption coefficient increases as a power of the intensity over the measured range of 0.01 to 1 Wcm^{-2}. This effect is stronger with increasing iron content. The data can be fit to the equation:

$$\Delta\alpha = AI^{x} \tag{4}$$

The rise time of the change in the absorption coefficient is also proportional to the intensity raised to a power. The decay is characterized by a fast decay followed in some samples by a very long (hours) decay time. The spectral variation of the absorption coefficient is similar to the change caused by increased iron doping or by oxidation. This includes a particularly interesting feature which is aa change in the absorption coefficient at shorter wavelengths than the pump wavelength. Finally, the change in the absorption coefficient is shown to not vary in the same way as the temperature. Thus, this is an electronic and not a thermal process.

REFERENCES

1. A. Motes and J. J. Kim, "Beam coupling in photorefractive $BaTiO_3$ crystals," Optics Letters 12, 199-201 (1987).

2. M. B. Klein and G. C. Valley, "Beam coupling in $BaTiO_3$ at 442 nm," J. Appl. Phys. 57, 4901-4905 (1985).

3. F. P. Strohkendl, J. M. C. Jonathan, and R. W. Hellwarth, "Hole-electron competiton in photorefractive gratings," Optics Letters 22, 312-34 (1986).

4. G. C. Valley, "Simultaneous electron/hole transport in photorefractive materials," J. Appl Phys. 59, 3363-3366 (1986).

5. A. Motes and J. J. Kim, "intensity-dependent absorption coefficient in photorefractive $BaTiO_3$ crystls," J. Opt. Soc. Am. B 4, 1379-1391 (1987).

6. G. A. Brost, R. A. Motes, and J. R. Rotge, "Intensity-dependent absorption and photorefractive effects in barium titanate," J. Opt. Soc. Am. B 5, 1879-1885(1988)

7. P. G. Schunemann, D. A. Temple, R. S. Hathcock, H. L. Tuller, H. P Jenssen, D. R. Gabbe, and C. Warde, "Role of iron centers in the photorefractive effect in barium titanate," J. Opt. Soc. Am. B 5, 1685-1696 (1988)

6 Color Front Dynamics in $BaTiO_3$

COLOR FRONT MOTION

The addition of iron to $BaTiO_3$ results in darker crystals in the as-grown state. In the more heavily doped as-grown samples, field-driven color fronts have been observed during electrical poling by Schunemann.[1] However, Schunemann was able to pole the samples before the color fronts progressed very far into the crystals, and he did not study the nature of the color fronts. Color front motion in $BaTiO_3$ is interesting because the low temperature diffusivity can be obtained from the speed of these fronts. Also they represent a potential problem in poling samples and an understanding of the nature of these fronts may allow a solution to this problem. The behavior of these fronts is different from the behavior of similar fronts reported in $SrTiO_3$.

Review of Literature

Field driven color fronts have been reported in $BaTiO_3$ by Kosman, and Bursian;[2] Ormancey, and Jullien;[3] and Godefroy *et al.*[4] Kosman, and Bursian observed a reddish brown color front moving from the anode toward the cathode in a reduced $BaTiO_3$ crystal at 300°C with an applied field of 3.33 kV/cm. They also noted a light blue region spreading from the cathode which is consumed by the advancing brown color front. At long times the crystal becomes uniformly brown. The original clear state could be restored by reducing the sample. Ormancey, and Jullien reported similar results with a dark region progressing from the anode at room temperature. They also report a clear region near the cathode, however it is not clear from their publication whether this region advances from the cathode. They also observe that the sample becomes uniformly dark at long times.

Blanc and Staebler studied the phenomena of electrocoloration in $SrTiO_3$[5]. They used a sample which was in an intermediate oxidation state and in order to verify the oxidation state of the sample during the experiment they doped $SrTiO_3$ with Ni and Mo. Oxidation resulted in a brown sample, and the color was due to the Ni ion. Reduction from the initial state yielded a blue sample. The blue color was assigned to the Mo ion. Blanc and Staebler also added Al to charge compensate the other dopants.

Upon application of an electric field at 300°C, they observed a brown region spreading from the anode, and a blue region spreading from the cathode. These two color fronts reduced the size of the clear region between them. When the field was reversed, the colored regions moved back toward the electrodes until the sample became clear and then the process begins again in the opposite direction. This "coloration" and "uncoloration" process could be repeated many times.[5] Because the brown region near the anode had a similar optical absorption spectra to an oxidized sample while the blue color near the cathode was the same as a reduced sample, Blanc and Staebler concluded that the color-front movement was due to the drift of oxygen vacancies. They developed a model for the movement of the color fronts during the "decoloration" of the crystal under constant current conditions which is valid for times short compared with the time required for a vacancy to move across the crystal. Their experimental data agreed with the predictions of the model within this constraint, and the value of

mobility extracted from the model, 1.5×10^{-8} $cm^2/Vsec$ at 200^0C, is in reasonable agreement with a value extrapolated from high temperature data. The observations of Blanc and Stabler are similar to those reported in $BaTiO_3$, except the sample did not become uniformly colored at long times and the original state could always be restored by reversing the field.

Wasser *et al.* have also observed color front movement in $SrTiO_3$:Fe.[6]. Their results are similar to those of Blanc and Staebler although it is not clear from their text what happens after long times. These authors also used the deflection of an electron beam in an SEM to map the potential in the sample as a function of time. This allowed them to verify that the colorless center region has a much greater resistivity than the colored end regions.[6] The difference in the resistivity was also reported by Blanc and Staebler. The conclusions of both of these reports is that oxygen vacancies are moved from one side of the crystal to the other by the electric field. This results in regions which have different electronic and optical properties.

Color front movement is not the only evidence of vacancy drift at low temperatures (293-400K). Williams studied the aging of switching properties in $BaTiO_3$.[7] This is a phenomena in which the amount of charge generated by switching the polarization of the crystal decreases with time if the switching pulses are asymmetric (i.e., a net dc field). This effect is explained by oxygen vacancies moving in the crystal and establishing an internal field which results in less depoling of the sample by the voltage pulse of opposite polarity. If the switching pulses are symmetric there is no net field and the oxygen vacancies do not move. The observations of Williams indicate that oxygen is not transferred through the aluminum electrodes which is in agreement with the work of Blanc and Staebler, and Wasser *et al.*, but he did observe ion transfer when using electrolyte electrodes.

Differences Between $SrTiO_3$ and $BaTiO_3$ Color-Front Motion

The color-front motion in $BaTiO_3$ results in a uniformly colored sample while this does not occur in $SrTiO_3$. In addition the process can be reversed in $SrTiO_3$ by reversing the field, but a high temperature anneal is required to reverse the effect in $BaTiO_3$. The color-front movement reported here differs from that reported in the $SrTiO_3$ literature in another significant way. The region near the anode becomes clear which indicates a reduced state. This is also in contrast to the observations reported for $BaTiO_3$ where the anode region becomes dark. However, in agreement with the literature on $BaTiO_3$ our samples could be restored to the original state only by a high temperature anneal. Since, in $SrTiO_3$, the electrodes do not allow ion transfer, the end of the crystal attached to the positive electrode becomes oxygen rich compared to the other end, and thus become darker like an oxidized crystal.

Experimental Procedures and Results

In order to better understand the color front movement, several experiments were performed on the iron doped crystals. A measurement of the motion of

the front as a function of time was made in order to obtain the mobility of the moving species. The optical absorption of the clear material was measured for comparison to reduced samples. Finally, beam coupling measurements were made on both sides of the front in an attempt to observe differences in the coupling gain due to the change in color.

A $BaTiO_3$ sample doped with 750 ppma iron was used for the study of the kinetics of the color-front motion. Because this sample had been poled, a color front had moved into the crystal some distance. The crystal was electroded using thin silver paste electrodes and placed in the poling apparatus shown in Fig. 1. This consisted of a peanut oil bath on a hot plate, and a temperature controller was used to maintain the temperature while a mercury thermometer was used for the temperature measurement. The sample was placed on a nickel plate and another nickel plate was lowered onto the sample to form the top electrical contact. The temperature was raised to 125^0C and a voltage of 1 kV was applied. A camera with a close up lens was used to record the position of the color front at intervals. The slides produced from this procedure were measured to provide the actual distance that the color front had progressed into the crystal.

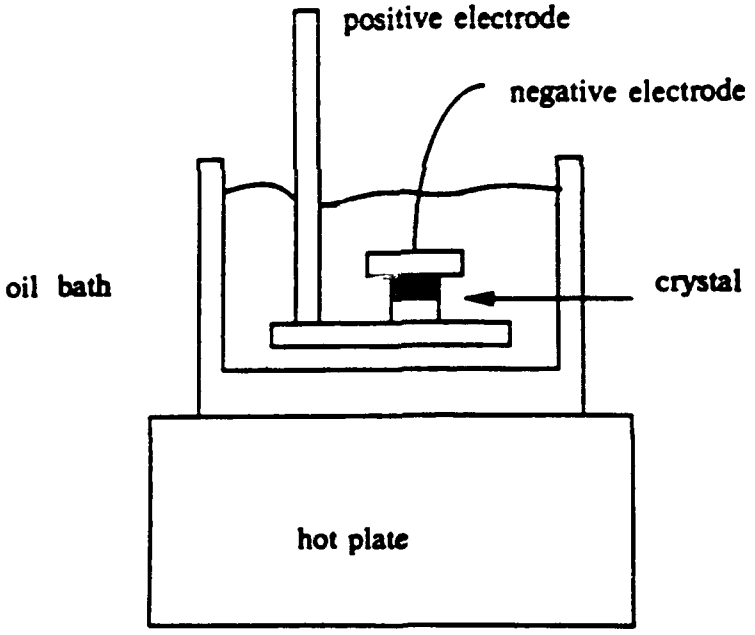

Fig. 1. Apparatus used in color front movement.

Figure 2 shows the color front progression at several times. The bottom electrode is positive, and the clear region is moving from bottom to top in the pictures. Although the color front moves as a stable, sharp boundary

between the two colored regions, there is some curvature across the crystal. Since the amount of curvature did not change much during the experiment the position of the front was taken as the average of the positions of the front at each edge of the crystal. The position of the color front as a function of time is shown in Fig. 3. Note that unlike the work of Blank and Staebler who performed their experiments under constant current conditions, these data are for constant voltage conditions. Although constant current would have made the analysis easier, it was not possible because the conductivity of the oil was greater than that of the crystal.

t = 0 (min.) t = 474 (min.) t = 1278 (min.)

Fig. 2. Color front motion in $BaTiO_3$:Fe.

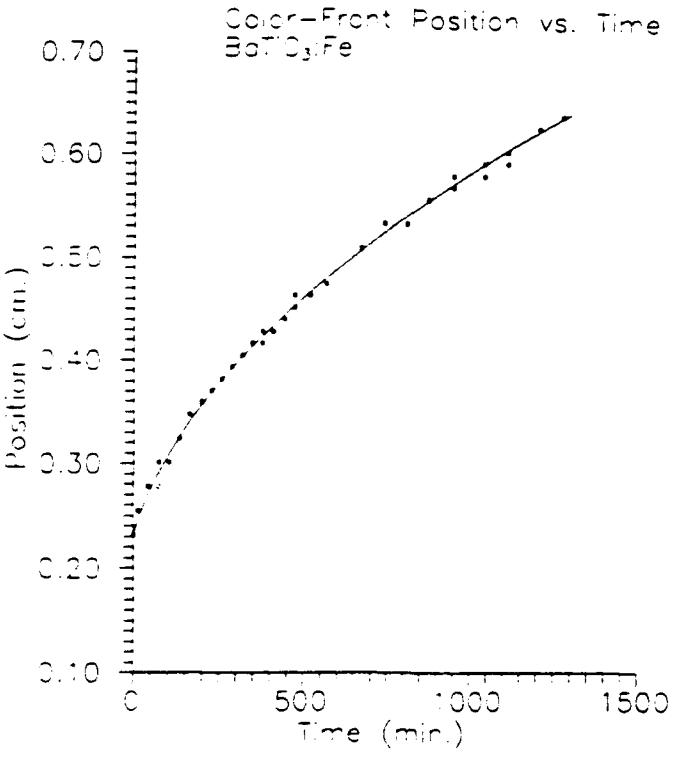

Fig. 3. Motion of the color front.

After 1278, minutes the field was reversed in an attempt to reverse the motion of the color-front and return the crystal to its original state as reported for $SrTiO_3$. The original color front moved very slowly backward and became diffuse, while a second clear region developed at the top electrode which was now positive. This resulted in a sample which was clear on both ends and dark in a narrow band between the clear regions. The second color-front moving down from the top electrode overtook the first color-front and the crystal became uniformly clear. This behavior is similar to that observed by Kosman with clear and dark interchanged.

Since the clear region could not be removed from the crystal by reversing the voltage as in $SrTiO_3$, the assumption of no ion transfer at the electrode becomes suspect. To test this assumption the color front measurement was repeated in air. The sample used was the clear sample which resulted from the previously described experiment. No sharp color front was observed making it impossible to obtain quantitative data on the ion movement. However, the sample became streaked with darker regions, and after a long time was noticeably darker. This indicates that changing the environment from oil to air causes a change in the nature of the field driven color front, and is strong evidence that oxygen is transversing the electrodes. This experiment was accidentally repeated on the 1000 ppma sample which had a color front in the center of the crystal. The sample was being repoled in air instead of oil to avoid increasing the size of the clear region. Figure 4 shows the results of this error. Note that the second color front is more diffuse than the first but it is not as diffuse as that observed in the 750 ppma crystal. Finally, the experiment was repeated in oil with evaporated aluminum electrodes. In this case the electrode is blocking to ion transfer and the positive electrode became darker. This behavior is opposite of that observed with silver paste electrodes, and indicates that when the electrodes are blocking, the oxygen vacancies move away from the positive electrode leaving an oxidized region.

Fig. 4. Multiple color fronts in crystal.

Finally the 750 ppma sample was annealed in air at 850°C. and quenched into a furnace at 200°C. as described by Schunemann.[8] This returned the sample to a uniform dark state similar to that of the as-grown state. In order to verify the reduced nature of the clear region resulting from color-front movement, an attempt was made to repeat the first color-front motion experiment with laboratory grade N_2 instead of oil. Although a clear region developed at the positive electrode and began moving into the crystal, it soon was replaced by a dark region at the positive electrode. Because the

clear region was very small and becoming diffuse the experiment was terminated at this point.

In order to characterize optical absorption and beam coupling of both sides of the color front, the 1000 ppma iron doped sample was placed in the oil bath poling apparatus. Care was taken to apply the voltage in the same direction as in the previous poling operation. The correct direction was determined by observing the small clear region due to the previous poling and by measuring the pyroelectric effect. Both methods confirmed the direction of the c-axis. The sample was heated to approximately 125°C and the voltage, 1 kV, applied until the color front was approximately in the center of the crystal. After cooling the sample showed no 90° domains when examined between crossed polarizers and gave a strong pyroelectric reading. These indicate that the crystal was well poled although 180° domains can not be absolutely ruled out.

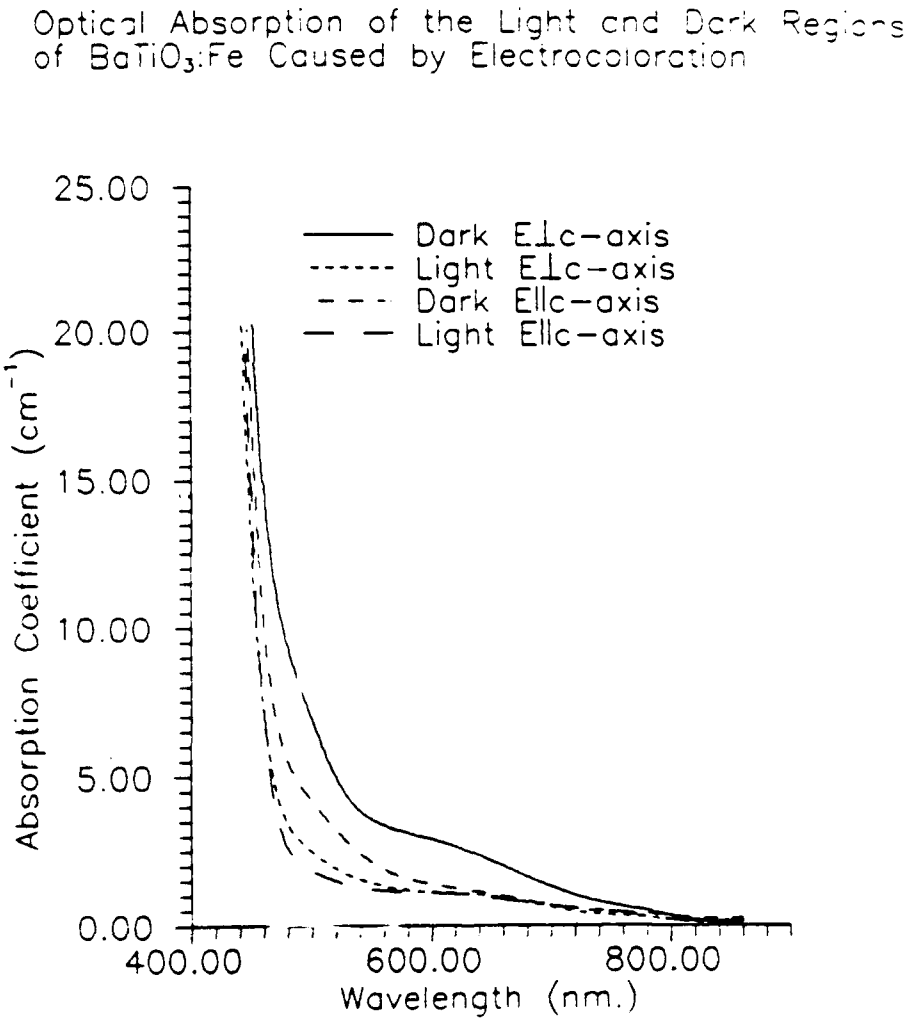

Fig. 5. Absorption of dark and light regions caused by color front motion in as-grown $BaTiO_3$ doped with 1000 ppm Fe.

The optical absorbance of both the light and dark regions were measured using the Perkin-Elmer λ-9 spectrometer. The absorbance was converted to absorption coefficient and is shown in Fig. 5. It is seen that the dark region has absorption characteristic of the iron doped samples with the shoulder at 620 nm in the spectrum for the optical polarization perpendicular to the c-axis. In contrast to this, the clear region shows no structure and smaller absorption through out the visible. These data indicate that the clear region has significantly less Fe^{4+} than the dark region.

Beam coupling was performed on both the light and dark sections of the crystal. However, the signal averaging capability had not been added to the control program so all the data presented here represent a single data run. Furthermore, because the size of the colored region is approximately half that of the crystal, it was impossible to obtain good data at the larger angles. However, since the beam-coupling measurement was made on both sides of the color-front under the same experimental conditions and without further processing of the sample, these data should yield a valid comparison of the light and dark regions.

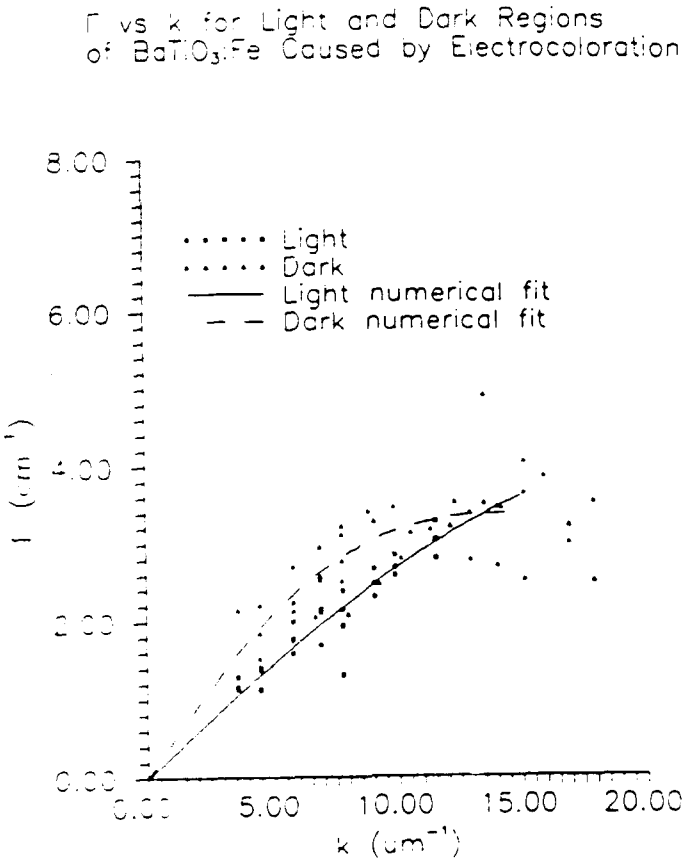

Fig. 6. Two beam coupling on both sides of the color front in as-grown $BaTiO_3$ doped with 1000 ppm Fe.

Figure 6 shows the two-beam coupling gain as a function of grating vector for both sides of the sample. The solid lines represent numerical fits to the theory. The numerical fit of the data for the light side of the sample gives values of $0.30*10^{-4}$ and 30.2 μm^{-1} for A and K_o, respectively. In the dark half of the sample, these values are: $A = 0.47*10^{-4}$ and $K_0 = 14.3\ \mu m^{-1}$. This supports the absorption data in suggesting that the clear region is reduced compared to the dark region. Further agreement is found in the time constant data. The time dependence of the beam-coupling is shown in Figure 7. The lines represent linear least-squares fits to the data. Note that, as expected, the clear region has a small negative slope while the dark region has a positive slope. The value of photoconductivity is only slightly smaller for the clear region and both values of photoconductivity are the same order of magnitude as those reported elsewhere for as-grown $BaTiO_3$.

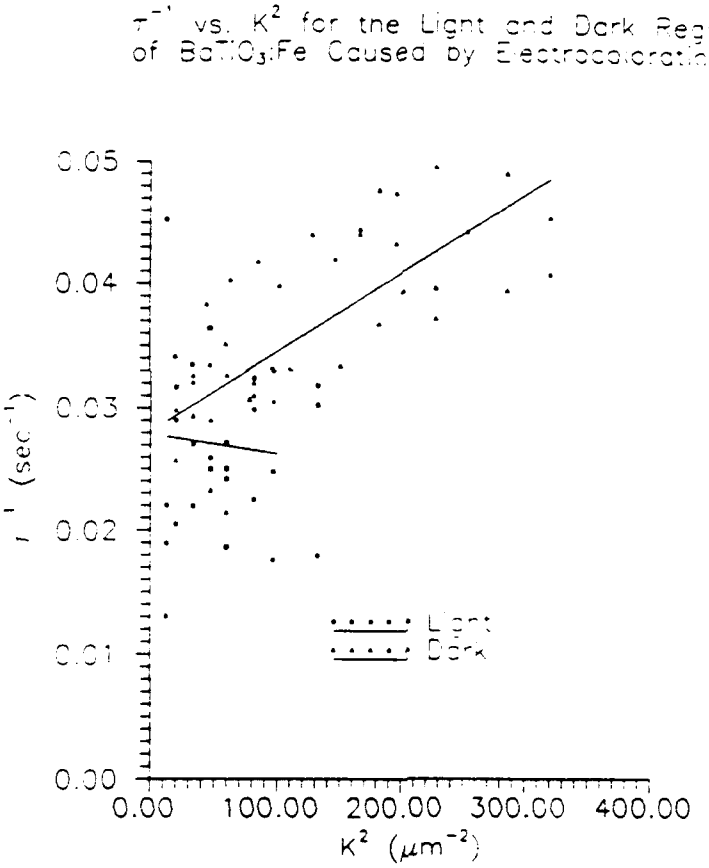

Fig. 7. Beam-coupling time constant on both sides of the color front.

Modeling

In order to explain the observed behavior associated with the color front in iron doped $BaTiO_3$, a physical model was be proposed. This model was be used

to develop equations which describe the movement of the color front. Since the color front process is not reversible and depends on the environment, the model will assume that oxygen is transferred at the electrodes. This is the general case and the special case of blocking electrodes can be achieved by making the transfer infinitely slow. The model will assume that a color front already exist in the crystal, otherwise it is necessary to deal with a discontinuity which is mathematically more difficult. Also in the early stages of formation diffusion or other mechanisms may become important.

A schematic of the crystal with a color front is shown in Figure 8 along with the definitions of various symbols. In this model we will treat oxygen vacancies as a chemical species which has an activity in the environment outside of the crystal. Obviously these do not have meaning outside of the crystal but since the oxygen activity sets the equilibrium vacancy concentration we can use this mathematical convenience.

The general model consists of an environment with an oxygen activity which would produce an equilibrium vacancy concentration $[V_o]_{env}$ in the $BaTiO_3$ sample at the temperature of the experiment. Next there is a generalized boundary layer around the crystal. This layer could represent any of the following processes: boundary layer diffusion, surface layer diffusion, and/or surface reaction. It will assumed that this is a first order process with the flux proportional to the concentration difference. Although, this is not necessarily correct for surface chemical reactions, it simplifies the math and the general conclusions are not greatly affected. Finally, the crystal will be assumed to have an oxygen vacancy which varies with space and time. This variation of the oxygen vacancy concentration causes a local variation of the electronic conductivity.

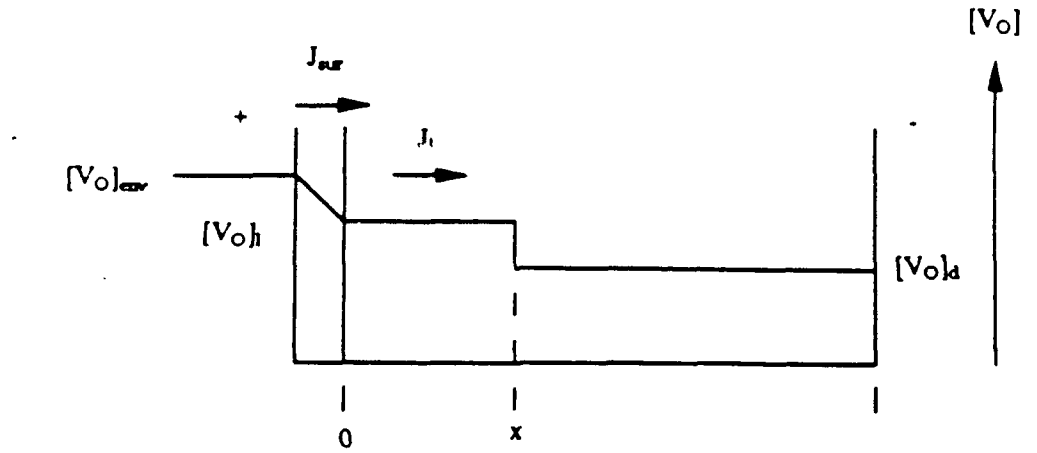

Fig. 8. Model for color front motion.

The general model described above can not be solved exactly, so one is faced with the choice of approximation or numerical simulation. In this section, it will be shown that with reasonable approximations the model can be reduced to an analytic form which fits the data with reasonable values of the parameters. As discussed above the irreversibility of the clear color front indicates that oxygen is being transferred at the surface and this

will be modeled by a flux into the surface:

$$J_{sur} = k_s([V_0]_{env} - [V_0]_{sur}) \quad (1)$$

where k_s is a transport constant.

We now make a very important simplification, and assume that the oxygen vacancy concentration is constant through out each separate region of the crystal. We will designate the concentration in the dark region as $[V_0]_d$ and $[V_0]_l$ in the light. Although the interface between the two regions will have a diffusion profile, it will be very sharp as diffusion is very slow at these temperatures. For simplicity we will treat it as a step function. We can argue that these simplifications are justified by the visual uniformity through out both the clear and dark regions during the forward color front movement. The uniform concentration of vacancies across a region allow us to assign a conductivity to that region. These conductivities are made up of both electronic and ionic terms.

The next approximation is to assume that the conductivity of the dark region is much greater than that of the clear region. Although this assumption is directly verifiable in principle, it proved quite difficult to do so. However, indirect evidence will be presented to support this assumption. Before examining this evidence let us consider the cause of the dark color. We know that the photoexcited carriers in both regions are holes from the beam coupling direction. We also know that the color is enhanced by oxidation and by optical pumping; both are processes which lead to an increase of holes. These considerations indicate that both sides of the crystal are p type and the dark side is more p type. This would result in the dark region having a larger electronic conductivity. Note that both conductivities are still exceedingly small which makes direct measurements difficult.

The indirect evidence that the conductivity of the dark region is larger than that of the light region is the stability of the front in the forward (i.e. clear region moving toward dark region) direction contrasted to the instability of the front moving in the reverse direction. As pointed out by Blanc and Staebler[5] if all the field is dropped across the region which is becoming longer then the motion will be stable. The reason for this can be seen in Figure 9.

In case 1, all of the field is dropped across the clear region. If a perturbation occurs which causes a local portion of the clear region to move ahead of the front then the local field is decreased. This happens because a fixed voltage is applied across a longer region. The reduced field causes the perturbed portion to move more slowly which tends to flatten the color-front. Thus this is condition results in stable color-front motion. Similarly a perturbation in the opposite direction has a higher local field which acts to restore the front. In case 2, all of the field is across the dark region. Now a perturbation in the direction of the front motion reduces the local field. This increases the perturbation and would result in the diffuse appearance which is observed when the field is reversed.

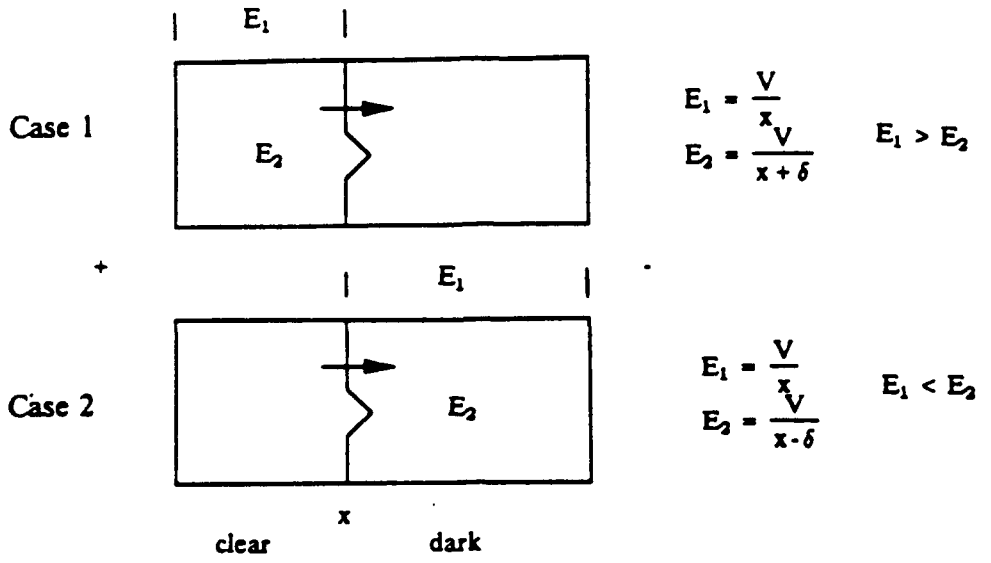

Fig. 9. Stability of color front motion.

With these approximations there are two fluxes which must be balanced in steady state. The surface flux into the clear side described in Eq. 1 must equal the flux in the clear side. The flux in the clear side is given by:

$$J_l = [V_0]_l \, \mu_V \, E_l \tag{2}$$

The electric field is given by the position of the color front:

$$E_l = \frac{V}{x_0} \tag{3}$$

The balance of Eqs. (1) and (2) results in:

$$[V_o]_l = \frac{k[V_o]_{env}}{\mu_V \frac{V}{x_o} + k} \tag{4}$$

In order to use the flux to predict the movement of the color front we must examine the continuity equation for an infinitesimal region $\Delta\chi$ in the direction of color front motion from the present front position. The flux into this region is simply J_l since the no field condition in the dark region results in $J_d = 0$. The length of time needed to change the concentration of this region which was initially dark to that of the light region is:

$$\Delta t = \frac{([V_O]_l - [V_O]_d) A \, \Delta x}{J_l A} \qquad (5)$$

where A is the cross sectional area. By letting the finite differences become derivatives and rearranging this equation we get a differential equation for the position of the color front. Integrating this equation and using Eqs. (1)-(4) gives an analytical expression for the position of the color front:

$$x = \frac{\mu_V V}{k(r-1)} \pm \left[\left(x_o - \frac{\mu_V V}{k(r-1)} \right)^2 + \frac{2}{1-r^{-1}} \mu_V V t \right]^{1/2} \qquad (6)$$

The initial position is x_0 and r is the ratio of $[V_O]_{env}$ to $[V_O]_d$. This form was numerically fit to the data using commercial software. The theoretical curve is plotted as a solid line in Fig. 3. The numerical fit gives a value for the mobility at 125°C of $1.46*10^{-9}$ $cm^2 V^{-1} sec^{-1}$. The concentration ratio is 2278 and the surface rate constant is $4.2*10^{-9}$ $cm.sec^{-1}$. For any value of r much greater than one, r does not affect the time dependent term. In this case r and k appear multiplied together and the fit is not changed much by raising one and lowering the other. Therefore the absolute magnitude of r and k are less well known than μ from fitting these data.

The equation of motion of the color front was also solved assuming fast transport at the surface and an electric field in both regions. The electric field in each region is now determined by the relative conductivities and widths of the regions. Using this model the condition of all of the field being dropped across one region is relaxed. However, the numerical fit which followed the data closely produced a nonphysical value for the ratio of the conductivities. It is interesting that the value of mobility derived from this model is within a factor of two of that derived from the above model.

Using the Einstein equation, the diffusion coefficient, D, is $2.6*10^{-11}$ $cm^2 sec^{-1}$. With this, it is possible to estimate how long it would take for the sample to become clear without the applied field. For this purpose we will assume a 1 cm cube of $BaTiO_3$ in the oil bath at 125°C. The initial concentration of oxygen vacancies will be labeled C_0, and the total change in this concentration when the crystal has reached equilibrium with the oil is Δ. The equation for the average concentration after equilibrium is nearly established is;

$$\bar{C} = C_0 + \Delta \cdot \left[1 - \frac{8^3}{\pi^6} exp\left(-\left(\frac{\pi}{l}\right)^2 3D t \right) \right] \qquad (7)$$

We now ask how long it takes for the change in the average concentration to reach 99% of the total change. This is given by:

$$1 - \frac{8^3}{\pi^6} exp\left(-\left(\frac{\pi}{l}\right)^2 3D\,t\right) = 0.99 \qquad (8)$$

Solving for time, t, and using the diffusion coefficient derived from the mobility the time required for the crystal to become clear due to diffusion at 125^{0}C is approximately 164 years. This is why we do not observe any clear region on the faces which are not electroded.

Summary

Field driven color fronts have been observed in iron doped $BaTiO^3$ which do not behave in the same way as those observed in $SrTiO_3$. While in $SrTiO_3$ the electrodes do not allow oxygen transfer, the experimental evidence presented here suggests that the silver paste electrodes used in this study allow oxygen transfer. Based on this assumption, the color front can be treated as a field driven step increase in the oxygen vacancy concentration. The vacancy mobility needed to fit the data with this model is reasonable, and the optical absorption data are also consistent with the light colored region being a reduced region. Although noisy, the beam coupling data also support this assumption, and confirm that both regions remain p-type.

Although the model gives an estimate of the oxygen activity in the oil, it is not sensitive to this parameter so the actual degree of reduction is unknown. Finally, the model proposed here can explain the color-front motion in $BaTiO_3$ reported in the literature while the model proposed for $SrTiO_3$ cannot. The important difference is the ability to transfer oxygen across the surface of $BaTiO_3$.

REFERENCES

1. P. G. Schunemann, D. A. Temple, R. S. Hathcock, H. L. Tuller, H. P Jenssen, D. R. Gabbe, and C. Warde, "Role of iron centers in the photorefractive effect in barium titnate," J. Opt. Soc. Am. B 5, 1685-1696 (1988).

2. M. S. Kosman and E. V. Bursian, "Coloration of $BaTiO_3$ single crystals," Dokl. Akad. Nuak SSSR 115, 483 (1957) [Sov. Phys. Doklady 2, 354-356 (1957)].

3. G. Ormancey, and P. Jillien, "Electric and optical properties of $BaTiO_3$:Fe," Ferroelectrics Lett. 1, 103-106 (1983).

4. G. Godefroy, G. Ormancey, P. Jullien, Y. Semanou, and W. Ousi-Benomar, 1986 IEEE International Symposion on Applications of Ferroelectrics (ISAF), June 8-11, Lehigh University, Bethlehem, PA., PA-1.

5. Joseph Blanc, and David L. Staebler, "Electrocoloration in $SrTiO_3$: Vacancy drift and oxidation-reduction of transition metals," Phys. Rev. B 4, 3548-3557 (1971).

6. R. Wasser, "Degradation of dielectric ceramics," to be published.

7. Richard Williams, "Surface layer and decay of the switching properties of barium titanate," J. Phys. Chem. Solids 26, 399-405 (1965).

8. P. G. Schunemann, *Growth and Characterization of High-Purity and Iron-doped Photorefractive Barium Titanate*, Masters Thesis Massachusetts Institute of Technology, 1987.

7 Appendix (Publications)

7.1 Photoinduced Optical Absorption in $BaTiO_3$:Fe
7.2 Intensity Dependent Photorefractive Properties of $BaTiO_3$

Photoinduced optical absorption in $BaTiO_3$:Fe

Doyle A. Temple[a] and Cardinal Warde
Departments of Physics and Electrical Engineering and Computer Sciences, Massachusetts Institute of Technology, Cambridge, Massachusetts 02139

(Received 12 November 1990; accepted for publication 2 April 1991)

Measurements of the steady state photoinduced absorption $\Delta\alpha$ have been performed on single crystalline samples of pure and iron-doped $BaTiO_3$. The results show that $\Delta\alpha$ has a sublinear intensity dependence, similar to that observed in photorefractive grating decay measurements.

Determination of the origin of the centers responsible for the photorefractive effect in $BaTiO_3$ is complicated by the presence of several competing effects including stimulated photorefractive scattering (commonly known as beam fanning),[1,2] anisotropic scattering,[3-5] and photoinduced absorption.[6-10] To better aid in modeling of these charge transport processes, experimental methods must be employed that effectively decouple these competing effects.

The first measurements of the photoinduced absorption in $BaTiO_3$ were performed by Motes *et al.*[6-8] and Brost *et al.*[9] More recently, Pierce *et al.*[10] showed that absorption gratings could be produced in $BaTiO_3$ using a configuration that does not allow photorefractive beam coupling. Using this method, these authors were able to determine the trap density associated with the absorption gratings.

Iron has long been suspected as being the active photorefractive center in $BaTiO_3$. Klein and Schwartz[11] found a good correlation between the iron concentration and the photorefractive trap density in various commercial samples. Although these samples had several impurities that could be photorefractive centers, the strongest correlation was with the iron concentration. Godefroy *et al.*[12] measured the diffraction efficiency in unpoled, iron-doped samples and found a peak near 750 ppm. Previously, the diffraction efficiency and photorefractive speed of iron-doped $BaTiO_3$ samples were reported by Schunemann *et al.*[13] More recently, we reported measurements of the photorefractive trap density in the iron-doped samples using the light-induced grating erasure technique.[14] In this letter, we describe a method of measuring photoinduced absorption effects using a configuration which is free from photorefractive beam coupling, allowing accurate quantification of the photoinduced absorption, $\Delta\alpha$.

The crystals used in our experiments were grown from a melt containing high-purity $BaCO_3$ and TiO_2 and extreme care was taken to minimize melt contamination by the furnace. Spark mass spectrographic analysis of the pure crystals showed less than 0.3 ppm iron (see Table I for a list of the other impurities present). After growth of two high-purity boules, several iron-doped boules were grown from the same melt using the composition 0.34% $BaCO_3$ and 0.66% $[(1-x)TiO_2-(x/2)Fe_2O_3]$ where x is the concentration in ppm. In these experiments 50, 500, and 1000 ppm concentrations were used. Chemical analysis of these boules indicates a segregation coefficient near unity (see Table II). At least two samples from each of these boules were cut along (100) planes and then mechanically and electrically poled. One sample was used as grown and the other annealed at 800 °C in a reducing oxygen partial pressure of 10^{-4} atm. For a more complete description of the growth and preparation of these samples the reader is referred to Ref. 13.

Two problems associated with photoinduced absorption measurements are wave-mixing effects and nonuniform illumination along the path of the probe beam. Nonuniform photoinduced absorption along the path of the probe beam results when both the pump and probe beams pass through the center of the sample. This causes the intensity of the pump beam to change along the path of the probe beam. Calculation of $\Delta\alpha$ would require a detailed knowledge of the analytical equations describing the photoinduced absorption, which is the unknown being determined. Nonuniform illumination effects can be minimized by two simple changes. First, a small diameter probe beam, approximately 1 mm, is directed parallel to, and just below the crystal surface to be illuminated. Second, expanding the diameter of the pump beam so that it is much larger than the crystal to approximate uniform illumination.

The experimental setup shown in Fig. 1 minimizes

TABLE I. Spark-source mass spectrographic analysis of undoped $BaTiO_3$. After Ref. 13.

Element	Level (ppm) present in $BaTiO_3$
B	5
Na	<2
Mg	2
Al	0.5
Si	4
P	0.05
S	<2
Cl	10
K	<0.1
Ca	2
Cr	<0.02
Mn	<0.02
Fe	0.3
Ni	0.04
Cu	
As	0.1
Sr	50

[a] Present address: Department of Physics and Astronomy, Louisiana State University, Baton Rouge, LA 70803.

 0003-6951/91/260004-03$02.00 © 1991 American Institute of Physics

TABLE II. Chemical analysis of the $BaTiO_3$ samples. After Ref. 13

Iron doping level added to the Melt (ppm)	Iron level in $BaTiO_3$ crystals analyzed (ppm)[a]
0	0.3[b]
50	49
500	530
1000	980

[a]Atomic absorption (Northern Analytical)
[b]Spark-source mass spectrometry (Northern Analytical)

these problems in several ways. Wave mixing effects are eliminated by: (1) using two separate lasers for the pump and probe beams and (2) intersecting the beams in the x-y plane of the crystal, which by symmetry forbids beam coupling of the writing beams in $BaTiO_3$.[5] Using this setup, $\Delta\alpha$ is approximately constant along the path of the probe beam. Finally, the intensity of the probe beam is kept below 1 $\mu W/cm^2$ to minimize photoinduced absorption effects due to the probe beam. Under these conditions the photoinduced change in the absorption, measured by the probe beam, is given by[5]

$$\Delta\alpha = \frac{1}{L} \ln \frac{I_t^{(\text{without pump})}}{I_t^{(\text{with pump})}}, \tag{1}$$

where L is the thickness of the crystal parallel to the probe beam, $I_t^{(\text{without pump})}$ is the transmitted probe beam intensity without the pump beam present, and $I_t^{(\text{with pump})}$ is the intensity of the probe beam with the pump beam present. For our experiments, the pump source was a 3 W argon ion laser operating at 488 nm. The pump beam was expanded and collimated using two lenses and passed through a 1/2 wave plate and a polarizer before entering the crystal. The half wave plate allowed the intensity of the pump beam to be easily varied by simply rotating the 1/2 wave plate.

A second 100 mW air-cooled argon ion laser operating at 488 nm was used for the probe beam. This beam was expanded and collimated to a diameter of approximately 5 cm and directed through a polarizer positioned in a rotator, followed by an other polarizer aligned along the crystal axis, and finally through a 1-mm-diam aperture. The intensity of the probe beam was modulated at a frequency of 1000 Hz using an optical beam chopper, and synchronously detected using a photomultiplier tube and a lock-in amplifier. In all of these measurements the pump and

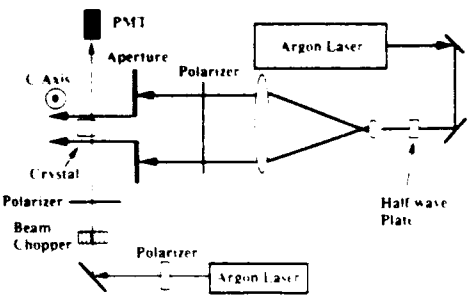

FIG. 1. Setup used to study photoinduced absorption.

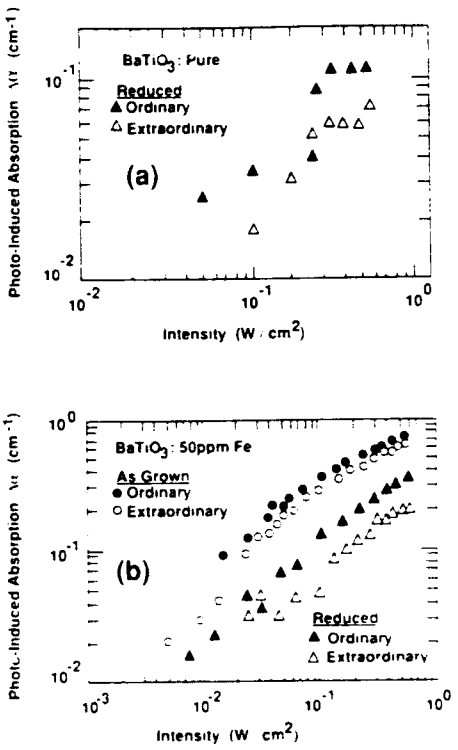

FIG. 2. Photoinduced absorption in $BaTiO_3$ plotted as a function of the pump beam intensity for (a) pure and (b) 50 ppm Fe.

probe beam polarizations were the same, that is, both parallel to the a axis (ordinary polarization) or c axis (extraordinary polarization). The change in the absorption was measured at various pump beam intensities for both ordinary and extraordinary polarization.

The results of these measurements are shown in Figs. 2 and 3. The change in the absorption for the pure as-grown crystal is not shown since there was none detected at the intensities used in this work. The rise time of the induced absorption was faster than the resolution of our detection system, which was a few milliseconds, while the dark decay time was on the order of 10–20 min. Because of this, the measurements started at the low pump intensities and proceeded to the high intensities. After a run, the crystal was allowed to return to the dark equilibrium conditions. As shown in the figures, the photoinduced absorption $\Delta\alpha$ increases nonlinearly with intensity for all the samples. However, since the experiment was designed to minimize intensity variations across the crystal surface, very high intensities were not achievable and we were unable to observe saturation.

As shown in Table III, both the absorption and the change in the absorption were found to increase with iron content for a given polarization, pump beam intensity, and oxidation state. Also, for any particular dopant level, the absorption and the photoinduced absorption of the as-grown sample was always larger than that of the reduced sample. The sublinear intensity behavior of the photoinduced absorption resembles that of the sublinear photocon-

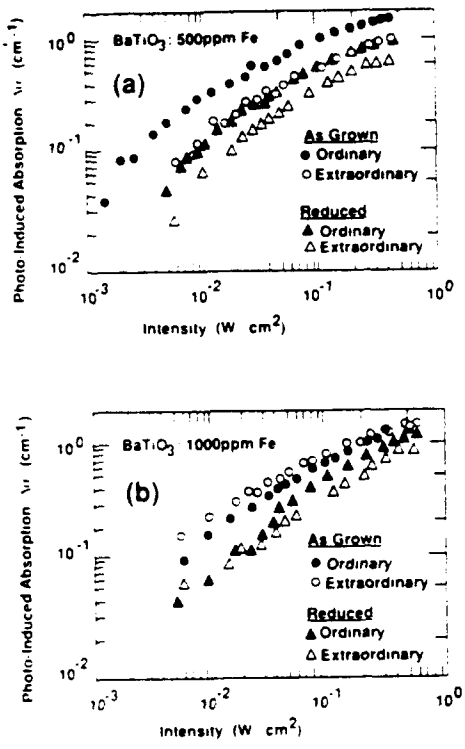

FIG. 3. Photoinduced absorption in $BaTiO_3$ plotted as a function of the pump beam intensity for (a) 500 ppm Fe and (b) 1000 ppm Fe.

ductivity measured by Ducharme and Feinberg.[15] The photorefractive erasure rate of our as-grown samples was previously reported to increase sublinearly with intensity[14] and therefore they seem to correspond to the type-B crystals discussed by Mahgereftreh.[16] Since the intensity dependence of the photoinduced absorption and the photoconductivity are similar, it is likely that shallow levels, as described in the models of Mahgereftreh[16] and Brost,[17] play a role in the photoinduced absorption. If the shallow acceptor levels were the source of the photoinduced absorption, then annealing a type-B crystal in reducing atmospheres, should result in partial filling of the shallow acceptor levels and thus a decrease in the photoinduced absorption. As shown in the figures and Table III, the crystals that were annealed in reduced oxygen partial pressures did show a decrease in the photoinduced absorption.

In conclusion, we have performed photoinduced absorption measurements on pure and Fe-doped samples of $BaTiO_3$. Our results show that: (1) there is a photoinduced absorption effect that increases with the addition of iron, (2) the photoinduced absorption increases sublinearly with intensity, and (3) annealing the crystals in reduced oxygen partial pressures lowers the photoinduced absorption. At present it is not clear if the charge centers responsible for the photoinduced absorption are due to iron, or if the charge compensating defects, such as oxygen vacancies or Fe-oxygen vacancy complexes, are the cause. Further experiments, such as correlation of the electron paramagnetic resonance spectra with the photorefractive trap density and photoinduced absorption, would be needed to clarify the exact nature of the photorefractive centers.

TABLE III. Absorption coefficient at 488 nm was measured using a Perkin-Elmer Lambda 9 double beam spectrometer. The photoinduced absorption data is given at a laser intensity of 0.5 W/cm^2. All of the data are for ordinary polarization.

Fe concentration	Absorption (cm^{-1})		$\Delta\alpha$ (cm^{-1})	
	as-grown	Reduced	as-grown	Reduced
Pure	0.53	0.47	...	0.11
50 ppm Fe	0.76	0.66	0.7	0.31
500 ppm Fe	1.73	0.63	1.1	0.9
1000 ppm Fe	...	1.23	1.05	1.05

[1] Jack Feinberg, J. Opt. Soc. Am. 72, 46 (1982).
[2] G. Valley, J. Opt. Soc. Am. B 4, 14 (1987).
[3] N. V. Kuktarev, E. Kratzig, H. C. Kulich, and R. A. Rupp, Appl. Phys. B 35, 17 (1984).
[4] M. Ewbank, P. Yeh, and J. Feinberg, Opt. Commun. 59, 423 (1986).
[5] D. A. Temple and C. Warde, J. Opt. Soc. Am. B 3, 337 (1986).
[6] Andy Motes and Jin Joong Kim, Opt. Lett. 12, 199 (1987).
[7] Andy Motes and Jin Joong Kim, J. Opt. Soc. Am. B 4, 1379 (1987).
[8] A. Motes, G. Brost, J. Rotge, and J. Kim, Opt. Lett. 13, 509 (1988).
[9] G. A. Brost, R. A. Motes, and J. R. Rotge, J. Opt. Soc. Am. B 5, 1879 (1988).
[10] R. M. Pierce, R. S. Cudney, G. D. Bacher, and Jack Feinberg, Opt. Lett. 15, 414 (1990).
[11] M. B. Klein and R. N. Schwartz, J. Opt. Soc. Am. B 3, 293 (1986).
[12] G. Godefroy, G. Ormancey, J. Jullien, W. Ousi-Benomar, and Y. Semanou, *Digest of IEEE International symposium on Applications of Ferroelectrics* (ISAF) (IEEE, New York, 1986), paper PA-1.
[13] P. G. Schunemann, D. A. Temple, R. S. Hathcock, H. L. Tuller, C. Warde, and H. P. Jenssen, J. Opt. Soc. B 5, 1685 (1988).
[14] D. A. Temple, R. S. Hathcock, and C. Warde, J. Appl. Phys. 67, 6667 (1990).
[15] S. Ducharme and J. Feinberg, J. Appl. Phys. 56, 839 (1984).
[16] Daniel Mahgereftreh and Jack Feinberg, Phys. Rev. Lett. 64, 2195 (1990).
[17] G. A. Brost and R. A. Motes, Opt. Lett. 15, 1194 (1990).

Intensity dependent photorefractive properties of $BaTiO_3$

Doyle A. Temple,[a)] R. Scott Hathcock, and Cardinal Warde
Department of Physics and Center for Materials Science and Engineering, Massachusetts Institute of Technology, Cambridge, Massachusetts 02139

(Received 14 August 1989; accepted for publication 19 February 1990)

We have used the light-induced grating erasure technique to measure the photorefractive properties of pure and iron doped $BaTiO_3$. Our experiments were performed using an anisotropic configuration which forbids beam coupling and self-diffraction between the writing beams, resulting in plane parallel intensity fringes that do not change with time. This allowed direct measurement of the charge transport processes without any feedback on the grating due to wave-mixing processes. The results from these experiments show that the photorefractive parameters known as the trap density N_{pr} and the mobility-recombination time product $\mu\tau_r$ vary with intensity and are not material constants.

I. INTRODUCTION

The photorefractive properties of $BaTiO_3$ and other photorefractive materials, have been studied by a number of researchers using a variety of optical techniques.[1–6] Many of the experimental results are found to be described by the hopping model[1] or the band transport model.[7] One method for optical characterization of photorefractive materials is the light-induced grating erasure technique.[5] Using this technique, Feinberg found that the grating spacing dependence of the photorefractive gratings in $BaTiO_3$ was well described by the models,[1,7] and could be used to determine the photorefractive trap density N_{pr}. Mullin and Hellwarth performed similar experiments in $Bi_{12}SiO_{20}$ (BSO) and showed that the technique could also be used to determine the mobility recombination time product $\mu\tau_r$.[5] However, Ducharme and Feinberg found that the photoconductivity of $BaTiO_3$, determined from the light-induced grating decay rates of photorefractive gratings, varies nonlinearly with intensity.[8] More recently, Brost *et al.*[9] found that their beam coupling data showed that the photorefractive trap density in $BaTiO_3$ varied with intensity.

In this paper we report the results of light-induced grating erasure measurements on pure and Fe doped $BaTiO_3$ using anisotropic gratings that do not allow beam coupling or self-diffraction between the writing beams. The results show the photorefractive parameters known as the trap density N_{pr} and the mobility recombination time product $\mu\tau_r$ are functions of intensity.

II. THEORY

A. Photorefractive response time

Consider the band transport model of Kukhtarev[7] in which there are donor and acceptor levels in the band gap of the crystal. For this example, we have chosen (1) the acceptor density to be larger than the donor density, $N_A > N_D$, and (2) the transport is dominated by hole conduction.[8] If all the electrons from the donors are transferred to the acceptors, the density of unfilled acceptors is $N_A - N_D$. These unfilled acceptors are assumed to be available to be redistributed by the light among all the acceptor levels. If the applied intensity pattern is in the form of a sinusoidal fringe pattern

$$I(x) = I_0[1 + m\cos(Kx)], \tag{1}$$

where $m \ll 1$, and K is the spatial frequency of the fringes, the resulting charge distribution may also be sinusoidal. For this case, the charge transport solutions of Kukhtarev[7] and Feinberg[1] both predict an exponential response for the photorefractive gratings given by

$$\frac{1}{\tau} = \frac{\sigma_{ph}}{\epsilon}\left(\frac{1 + (\epsilon kT/e^2 N_{pr})K^2}{1 + (\tau_r \mu k_b T/e)K^2}\right), \tag{2}$$

where

$$\sigma_{ph} = \frac{e\mu[(s/h\nu)I_0 + \beta_r](N_A - N_D)}{\gamma_r N_D}, \tag{3}$$

is the photoconductivity, μ is the mobility, γ_r is the recombination constant, ν is the light frequency, s is the photoionization cross section, h is Planck's constant, β_r is the thermal generation constant, ϵ is the static dielectric constant, k_b is the Boltzmann constant, T is the lattice temperature,

$$\tau_r = 1/(\gamma_r N_D), \tag{4}$$

is the recombination time and

$$N_{pr} = N_D \tag{5}$$

is the photorefractive trap density. The only intensity dependence in Eq. (2) is the photoconductivity, given by Eq. (3), which is predicted to be linear in intensity. Also, Eqs. (4) and (5) give the mobility recombination time product and the photorefractive trap density as material constants.

B. Anisotropic diffraction

For the experiments reported here anisotropic gratings were used. That is the grating vector lies in the x-y plane of

[a)] Present address, Department of Physics and Astronomy, Louisiana State University, Baton Rouge, LA 70803.

 0021-8979/90/116667-04$03.00 © 1990 American Institute of Physics

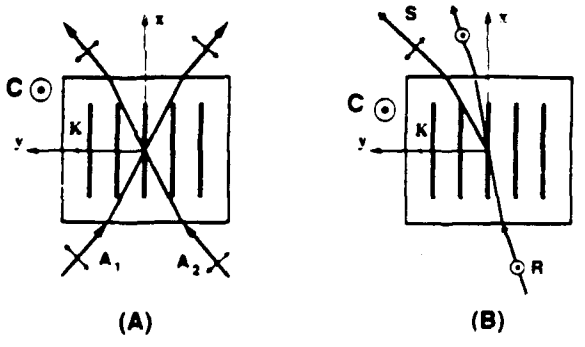

FIG. 1. Beam geometry illustrating (a) writing and (b) readout of an anisotropic photorefractive grating in the x-y plane. In (a) the writing beams A_1 and A_2 intersect in the crystal producing a photorefractive grating with a wave vector $\mathbf{K} = \mathbf{k}_2 - \mathbf{k}_1$. In (b) an extraordinary polarized readout beam **R** scatters into an ordinary polarized beam S, where $\mathbf{K} = \mathbf{k}_S - \mathbf{k}_R$.

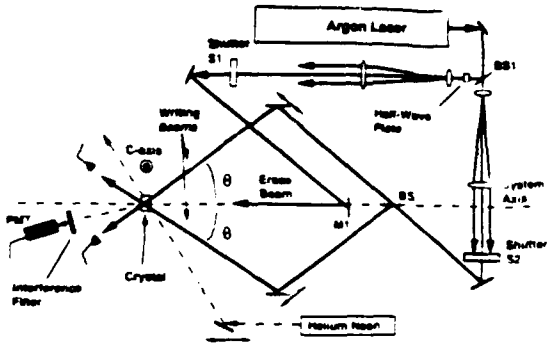

FIG. 2. Optical system used for light-induced grating erasure as a function of grating vector **K**.

the crystal.[10,11] One of the advantages of anisotropic diffraction is that there are certain configurations in which gratings can be produced with no beam coupling or self-diffraction allowed between the writing beams.[12] For two waves intersecting in a photorefractive crystal the amount of coupling or self-diffraction between the writing beams is proportional to the effective susceptibility[13]

$$\chi_{\text{eff}} = (\hat{e}_1^* \cdot \hat{e}_2)[\hat{e}_1^* \cdot (-\bar{\varepsilon}_0 \cdot \mathbf{E} \cdot \bar{\bar{R}} \cdot \bar{\varepsilon}_0) \cdot \hat{e}_2], \tag{6}$$

where $\hat{e}_1$ and $\hat{e}_2$ are the polarization vectors of the writing beams, $\hat{e}_R$ and $\hat{e}_S$ are the polarization vectors of the readout and scattered beams respectively, $\bar{\varepsilon}_0$ is the second rank optical dielectric tensor, $\bar{\bar{R}}$ is the third rank electro-optic tensor, and **E** is the space charge field. If the two waves interfere in the x-y plane of 4 mm symmetry $BaTiO_3$ as shown in Fig. 1(a), the effective susceptibility is zero when the polarizations of the writing beams are both ordinary or both extraordinary.[12] In this case, the feedback between the charge transport processes and the wave diffraction processes is eliminated, resulting in intensity fringes that are parallel planes and that do not change with time. Thus for very small modulation, $m \ll 1$, the solutions derived by Kukhtarev[7] and Feinberg,[8] are very close to the actual experimental conditions. Since the feedback from the wave-mixing processes on the charge transport processes of grating formation has been eliminated, each can be studied independently. This is therefore an excellent configuration for the measurement of photorefractive parameters.

Equation (6) does allow anisotropic diffraction to occur for readout of this grating. In this instance, the effective susceptibility is

$$\chi_{\text{eff}} = (\hat{e}_2^* \cdot \hat{e}_1)[\hat{e}_R^* \cdot (-\bar{\varepsilon}_0 \cdot \mathbf{E} \cdot \bar{\bar{R}} \cdot \bar{\varepsilon}_0) \cdot \hat{e}_S], \tag{7}$$

where $\hat{e}_R$ and $\hat{e}_S$ are the polarization vectors of the readout and scattered beams. For a negative uniaxial crystal the phase matching angles for anisotropic diffraction as shown in Fig. 1(b) are given by[12]

$$\sin(\alpha_R) = \left[\frac{n_0^2 - n_e^2}{4\sin(\theta)}\left(\frac{\lambda_W}{\lambda_R}\right) - \frac{\lambda_R}{\lambda_W}\sin(\theta)\right], \tag{8}$$

and

$$\sin(\alpha_S) = [n_0^2 - n_e^2 + \sin^2(\alpha_R)]1/2, \tag{9}$$

where α_R and α_S are the angles outside the crystal of the extraordinary polarized readout beam and ordinary polarized scattered beam measured from the surface normal, n_0 and n_e are the indices of refraction at the readout beam wavelength, θ is the angle of the writing beams with the surface normal, and λ_W and λ_R are the writing and readout beam wavelengths.

III. EXPERIMENTAL METHODS

A. Light-induced grating erasure

The light-induced grating erasure technique involves writing a photorefractive grating in the crystal with two coherent plane waves, then removing the writing beams and flooding the crystal uniformly with an erase beam.[7] The grating decay rate is simultaneously monitored with a low power (1 μW cm^{-2}) readout beam incident at the Bragg angle.

The optical setup used for the light-induced decay rate experiment is shown in Fig. 2. In this setup an argon ion laser was used for the writing beams and the erase beam. As shown in Fig. 2, a beam splitter labeled BS1, was placed just after the laser to produce two separate beams that were expanded and collimated using spatial filters. The beam reflected by BS1, was used as the erase beam. This beam was directed onto mirror M1 then through the center of the crystal mount with the line between M1 and the crystal mount defining the system axis. The intensity of the erase beam was varied using a rotating half wave plate followed by a polarizer. The beam transmitted through the beam splitter BS1 was directed through the second beam splitter BS to produce two writing beams. These beams were directed symmetrically about the system axis. Optical table rails were mounted parallel to the two writing beam paths with mirrors mounted on each rail to redirect the beams onto the crystal. The rails were calibrated to allow accurate angular measurements. The intensity of one of the writing

beams was varied using rotating polarizer followed by a fixed polarizer. This was necessary to ensure that the modulation index was small $m \ll 1$.

For $BaTiO_3$, phase matching for anisotropic diffraction is limited to an angular range of $3° < \alpha < 20°$ for 488 nm writing beams and 633 nm readout beams, where α is the incident angle of the readout beam outside of the crystal. We note here that extreme care must be taken so as not to confuse higher diffracted orders which are easily observed in the anisotropic configuration in $BaTiO_3$.[14] Also, we found that small shifts in the position of the erase beam in the crystal caused significant variations in the decay rates. Therefore, the crystal and the erase beam were not moved during the experiments.

A HeNe laser was used to readout the gratings (see Fig. 2). This beam was expanded using two lenses and the intensity was varied using a rotating polarizer followed by a fixed polarizer. The beam was directed along the optical rail by two mirrors and modulated by a beam chopper at a frequency of 1000 Hz. The readout beam angle could be varied by moving a mirror along the rail and redirecting the beam to the crystal. The diffracted beam was synchronously detected using a photomultiplier tube and a lock-in amplifier with the output of the lock-in captured by an AT&T 6300 computer equipped with a Data Translation data acquistion board. The sampling rate was set at 80 Hz and the grating decay rates were found to be well fitted by a single exponential. Also, a 633 nm interference filter was placed in front of the photomultiplier tube to eliminate bleaching from the argon laser.

A typical measurement was made as follows: First shutter S1 was opened and any gratings present in the crystal were erased. Shutter S1 was closed and shutter S2 opened allowing the writing beams to intersect in the crystal forming a photorefractive grating. This grating was monitored by measuring the diffraction of a HeNe beam incident upon the crystal at the Bragg angle, Eq. (8). When the diffraction efficiency reached saturation, shutter S2 was closed and simultaneously S1 opened, erasing the grating. After three or four decay times were measured, the angles of the writing beams were changed and the measurement repeated. After one complete scan of the angular range was finished, the erase beam intensity was increased and the measurement repeated. The writing beams, and the erase beam were ordinary polarized for all the measurements reported here.

B. Sample preparation

The crystals used in our experiments were grown from a melt containing high purity starting materials and extreme care was taken to minimize melt contamination by the furnace. After growth of two high purity boules, several iron doped boules were grown from this melt at the concentrations 50, 500, and 1000 ppm in the melt. Samples from each of these boules were cut along (100) planes and then mechanically and electrically poled. One sample from each doping concentration was annealed at 800 °C in a reducing oxygen partial pressure or 10^{-4} atm. Another sample was prepared from a melt containing pure TiO_2 and

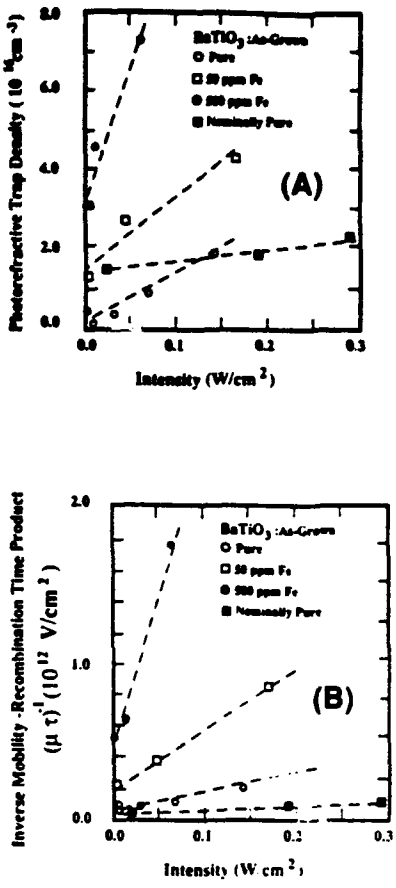

FIG. 3. Intensity dependence of (A) the trap density and (B) the mobility recombination time product in as grown $BaTiO_3$. The dashed lines are qualitative guides.

reagent grade BaO. This sample will be referred to as nominally pure since it was grown from the type of feed materials commonly used in the growth of $BaTiO_3$. For a more complete description of the growth and preparation of these samples the reader is referred to Ref. 15. Beam coupling measurements indicate that all the crystals exhibited p type conduction.[16]

IV. RESULTS AND DISCUSSION

The decay rate versus grating vector data was fitted to Eq. (2) for each erase beam intensity, and the parameters known as the photoconductivity σ_{ph}, the photorefractive trap density N_{pr}, and mobility recombination time product $\mu\tau$, were calculated from these fits. The results are plotted in Figs. 3, 4, and 5. The decay rate of the 1000 ppm crystals showed nonexponential behavior and was not suitable for this type of analysis.

The plots shown in Figs. 3 and 4 indicate that, for a given crystal, the trap density and the inverse of the mobility-recombination time product have very similar intensity dependencies. Since it is unlikely that the mobility is intensity dependent this would seem to indicate that the trap density is related to the recombination time as in Eqs (4) and (5). This behavior was found for all the samples

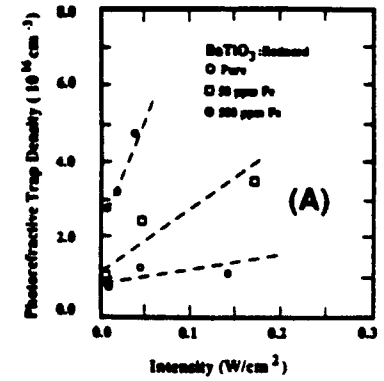

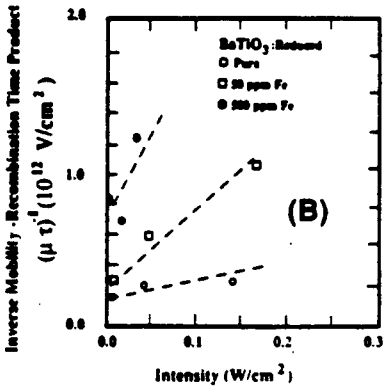

FIG. 4. Intensity dependence of (A) the trap density and (B) the mobility recombination time product in reduced $BaTiO_3$. The dashed lines are qualitative guides.

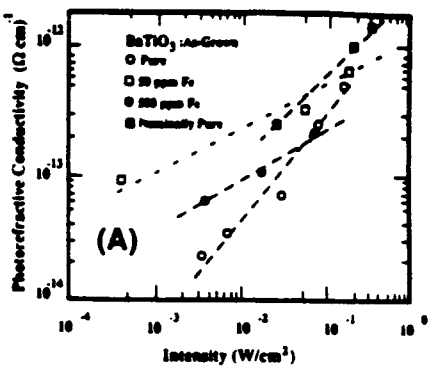

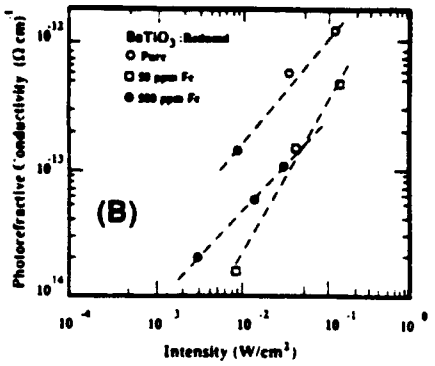

FIG. 5. Intensity dependence of the photoconductivity in (A) as grown $BaTiO_3$ crystals and (B) reduced $BaTiO_3$ crystals. The dashed lines are qualitative guides.

measured including the high purity sample and the nominally pure sample. The nonlinear intensity dependence of the photoconductivity, shown in Fig. 5, was found to be similar to that observed by Ducharme and Feinberg.[2,8]

Intensity dependent trap densities can be explained by the normal models through trap depletion. However, it is not unreasonable to assume that the intensity dependent recombination time and trap density are in some way related to the nonlinear photoconductivity. Since the transport seems to be well fitted by a diffusion type photoconductivity, as evidenced by the grating spacing dependence, modification of the model to include the intensity dependent effects may be possible. One possibility is a model, proposed by Rose, in which there exists a distribution of levels in the band gap.[17] However, direct of Rose's model does not seem appropriate since it disagrees with temperature dependencies reported by Ducharme and Feinberg.[8]

In conclusion, we have used the light-induced grating erasure technique to measure the intensity dependence of the photorefractive properties of pure and Fe doped $BaTiO_3$. Our results show that direct interpretation of the photorefractive models would lead to an intensity dependent trap density and recombination time with a strong correlation between the two. Further experiments, such as accurate measurements of the temperature dependence over a wider range of intensities, are needed before a substantial modification of the photorefractive charge transport models can be accomplished.

J. Feinberg, D. Heiman, A. R. Tanguay, Jr., and R. W. Hellwarth, J. Appl. Phys. 51, 1297 (1980).
S. Ducharme and J. Feinberg, J. Opt. Soc. Am. B 3, 283 (1986).
M. B. Klein and R. N. Schwartz, J. Opt. Soc. Am. B 3, 293 (1986).
E. Kratzig, F. Welz, R. Orlowski, V. Doormann, and M. Rosenkranz, Solid State Commun. 34, 817 (1980).
R. A. Mullin and R. W. Hellwarth, J. Appl. Phys. 58, 40 (1985).
M. Carrascosa and F. Agullo-Lopez, IEEE J. Quantum Electron. 22, 1369 (1986).
N. Kukharev, Sov. Tech. Phys. Lett. 2, 438 (1976).
S. Ducharme and J. Feinberg, J. Appl. Phys. 56, 839 (1984).
G. A. Brost, R. A. Motes, and J. R. Rotge, J. Opt. Soc. Am. B 5, 1879 (1988).
S. I. Stepanov, M. P. Petrov, and A. A. Kashilin, Sov. Tech. Phys. Lett. 3, 345 (1977).
N. V. Kukhtarev, E. Kratzig, H. C. Kulich, and R. A. Rupp, Appl. Phys. B 35, 17 (1984).
D. A. Temple and C. Warde, J. Opt. Soc. Am. B 3, 337 (1986).
J. Feinberg, in *Phase Conjugate Optics*, edited by R. Fisher (Academic, New York, 1984), Chap. 11.
D. A. Temple and C. Warde, J. Opt. Soc. Am. B 5, 1800 (1988).
P. G. Schunemann, D. A. Temple, R. S. Hathcock, H. L. Tuller, H. P. Jenssen, D. R. Gabbe, and C. Warde, J. Opt. Soc. B 5, 1685 (1988).
Beam coupling was measured in these samples by the authors and will be described in more detail in a future publication.
A. Rose, *Concepts in Photoconductivity and Allied Problems* (Krieger, Huntington, NY, 1978).

8 Publication and Presentations

1. D. A. Temple, "Photoinduced Absorption and Photorefractive Grating in Barium Titanate," Ph.D Thesis, MIT, September 1988

2. R. S. Hathcock,"Optical and Photorefractive Properties of Iron Doped Barium Titanate," Ph.D Thesis, MIT, September 1989

3. D. A. Temple, R. S. Hathcock and C. Warde,"Intensity Dependent Photorefractive Properties of $BaTiO_3$:Fe," J. Appl. Phys. **67**, 6667 (1990)

4. M. H. Garrett, J. Y. Chang, H. P. Jenssen, H. L. Tuller and C. Warde, "Top-Seeded Solution Growth and Photorefractive Characterization of Barium Strontium Titanate, $Ba_{1-x}Sr_xTiO_3$," Proceedings of the American Conference of Crystal Growth - 8, Vail, Colorado, July 1990

5. D. A. Temple, R. S. Hathcock and C. Warde, "Photoinduced Optical Absorption in $BaTiO_3$:Fe," accepted for publication, Appl. Phys. Lett. (1991)

9 List of Personnel

Faculty and Staff

Cardinal Warde (Professor of Electrical Engineering and Computer Science)
Hans P. Jenssen (Director of Laboratory for Advanced Solid State Laser Materials)

Graduate Students

Doyle Temple
R. Scott Hathcock
Peter G. Schunemann
Jenq-Yang Chang

Undergraduate Students

Jim Rolle

Support Staff

Margaret Eminian